Prediction of residual stress of an orthotropic plate due to welding

K. Spyridoni

Prediction of residual stress of an orthotropic plate due to welding

by

K. Spyridoni

to obtain the degree of Master of Science
at the Delft University of Technology
to be defended publicly on Monday February 4, 2019 at 14:30.

Student number:	4620828	
Thesis committee:	Prof. dr. M. Veljkovic,	TU Delft, supervisor
	Dr. ir. M.J.M. Hermans,	TU Delft
	Dr. H. Xin,	TU Delft

An electronic version of this thesis is available at `http://repository.tudelft.nl/`.

Cover picture: Pedestrian bridge with orthotropic steel deck in Ottawa, Canada. Digital Image. *Canam Bridges*, 2014. https://www.canambridges.com/

TU Delft

Preface

This research project represents the conclusion to my academic journey as a master student in Delft University of Technology. At this point, I have to mention the people who have encouraged me during these years.

I would like to thank my thesis supervisor, Prof. dr. M. Veljkovic, for suggesting to me a research topic that has stimulated my interest. His advice and support have been valuable during the entire process. Furthermore, I owe my gratitude to dr. H. Xin, who has offered me important advice on technical aspects of this project, every time that I turned to him for help. It would be a great omission not thank dr. ir. M.J.M. Hermans, who has offered essential feedback on my work and has helped me to organize the experimental part, on which this research project is based.

Finally, I would like to thank my family and friends for their endless support and the useful advice that they have shared with me throughout these years.

K. Spyridoni
Delft, February 2019

Abstract

Orthotropic steel decks are widely used in bridge construction nowadays, especially in case of long span bridges. One of the main problems of bridges that utilize this technology is the susceptibility to fatigue failure. Cyclic loading due to wheel loads, in combination with the complex network of welded details, make such types of decks prone to fatigue cracking, which poses a threat to the structure's integrity.

One of the factors that contribute to crack initiation and propagation under cyclic loading are welding-induced residual stresses. The localized heat input, due to welding, and the subsequent cooling, force the adjacent area to undergo expansion and shrinkage, which are, however, restricted by the surrounding material. As a result, residual stresses are formed, which can reach the yield strength of the material in the region near the weld. When these are tensile, they can accelerate the crack propagation rate, thus severely reducing the fatigue life and endangering the structure's safety. Knowing the residual stress distribution in welded joints of orthotropic steel decks can prove to be useful in the evaluation of resistance against fatigue.

In this research project, a finite element model which is able to predict residual stresses in normal strength steel weldments, has been developed. In the first stage of the research, a small-scale welding experiment has been conducted, during which temperature and distortion measurements were derived. The welding procedure was then modelled in the finite element software ABAQUS. Experimental data have been used to validate the accuracy of the adopted heat source model and parametric studies have been carried out, in order to investigate the influence of the heat source parameters and the heat losses on the temperature distribution.

The validated methodology was then applied on a trough-to-deck plate welded connection of an orthotropic steel deck. Longitudinal and transverse residual stresses have been calculated at various positions of the deck and stiffeners. The influence of the welding sequence on the residual stresses has been investigated, by considering two welding scenarios; parallel and sequential welding. The effect of the adopted stress-strain relationship under elevated temperatures on the residual stress field has been examined, by considering an ideal plastic material model and one that includes strain hardening. In addition to these, the impact of the boundary conditions has also been studied. Finally, the effect of welding on the appearance of imperfections is discussed, by considering the deflection of the deck plate, after the process. As a result, valuable information is obtained about the shape of residual stresses, the associated deformations, and the factors that affect them, in a welded connection of an orthotropic steel deck.

Contents

1 Introduction

1.1. Motivation for research

In the manufacturing and construction industry, welding is one of the most important joining techniques of metal components. From marine structures to civil engineering applications, welding is used both for fabrication and repairs. As a technique, it can be faster and more economical than other joining techniques, since it requires less labour. At the same time, it offers great flexibility in the design and forms more lightweight connections, as compared to bolted ones, resulting in significant material and financial savings.

Despite the important advantages, welding can also pose serious problems on the integrity of components. Some of those are residual stresses and distortions, inevitably induced by all welding methods. Welding distortions act at the expense of dimensional tolerances and can result in costly repairs and time delays [4]. Residual stresses are the stresses that exist within a body, in the absence of external loading. In case of welding, they arise due to the inhomogeneous temperature field generated during the process. The heat input due to welding generates an abrupt temperature increase, followed by a subsequent rapid cooling of the material, down to room temperature. In reality, the thermal gradients are so large, that the material undergoes plastic deformation. Residual stresses are generated, as a result of the restricted expansion and shrinkage of the material at the vicinity of the weld.

When residual stresses are exclusively present in the material, without any additional external loads, they cannot pose a serious threat to the component's integrity. In reality, the behaviour of residual stresses is additive in nature and structural failure is likely to occur when their action is combined with external stresses. Studies have suggested that residual stresses caused by welding can influence the behavior of a component, leading or contributing to a possible reduction of the fatigue strength, a premature yielding and loss of stiffness, a decrease of the fracture toughness and stress corrosion cracking [25]. Under external cyclic loading, tensile residual stresses can reduce the fatigue life by increasing the crack propagation rate, while compressive stresses are found to be favorable, since they slow down the fatigue crack growth. It is therefore important for the engineer to be properly informed about their distribution and magnitude, and also to include them in the estimation of the crack propagation rate, in case of fatigue checks.

The influence of residual stresses on the integrity of a welded connection is especially evident in case of orthotropic steel decks. Nowadays, they are widely used in bridge construction and some of the world's most impressive long span bridges are built in this form. This type of deck consist of a steel plate, stiffened along its longitudinal and transverse direction by stiffeners. An orthotropic steel deck is essentially a *nearly all steel superstructure*, in which a large number of steel pieces are welded together. From the early 1970s, it was found that many orthotropic steel deck bridges suffered from fatigue damages [30], [19]. The complex network of weld details, where crack propagation is likely to occur due to the inherent defects, along with the utilization of thin deck plates in earlier designs, to minimize the dead weight, has endangered the structure's fatigue life. In the Netherlands, the most known example of fatigue cracking in orthotropic decks is the Van Brienenoord bridge, where deck cracks were observed, seven years after its construction.

Ever since the observations of fatigue problems on orthotropic steel decks, research has focused on investigating the main reasons behind them. Studies have suggested that, apart from the increased traffic load, welding residual stresses in the connections have also constributed to the crack propagation [8]. Indeed, cracks have been observed in regions where the stress field due to external loads is purely compressive. This implies that crack propagation cannot be explained simply by external loading, since it can occur only when the component is loaded in tension. Such observations have increased the concerns about the inclusion of residual stresses in the estimation of crack propagation rates.

In this context, it becomes evident that the prediction of welding induced residual stresses is a field of utmost importance. Residual stresses can by investigated experimentally by non-destructive (X-ray diffraction) and destructive methods (sectioning method). Although, the actual stress distribution can be acquired mainly by experimental measurements, those can be costly, difficult to perform and applied only on existing specimens. On the other hand, recent developments in the Finite Element Method offer new possibilities of modelling and establish a new tool in the calculation of residual stresses. Any geometry, no matter how complex, can be modelled, with satisfactory results. Their accuracy, however, has to be verified by the engineer, since input parameters are user-dependent and interpretation of the results should be performed with care. In this sense, the need for a detailed methodology of modelling the welding procedure and predicting accurately residual stresses through a finite element analysis program is indispensable.

1.2. Purpose of research

The directions around which this research project evolves, can be summed up in two main questions:

- **How can the welding procedure be modelled in a finite element analysis software, so as the residual stress field can be predicted?**
- **What is the distribution of residual stresses in a welded through-to-deck plate connection of an orthotropic steel deck?**

The two main questions posed, give rise to additional points of interest:

- Why is it important to obtain information about the residual stresses in a material?
- What are the most important points that should be taken into account during numerical simulations? What are the parameters that should be considered when modelling the heat source and to what extent do they affect the integrity of the results?
- What kind of thermomechanical properties should be used when simulating the behaviour of a material due to welding? How are these properties influenced by increased temperature during welding?
- How does the welding sequence affect the residual stress field?
- How do applied boundary conditions influence the development of residual stresses in the material?

1.3. Applied methodology

The objective posed by the first main research question refers to the development of an accurate methodology able to predict welding residual stresses, through a finite element analysis software. Towards this goal, a small scale welding experiment has been conducted, during which, temperature and distortion measurements have been taken. Subsequently, the specimen is modelled in the FEA software ABAQUS. The welding procedure is simulated by a moving heat source and appropriate thermomechanical properties and boundary conditions are implemented. The simulation results are compared to the experimental data of temperature and distortion, in order to estimate the accuracy of the model.

In the second part of this thesis, the main objective is the application of the previously validated methodology in a through-to-deck plate connection of an orthotropic steel deck. Manually and automatically welded connections are modelled, so as to investigate the residual stress distribution. Additionally, two welding scenarios are examined; parallel and sequential welding, in order to evaluate the influence of the welding sequence on the residual stresses. A study is also conducted on the impact of the adopted material law model. The differences between including strain hardening or not, in the description of the mechanical behaviour of the

material under elevated temperatures, are examined. The influence of the applied boundary conditions is also discussed. Based on the contour plots of residual stresses, remarks are made on possible crack initiation positions.

1.4. Structure description

In order to approach the main objectives of this project, it is necessary to divide the workflow into distinctive parts.

Chapter 2 presents some fundamental information about residual stresses. Valuable insight into their origins and their effect on a structure's integrity is given. Moreover, the reasons why residual stresses should be investigated in orthotropic steel decks are presented.

Chapter 3 describes the procedure followed during the small-scale welding experiment. Details are given about the experimental set up and temperature and distortion recordings are presented.

The process of simulating the welding procedure of the small-scale experiment in the ABAQUS environment is expressed in Chapter 4. Special attention is paid on the heat source model for the simulation of the welding arc and necessary specifications about the adopted thermomechanical parameters are made. Additionally, parametric studies on the heat source model's and heat losses' parameters are conducted, in order to investigate their influence on the predicted temperature field. The thermomechanical simulation outcome is compared to the experimental data of temperature and distortion presented in Chapter 3, in order to validate the accuracy of the followed procedure.

In chapter 5, the validated methodology of welding modelling is applied on a welded rib-to-deck connection of an orthotropic steel deck. Residual stresses are predicted both in the deck and the stiffeners. The results of the study on the influence of the welding sequence, the boundary conditions and the material law are presented and discussed.

The conclusions of the present work are presented in Chapter 6. Additionally, recommendations are made for further research on this topic.

2

Background information

In this chapter, general information about residual stresses is given. First, the main mechanisms behind their creation are discussed, with more emphasis on welding induced residual stresses. Next, their effects on the component's integrity are presented and a connection is made between their action and fatigue failure in orthotropic decks. Finally, additional information is provided for the concept of orthotropic steel decks and their problems related to fatigue resistance.

2.1. Residual stresses

Residual stresses are internal stresses, existing in a component even in the absence of externally applied loads. Almost all fabrication processes, such as welding, machining or rolling, as well as surface treatments, such as shot peening, lead to the trap of stresses in the manufactured product. In reality, no manufactured component is free of such stresses.

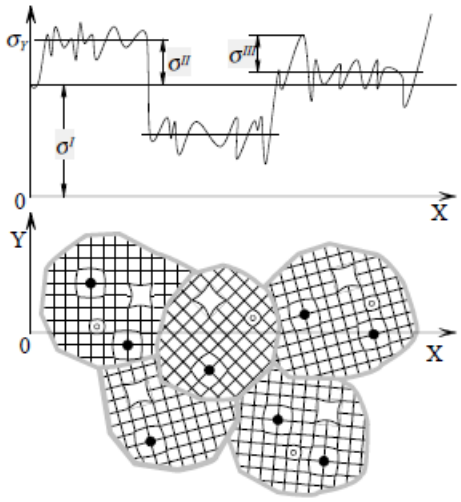

Figure 2.1: Types of residual stress in a material [29]

Residual stresses can be divided into three categories, depending on the scale over which they equilibrate [35]. They are investigated in macro- and microscopic level and they are classified as type I, II or III stresses (Figure 2.1). Type I residual stresses (macrostresses) extend over lengths comparable to the component's dimensions and neglect the underlying microstructure. Type II residual stresses extend in between adjacent grains, while type III residual stresses vary on an atomic scale [26], [29]. Residual stresses of second and third order are classified as microstresses. Stresses due to external loading and welding usually rank among macrostresses [29].

2.1.1. Formation of residual stresses

Generally, residual stresses arise because of incompatibilities between adjacent regions of the material or component [35]. Volume elements are forced by the surrounding material to form a different shape than the one they would equilibrate over, in the absence of this influence [26]. Residual stresses are an inevitable consequence of most fabrication processes and can arise due to various reasons.

1. Non-homogeneous plastic deformation
   The simplest way of introducing residual stresses plastically into a ductile material is to deform it beyond its elastic limit. Some typical manufacturing processes, such as bending and cold rolling, intentionally apply permanent deformations on a component, to attribute a desirable shape to it. Additionally, permanent deformation can be introduced in order to achieve a certain stress state. Such is the case of post weld improvement techniques (ie. peening), where compressive residual stresses are introduced in order to relieve the tensile residual stress field developed due to welding.

2. Phase transformation
   Rapid changes in the lattice structure from one form to another can generate discontinuities between adjacent regions, giving rise to residual stresses. A known example of such transformation is the martensitic transformation in steel.

3. Thermal gradients
   One of the most common reasons of residual stresses due to thermal gradients in a material, or between connected parts is welding. In the case of welding, the differential thermal cycle is responsible for the formation of residual stresses. The process is accompanied by an inhomogeneous temperature field, where points of high and low temperature are both present in the material. During the movement of the heat source along the welding direction, local heating of the joining components takes place, followed by a subsequent rapid cooling. This alternation between heating and cooling cycles causes the material to undergo expansion and shrinkage, which, if constrained, will result in the appearance of self-equilibrating residual stresses.

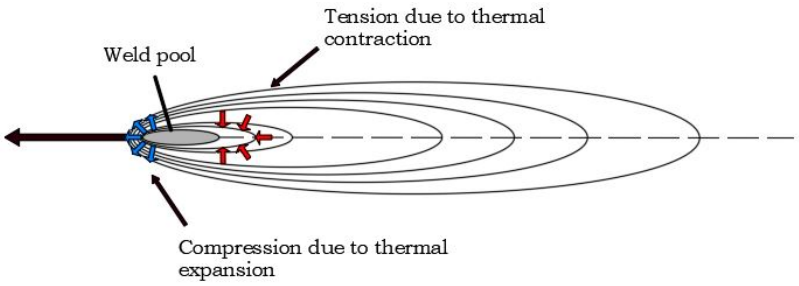

Figure 2.2: Formation of residual stresses due to welding. The expansion of the heated material and the shrinkage of the cooled material are restricted by the surroundings. Compression and tension develop respectively.

Welding induced residual stresses

The formation of residual stresses due to welding can easily be explained by a simple example. One can consider the specimen as a sum of many small elements. If they are evenly heated, the expansion of all elements in every spatial dimension will be uniform. With unrestrained expansion, no stresses will be induced in the body and the elements can be summed up to form a solid body. However, if the heating is not uniform, each element will expand proportionally to the temperature change it experiences. As part of a continuous body, the expansion of the most heated elements will be restrained by less heated ones. This time, all elements have a different size and cannot form a solid body without changes in the deformation or stress state. Thus, deformations and residual stresses occur in the body [29].

The evolution of longitudinal stresses and the temperature change can be understood through Figure 2.3. The type and magnitude of residual stresses differ during each stage of the welding process. All points far from the weld experience no change in their temperature, thus the stress is equal to zero. In the first stage of heating, as the source is approaching the point of interest, the temperature increases and neighbouring

elements are heated. Their expansion, however, is restricted by the low temperature surrounding material. This leads to the development of compressive stresses. Moving towards the negative x-direction, farther from the source, an opposite trend starts to develop. Longitudinal stresses transform into tensile due to cooling down and restrained shrinkage of previously heated elements.

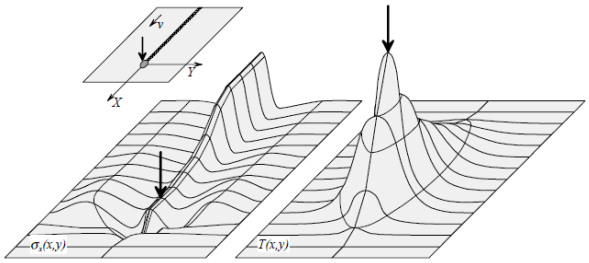

Figure 2.3: Longitudinal stress evolution during welding [29]

The magnitude of tensile reisdual stresses near the weld can be close to or equal to the yield stress. In cases of normal strength steel, longitudinal tensile stresses near the weld can reach the yield strength, while, on the other hand, this is not observed in case of high strength steels, where the tensile stresses are a smaller percentage of the material yield strength [25]. Due to the self equilibrating nature of residual stresses, farther from the weld area, balancing compressive stresses develop in the material (Figure 2.4).

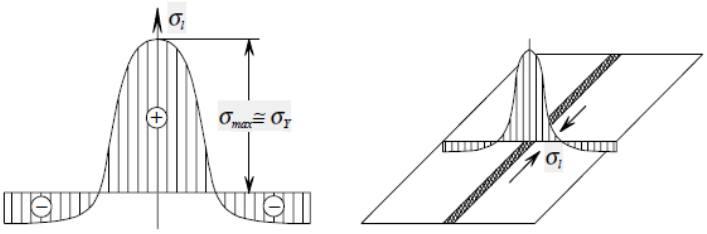

Figure 2.4: Welding induced longitudinal stresses [29]

Transverse residual stresses develop in a similar way to longitudinal stresses. Usually, their magnitude is less than that of longitudinal stresses, reaching approximately 25% of the material's yield strength.

2.1.2. Effects of residual stresses

Nowadays, evaluating the stresses induced in a component due to in-service loads is relatively easy, with the help of analytical and numerical tools. In many cases, however, a reliable prediction of a component's service life requires more, than simply considering their effect on its behaviour. Quite often, premature failure has appeared, as a result of the combination of residual stresses with external stresses [36].

One of the most common reasons of failure in steel structures is fatigue damage. Cyclic loads applied during the service life of a component can result, in the long run, to weakening of the material, even in cases when the acting stresses are below the strength of the material. Welded connections are regions where fatigue damage is likely to occur, due to the inherent defects induced inevitably by the process. Near the weld area, microcracks can grow into becoming large visible cracks, thus threatening the structure's integrity. Knowing the residual stress field at the locations of cracks is of utmost importance for the evaluation of the fatigue life. Presence of residual stresses can accelerate or discourage failure, since their action is additive to the action of external loading. Residual stresses of the same type of the external loading can encourage failure, while those of a sign opposite to that of the external loading can have a positive impact on the component's behaviour. Compressive residual stresses can prevent failure under tensile external loading, since the net tensile stresses which will be acting on the component will be reduced. This is also the main reason behind improvement techniques of welds such as shot peening, which intentionally introduce compressive residual stresses to relieve the tensile stress field. On the other hand, given the fact that crack propagation is influenced by tensile

stresses, the presence of tensile residual stresses in the weld area can accelerate the process of crack development, leading more quickly to failure under cyclic loading and thus decreasing the fatigue life [4], [25]. Even when the externally applied stresses are entirely compressive, residual tensile stresses in the weld area can make the component susceptible to failure due to fatigue [22]. As it is illustrated in Figure 2.5, the effective stress range is at the level of residual stresses near the weld. This implies that under tensile residual stresses, which increase the mean stress, the stress amplitude has to be reduced, if the fatigue life has to remain unaffected [36].

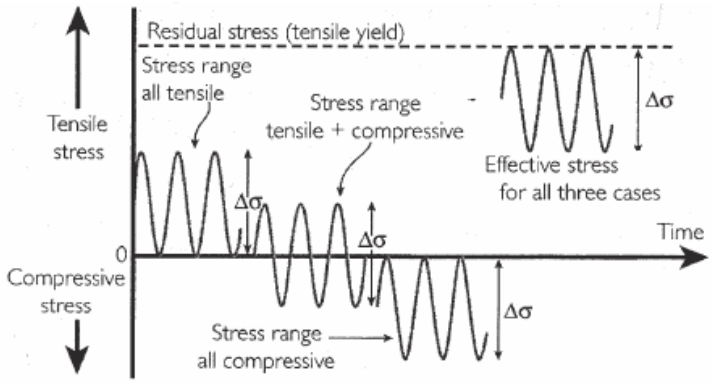

Figure 2.5: Effective stresses from applied and residual stresses [22]

In the case of orthotropic steel decks, the combined effects of local wheel loads, residual stresses and initial defects due to welding can provoke fatigue cracking. Various experimental approaches have dealt with fatigue cracking in orthotropic steel decks. In some cases, fatigue cracks were detected experimentally in areas where the applied stresses were relatively low but the residual stress field was tensile. Cracks have been observed in regions where stresses induced by external load were compressive [39], and they have remained open, even after removal of the applied, external load [22]. Possible exclusion of welding residual stresses from the estimation of the fatigue life of deck-to-rib connections can severely overestimate the fatigue resistance [9].

In the early stages of development of orthotropic steel decks, fatigue resistance has been overlooked in the design, leading to rapid damages, often only a few years after construction. Following this fact, many research projects have been devoted on evaluating the fatigue strength of connections and discovering the reasons behind crack initiation and propagation. However, even though residual stresses are believed to contribute to the initiation and propagation of cracks [3], [34], not enough information is available about their distribution in welded details of orthotropic steel decks [24], [7] [19].

2.2. Orthotropic steel decks

2.2.1. Overview

The first appearance of orthotropic steel deck bridges was made in the 1930s in Germany. Ever since, they have become a common practice in the bridge construction and today, some of the most impressive modern bridges utilize this deck system. The main advantage that makes this configuration competitive against concrete slabs is its low self weight. This is especially useful in case of large span bridges, where self weight becomes significant compared to the imposed loads. Moreover, due to their lightweight set-up, orthotropic bridge decks offer a significant advantage when pre-fabrication or rapid erection is necessary [22].

An orthotropic steel deck consists of a deck plate, stiffened on its lower surface, both longitudinally and trasversally by welded stiffeners at regular intervals (Figure 2.6) [17]. It can be compared to a plate with dissimilar stiffnesses in two directions; it is essentially an **ortho**gonal and aniso**tropic** plate. In this configuration, the deck plate serves several functions; it distributes the traffic loads to the rest of the system but also forms the top flange of the troughs, cross beams and main girders [22], [20]. This latter characteristic results in important material savings, thus reducing the total construction cost.

Over the last century, many configurations have been proposed for the construction of longitudinal stiffeners. An orthotropic steel deck can be formed either by using open or closed longitudinal stiffeners (Figure 2.7). Even though open stiffeners are easier to manufacture, inspect and maintain, their low torsional stiffness leads to an inefficient transverse distribution of local wheel loads. Moreover, they require smaller spacings and spans, thus resulting in greater use of material and welding volume. Nowadays, stiffening is mainly executed by closed cross section stiffeners that run through the crossbeam webs. Those stiffeners are fabricated by cold bending thin steel plates, to form, most commonly, a trapezoidal shape.

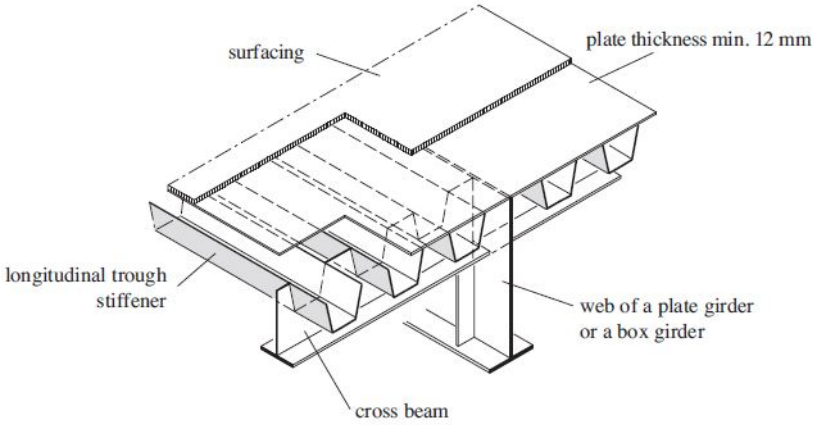

Figure 2.6: Overview of an orthotropic steel deck: the deck plate is stiffened longitudinally by troughs and transversally by cross beams [17]

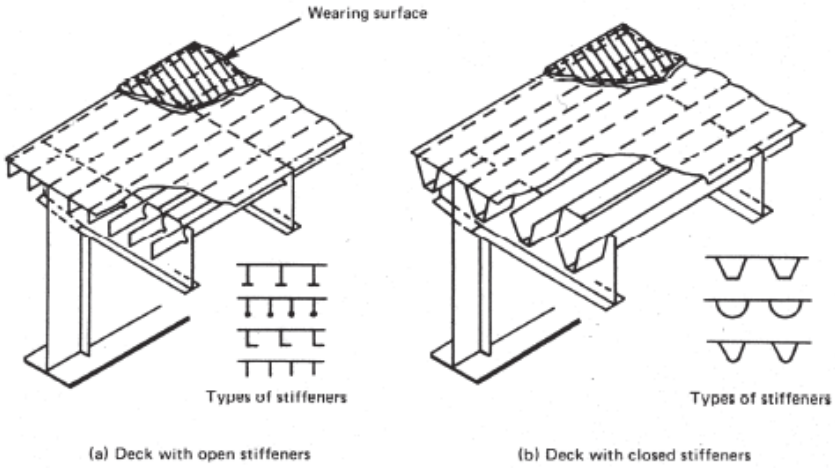

Figure 2.7: Types of orthotropic bridge decks [22]

In the transverse direction, inverted T-sections are welded to the deck plate, main girders and longitudinal stiffeners. The deck serves as a top flange to the cross beams, thus resulting in an increased rigidity. At the bottom of the intersection between longitudinal and transverse stiffeners, high stress concentration are observed, which, in combination with defects found in welded connections, can favour the crack initiation and propagation. In order to avoid this potentially catastrophic event, usually, cope holes are opened in the web of the transverse stiffeners. This leads to a reduction of the weld volume and limits the possibility of crack propagation.

2.2.2. Fatigue problems

Despite their remarkable advantages, orthotropic steel deck bridges have not been free of problems. Especially in early bridge designs, not enough attention was focused on the effect of fatigue life on the structure's integrity. This omission, in combination with the number and complexity of welded details, has lead to the appearance of fatigue cracking, as a result of cyclic loading due to traffic loads. The locations at which cracks can be observed can be summarized in four categories:

- The connection between deck plate and longitudinal stiffeners
- The connection between deck plate, longitudinal stiffeners and cross beam
- The connection between longitudinal stiffener and cross beam
- The trough splice joint

Deck plate to trough connection

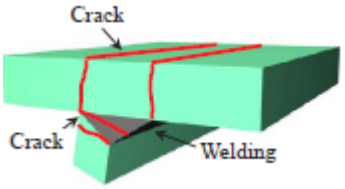

Figure 2.8: Crack pattern in deck-to-trough connection [9]

The welded connection of longitudinal stiffeners to the deck plate are locations where fatigue cracks are frequently observed. Four types of cracks can be distinguished (Figure 2.8) [22]:

- Cracks that propagate from the weld root through the deck plate
- Cracks that propagate from the weld root along the weld's throat
- Cracks that propagate from the weld toe through the deck plate
- Cracks that propagate from the weld toe through the longitudinal stiffener's web

Cracks initiating from the weld root usually propagate simultaneously in both vertical (through the deck's thickness) and longitudinal directions, thus becoming large invisible cracks, that are not detected until the damage on the wearing surface becomes visible (Figure 2.9). Considering the significant out-of-plane bending moments between the deck and the through, induced by vehicle loads, deck plate cracks can pose a serious threat to the structure's integrity and service life, if their length is large [19], [30]. Cracks that propagate along the weld's throat also develop in the longitudinal direction but usually, they do not threaten the safety of the deck structure. The intact deck plate remains functioning and redistribution of loads takes place [10].

Figure 2.9: Deck plate crack on the Van Brienenoord bridge. The crack initiated at the weld root of the deck-to-trough joint and propagated through and along the deck. Its length is approximately 50cm [10]

Deck plate to trough and cross beam joint

Another position where fatigue cracks can appear is the connection of the deck plate to the intersection of longitudinal and transverse stiffeners. Cracks initiate at the weld root, between the deck plate and the trough and propagate first in the vertical direction, through the deck plate and later in the longitudinal direction. As in the previous case, deck cracks in this location may also affect the integrity of the plate, and endanger the structure's safety. Given the fact that the deck plate also serves as a top flange to the crossbeam, insufficient function may lead to a reduced load bearing capacity of the crossbeam, under heavy loading [10].

Through to cross beam joint
The longitudinal and transverse stiffeners can be connected in various ways. In early designs of orthotropic steel decks, troughs were fitted between trasverse stiffeners. However, this kind of connection was shown to be low in fatigue strength [22]. Nowadays, the troughs usually pass through the cross beams, and cope holes may be opened on the cross beam, around the bottom of the trough. Depending on the type of the connection, different fatigue cracks can be observed. When the trough passes through the crossbeam and a cope hole is opened at the soffit, cracks can initiate at the weld toe and propagate through the trough or the crossbeam, or develop longitudinally in the trough. When no cope hole is opened, and the trough is welded all around to the crossbeam, cracks can inititate either at the weld toe and propagate through the trough or the crossbeam, or at the weld root and develop along the weld's throat [22]. However, if short, cracks at this joint do not threaten the structure's function, due to the possibility of load redistribution [10].

Through splice joint
This type of joint is usually executed by fitting a small length of trough between adjacent troughs. Cracks may initiate at the weld root, at the bottom of the stiffener. Cracks at this position have been related to poor workmanship during welding [38].

3

Small-scale experiment

The first stage of this research project consists of a small scale welding experiment, executed at the Material Science and Engineering laboratory at Delft University of Technology. The purpose of this experiment was to obtain temperature and distortion measurements for a given welding procedure. Those data were used at a later stage in order to verify the accuracy of the numerical model and its ability to predict temperature and distortions during and after welding.

3.1. Experimental procedure

The specimen under examination is a T-connection of two steel plates with dimensions $100 \times 150 \times 20mm$ and $55 \times 150 \times 6mm$. The latter is welded on the former along its longer dimension by two fillet welds on both sides (Figure 3.1). The steel grade used is S355, a non-alloy structural steel. The acceptable chemical composition and mechanical properties are fully described in the European standard EN10025, by the European Committee for Iron and Steel Standardization.

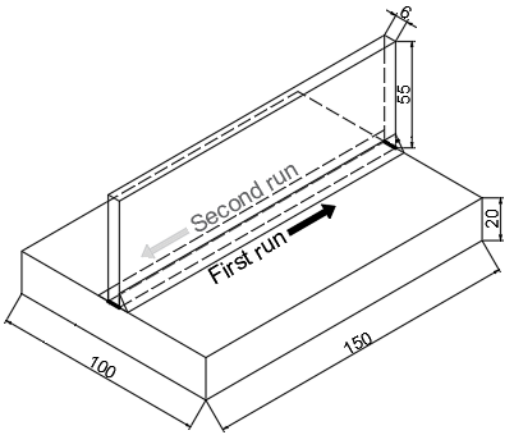

Figure 3.1: Specimen dimensions [mm] and welding procedure

The followed welding procedure is Gas Metal Arc Welding (GMAW). The used filler wire was LNM25, classified under ER70S-3, having a diameter of 1.2mm. The shielding gases were 85% Argon and 15% $C0_2$. The used power source was a Fronius TransPuls Synergic 5000. The welding torch was positioned at an angle of 90^o to the normal to the plate direction (welding direction), and 45^o to the trasverse one (Figure 3.2). The welding wire feed speed was $7m/min$ and the welding speed was set to $7mm/sec$.

In order to provide relative stability and facilitate the procedure of GMAW, the two steel plates were tack welded together at their ends (Figure 3.1). Next, the horizontal distortion of the vertical plate was measured at specific locations, as shown in Figure 3.3b, so as to act as a reference for the calculation of distortions after the welding passes.

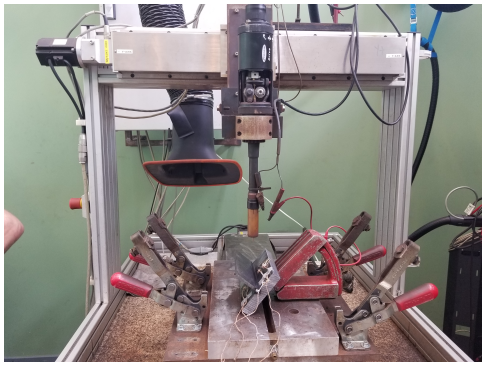

Figure 3.2: Positioning of specimen on welding table

Welding of the specimen was executed sequentially, in the opposite direction (Figure 3.1). During the first stage of the procedure, one fillet weld was executed on one side of the vertical plate. After a sufficiently long time, as the specimen had cooled down, the horizontal displacement at $5mm$ from the top of the vertical plate was measured. Next, the specimen was placed again on the welding table and the second fillet weld, on the opposite side of the vertical plate, was executed. Distortion measurements were also taken at the same positions, after the specimen had cooled down.

Steel grade	S355
Specimen dimensions (mm^3)	$150 \times 100 \times 20$ and $150 \times 55 \times 6$
Process	GMAW
Welding speed (mm/s)	7.00
Angle (longitudinal)	90^o
Angle (transverse)	45^o

Table 3.1: Main characteristics of welding procedure

3.2. Measurement set-up

The measurement of temperature was conducted through installed thermocouples which were connected directly to the multi-channels data logging system with a sampling frequency of $5Hz$. Four, K-type thermocouples were placed, perpendicular to the welding direction, at the top surface of the base plate [Figures 3.3a, 3.5a]. This type of thermocouples can detect temperatures reaching 1200°C, with an accuracy of ± 1°C.

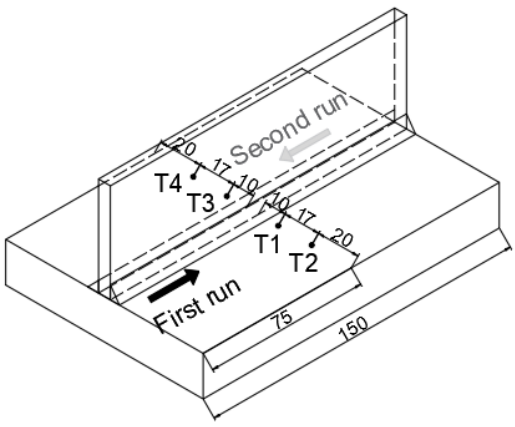

(a) Thermocouple positions on the base plate

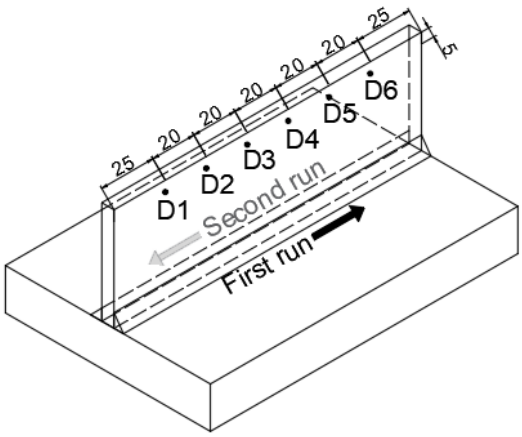

(b) Distortion measurement positions on the vertical plate

Figure 3.3: Thermo-mechanical measurement positions

Distortion measurements have been performed using a laser sensor. This instrument measures the distance between the sensor and the plate by detecting the time needed to reflect the laser beam back to the sensor (Figure 3.4). The optoNCDT IDL 1401-5 laser sensor, with a measurement range of 5mm has been used. The start and end of measuring range was at 20 and 25mm respectively [23]. The sensor was fixed at a constant position with a clamp and distortion measurements at 6 positions, on the vertical plate have been taken (Figures 3.3b, 3.5b).

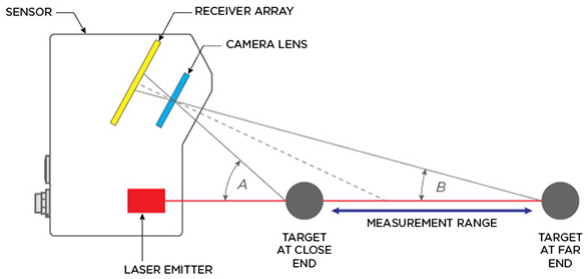

Figure 3.4: The principle of laser sensor displacement measurement [28]

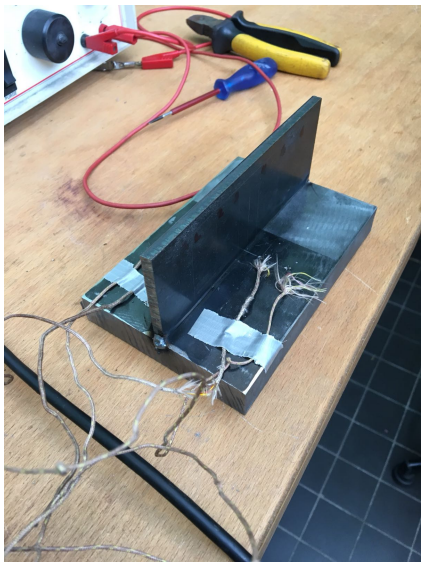

(a) Tack welded plates with installed thermocouples

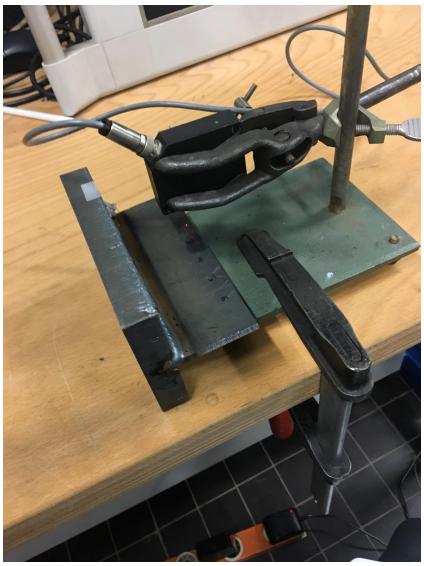

(b) Laser sensor set-up for distortion measurements

Figure 3.5: Thermo-mechanical measurement set-up

3.3. Experimental results

3.3.1. Temperature measurements

The temperature distribution during welding, at four measurement positions, is shown in Figures 3.6, 3.7. Abrupt increase of temperature is identified in positions T1 and T2, at the beginning of the first welding pass (Figure 3.6). Since these positions are located on this side of the bottom plate where the first welding pass is executed (Figure 3.3a), the erroneous measurements are attributed to sparks from the welding arc and spattering of the material. Thus, higher maximum temperatures are detected, than the ones that would appear in the absence of such event. Temperature measurements during the second welding run show less discrepancy.

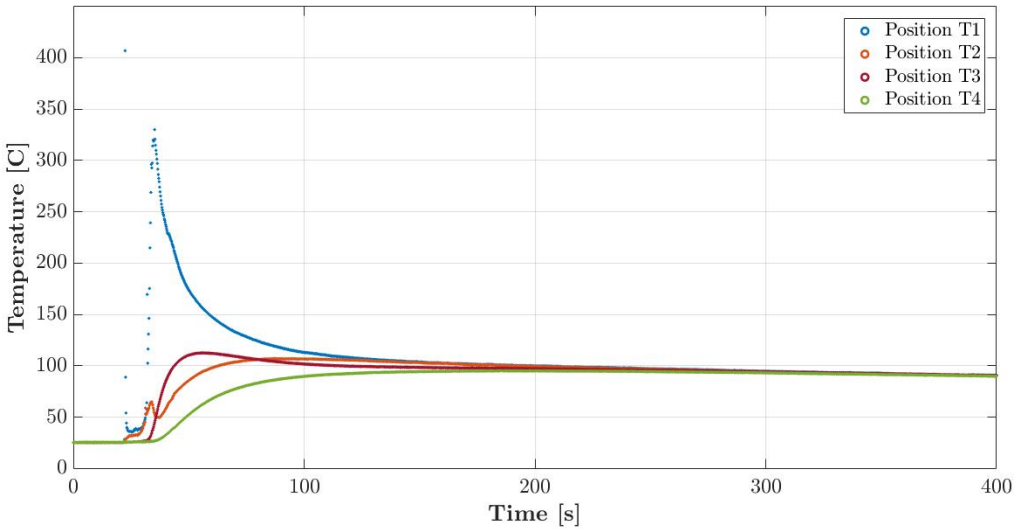

Figure 3.6: Temperature histories of four points on the base plate after the first pass

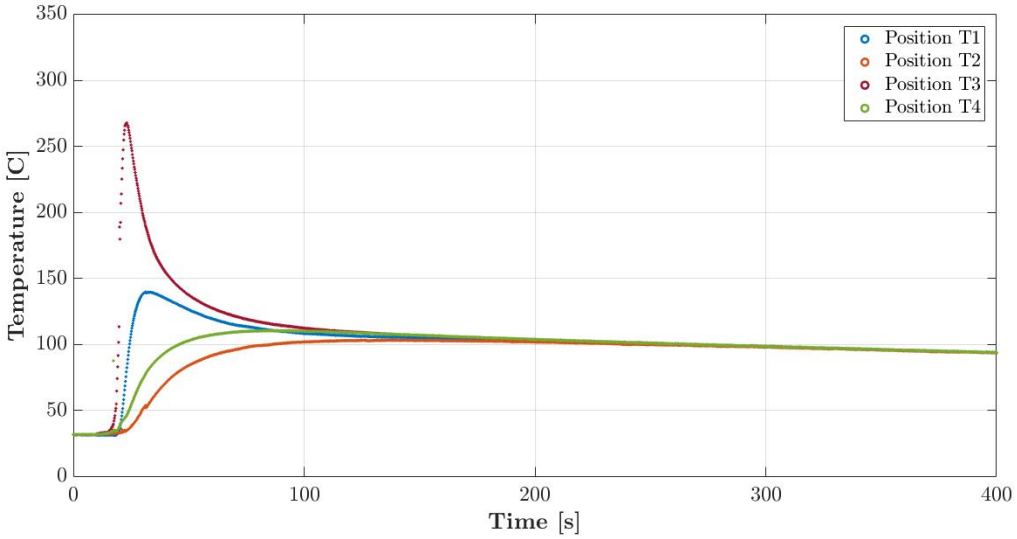

Figure 3.7: Temperature histories of four points on the base plate after the second pass

3.3.2. Distortion measurements

As mentioned earlier, a laser sensor was used to measure the distortion. In reality, the measured quantity is the distance of the point under consideration from the sensor. In this experiment, measurements were taken at three time moments:

- The first set of measurements was taken after the plates were tack welded together (δu_0).
- The second round of measurements was taken at a sufficiently large time period after the first welding run, so as to ensure that the specimen had cooled down (δu_1).
- The final measurements were taken at a sufficiently large time period after the second welding run (δu_2).

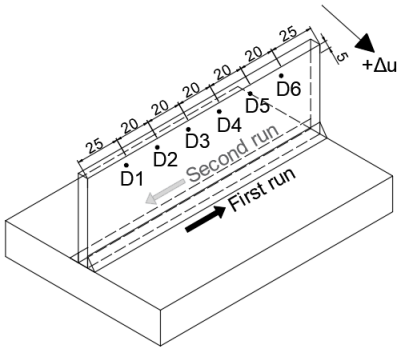

Figure 3.8: Sign convention for distortions

The distortion, Δu_1, is estimated as the difference between the sensor-to-surface distance of stage two and stage one, $\Delta u_1 = \delta u_1 - \delta u_0$. Similarly, distortion, Δu_2, is estimated as the difference between the sensor-to-surface distance of stage three and stage two, $\Delta u_2 = \delta u_2 - \delta u_1$. The horizontal distortion of the vertical plate after each welding pass is shown in Figure 3.9.

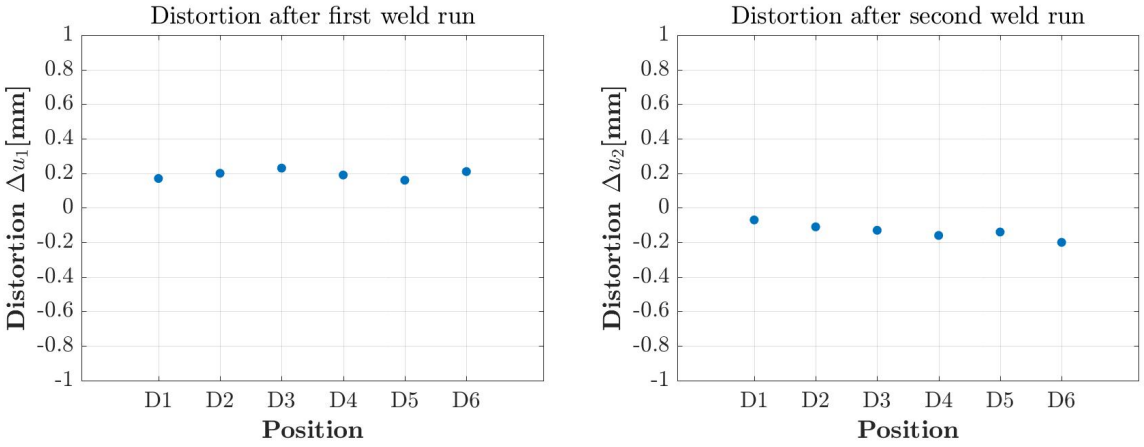

Figure 3.9: Distortion measurements

By evaluating the distortion measurements, some useful conclusions can be reached. Following the sign convention presented in Figure 3.8, positive values of distortion are expected after the first welding pass, and negative values after the second welding pass. This is verified by the measured distortions after both welding passes (Figure 3.9). The fact that the absolute value of distortion is smaller in the second case was expected, since, during the second run, the vertical plate is partly constrained by the first weld. Furthermore, from Figure 3.9b, it is observed that distortion gets bigger as the point of interest moves from position D1 to D6. This is fully explained by the changing constraint conditions during welding. Indeed, as shown in Figure 3.8, point D6 is located near the starting point of the second welding run. As the heat source is moving along the predicted direction, more and more filler material is deposited on the specimen, causing its free movement to be more restrained.

3.3.3. Voltage and Current measurements

During welding, current is measured by a current clamp. This measures the magnetic field caused by the passing current through the welding cable, and returns a voltage corresponding to $1mV/A$. Voltage is also measured during the whole procedure.

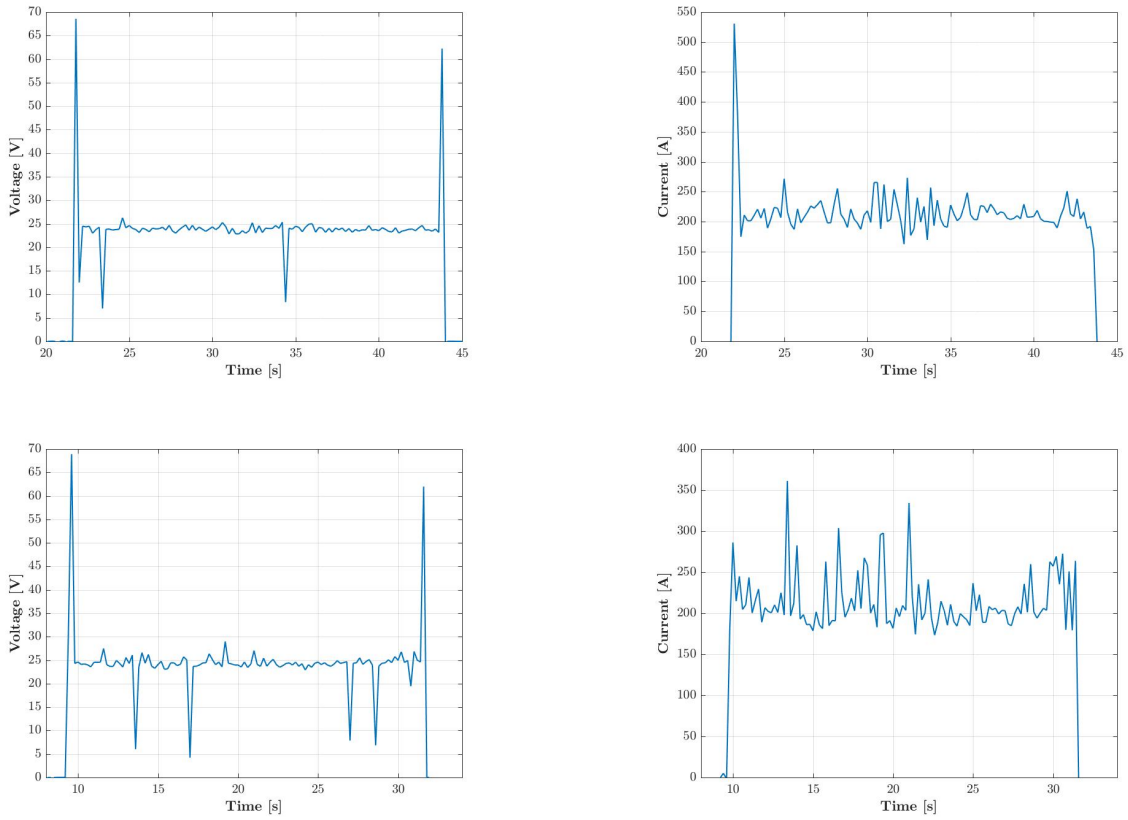

Figure 3.10: Voltage and Current measurements during first (a,b) and second (c,d) welding pass

3.3.4. Weld geometry

Metallurgical examination was conducted using a microscope on a cross section of the weld. This was hot mounted with Polyfast resin. The produced sample was then ground with sanding papers, polished and eventually chemically etched with a solution of nitric acid and alcohol (Nital 5%), in order for the microstructure of the welded steel plates to be revealed. With the help of a digital microscope, necessary geometrical parameters, such as the weld leg and throat dimensions, were measured (Figure 3.11). The microscopic images show clearly the fusion zone and the heat affected zone. The weld geometrical parameters were used in the weld modelling of the numerical analysis and the microscopic image was used to compare the fusion and heat affected zones that were predicted by the numerical modelling, to the ones that were formed in reality.

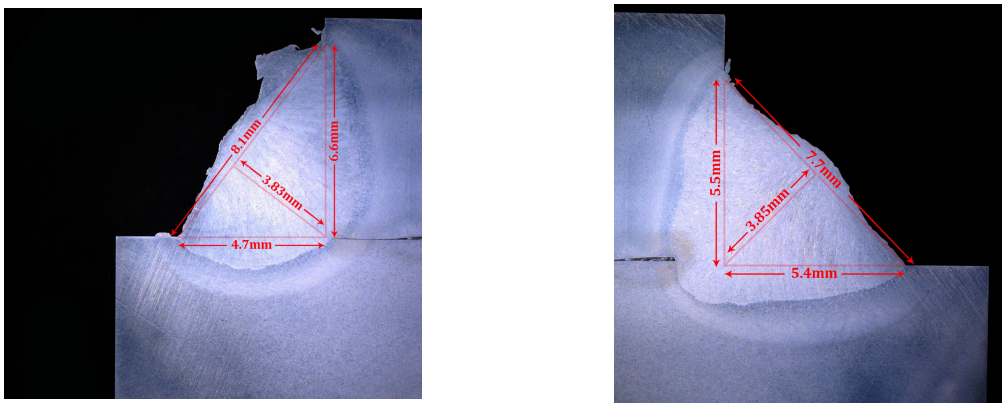

(a) First fillet weld

(b) Second fillet weld

Figure 3.11: Geometrical parameters of fillet welds

4

Simulation of small-scale experiment

In this chapter, the procedure of modelling a moving heat source in the Finite Element Analysis software, ABAQUS, is presented and verified by experimental results. The main point of interest is the appropriate simulation of the heat input due to the welding arc. This is achieved by conducting parametric studies to estimate the influence of the geometry of the moving heat source on the thermal response. This resulting model will serve as a numerical tool for the prediction of welding residual stresses in the following stages of the present work.

4.1. Introduction

The welding procedure is a complex phenomenon which contains electromagnetic, thermal, metallurgical and mechanical processes. Theoretically, an accurate prediction of welding distortions and stresses through numerical calculations would demand the consideration of all those physical phenomena. However, in case of numerical modelling, where time efficiency is a driving factor, it is necessary to separate the most influencing interactions among them.

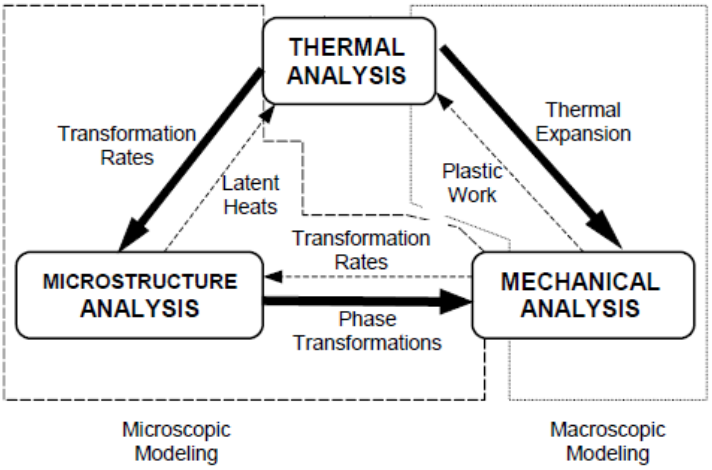

Figure 4.1: Work flow of residual stress computation [6]

Over the recent years, many studies have focused on the development of a reliable methodology of simulating the welding procedure and predicting residual stresses with the help of finite element software programs. Numerical modelling of welding could be divided in a microscopic and macroscopic part, as shown in Figure 4.1, where the influencing interactions are noted with a bold arrow. Some advocate that the prediction of microstructure evolution in a weld is necessary in a thermal-stress analysis of welds. Indeed, volumetric changes during phase transformations produce additional plastic strains. However, they are a significant factor mainly in high strength steels, while in low and mild carbon steels, the effect of microstructure changes

on distortions and stresses is small [6], [13]. For this reason, plasticity due to phase transformation in the microstructure is excluded from the scope of this study.

Macroscopic modelling treats distortions and stresses as a thermomechanical problem. During welding, a local and time-related heat concentration provokes thermal strains. On the contrary, the temperature field is not significantly affected by the stress field. In other words, the heat due to plastic deformation of the connected plates, is negligible compared to the heat generated by the arc. Following this reasoning, a basic assumption in the modelling of the welding procedure is the sequential coupling between the thermal and mechanical analysis [27]. In that sense, two separate analyses are conducted, a transient thermal and a mechanical analysis. The nodal temperatures calculated by the thermal analysis are inserted in the mechanical analysis as a predefined temperature field.

4.2. Mesh

A basic characteristic of any finite element analysis is the type of elements used. ABAQUS offers a wide range of elements, providing great flexibility in modelling. A common classification of elements is performed based on the family in which they belong. This term is the broadest category of classification and separates elements of different geometry and type of behaviour.

As mentioned, the workflow of this thesis involves a thermal and a sequentually coupled mechanical analysis. Those types of analyses, require elements with different degrees of freedom. Thus, the thermal analysis is performed using elements with temperature degrees of freedom. Specifically, 8-node linear heat transfer bricks (DC3D8) for the plates and 6-node linear heat transfer triangular prisms (DC3D6) at the welds. Accordingly, in the mechanical analysis, 8-node linear 3D stress bricks (C3D8R) are used for the plates and 6-node linear triangular 3D stress prisms (C3D6) are used in the welds, containing translational and rotational degrees of freedom.

In any finite element software, proper meshing is the key to accurate results. As a general rule, a finer mesh leads to more reliable solutions, at the cost of significantly increased computational time. On the other hand, a coarser mesh requires less amount of computer memory and run time, but is more likely to provide inaccurate results. Determining the balance between what is qualitatively acceptable and time efficient is crucial for the user.

During welding, significant temperature variations are observed near the weld seam. Therefore, it seems necessary to adopt a dense mesh in the region near the weld, where the thermal gradients are higher, so as to ensure an accurate prediction of residual stresses [21]. In order to reduce the required computational time, without endangering the accuracy, a finer mesh is constructed near the weld, at a distance of 10mm from the weld roots. Elements with a length of $1.25mm$ were adopted in the weld area and $5mm$ in the rest of the specimen, for the longitudinal direction. Between the two mesh configurations, a transition layer of 4.5mm is constructed, with a 4:1 ratio (Figure 4.2).

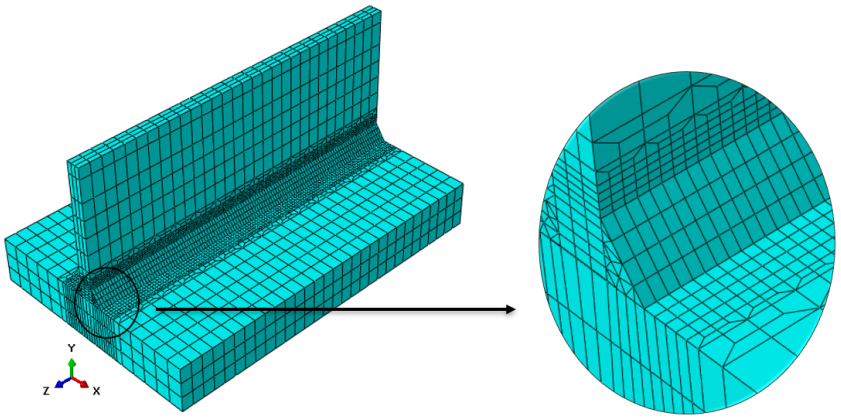

Figure 4.2: Mesh transition with a 4:1 ratio

4.3. Material Properties

During welding, high temperatures are observed near the weld seam. The influence of elevated temperatures on the thermomechanical material properties has to be taken into account. For a conventional structural steel, like S355, the thermal material properties under elevated temperature are calculated according to chapter 3 of EN 1993-1-2:2005 [1].

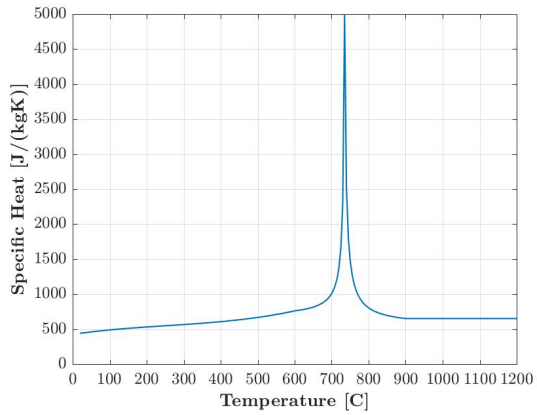

(a) Specific heat

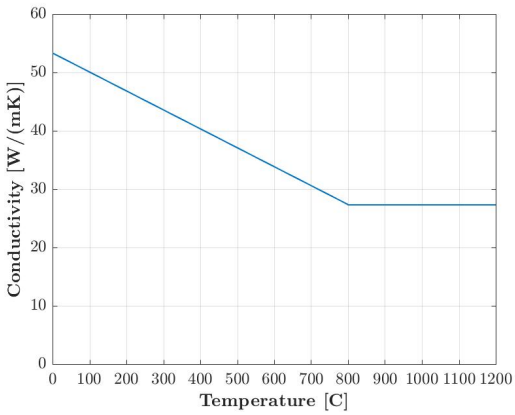

(b) Thermal conductivity

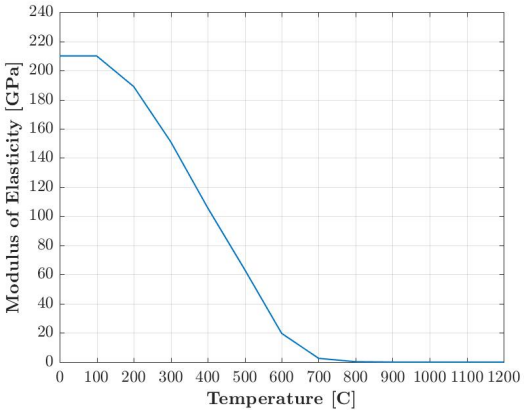

(c) Modulus of elasticity

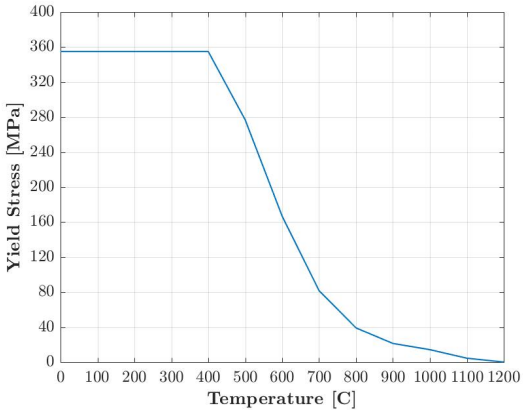

(d) Yield stress

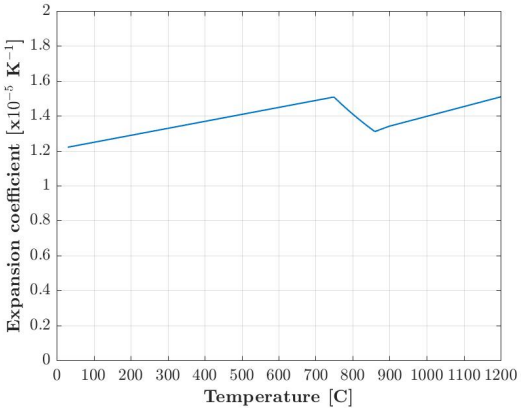

(e) Expansion coefficient

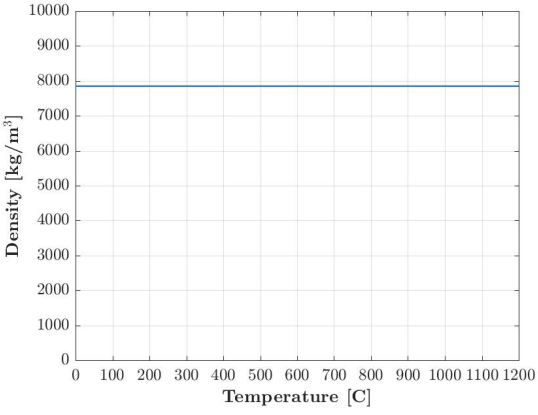

(f) Density

Figure 4.3: Thermal and mechanical properties under elevated properties

In EN 1993-1-2:2005 [1], the stress strain relationship at elevated temperatures is fully described (Figure 4.4). The proposed material model is ideally plastic, without strain hardening. The mechanical response of the material is also characterized by the Poisson ratio, which has a constant value of 0.3, independently of the temperature.

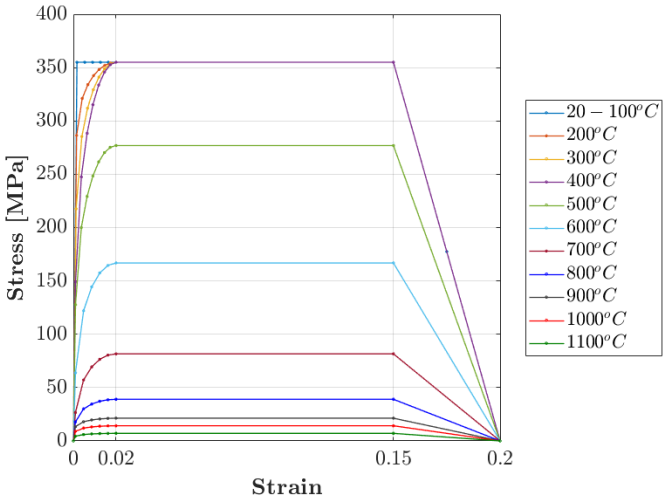

Figure 4.4: Stress-strain relationship for various temperature levels [1]

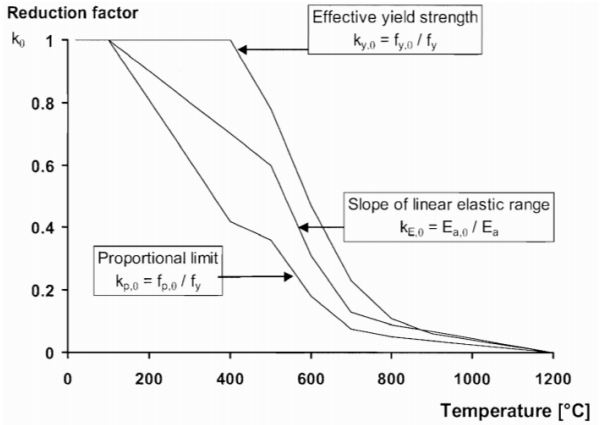

Figure 4.5: Reduction factors for proportionality limit, yield stress and modulus of elasticity, according to EN 1993-1-2:2005 [1]

4.4. Element activation

The mechanical behaviour of the welded components is significantly affected by the material behaviour under higher temperatures, since the area close to the weld is subjected to large and rapid temperature changes. Filler material deposition is a phenomenon related to weld solidification, which influences the mechanical response of the welded components.

During a welding process, the filler metal is continuously deposited on the welded joint, connecting the base material in a gradual manner. The specimen's movement is constrained more and more, as the filler metal deposition causes an accumulated rigidity. In order for this phenomenon to be incorporated into the numerical analysis, a common practice is the implementation of the birth and death technique. According to it, the weld bead is divided in segments, to simulate the deposition of the filler material with time. The terms "death" and "birth" refer mainly to the deactivation and subsequent activation of weld segments one by one, indicating the deposition of the filler material along the welding line. The model must be built, having all necessary elements, even those that will be removed at a later stage. In the beginning of the analysis, all weld

segments are removed, while in every following analysis step, a segment is added. Every time a weld segment is activated, a body heat flux is applied, representing the heat input due to welding. The duration of every activation step depends on the welding speed. When every segment has been activated, a sufficiently large cooling step has to be applied, in order to enable the component to return back to room temperature.

The procedure of birth and death is included in ABAQUS through the *Model Change* command. Before the removal step, the forces/fluxes that the removed parts exert on the remaining elements, at the nodes of their boundaries, are stored. During the removal step, these forces are gradually decreased to zero, meaning that the effect of the element removal is active only after the completion of the step. Removed elements are excluded from the analysis and no further calculations are performed for them, unless they are reactivated. At the moment of reactivation, the added elements are assumed to be free of any strain and stress [32].

4.5. Thermal Analysis

The temperature field history is calculated through a transient thermal analysis, which is based on the heat conduction formulation and adopts temperature dependent thermal properties [4]. Thermal analysis can be divided in three components: heat input by the welding arc, heat transportation and heat losses (Figure 4.6). The biggest part of the generated energy from the arc is distributed within the body through conduction, while the rest is lost to the surrounding environment through radiation, convection and conduction to contacting bodies.

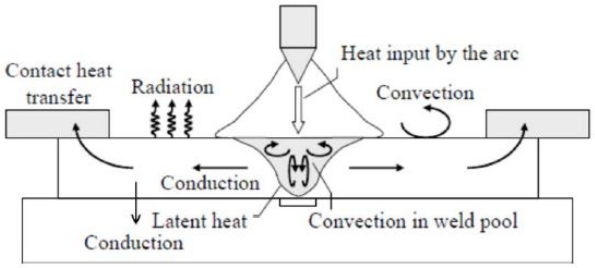

Figure 4.6: Heat balance during welding [15]

The transient temperature distributions during welding are a function of time t and spatial coordinated x, y, z and are determined by the non-linear heat transfer equation [4]:

$$c\rho\frac{\partial T}{\partial t} = k\left(\frac{\partial^2 T}{\partial x^2}\right) + k\left(\frac{\partial^2 T}{\partial y^2}\right) + k\left(\frac{\partial^2 T}{\partial z^2}\right) + q \tag{4.1}$$

In equation 4.1, c, ρ, T, t represent the specific heat capacity ($J/(kg°C)$), density (kg/m^3), temperature ($°C$) and time (s). The internal heat generation rate (W/m^3) is represented by q and thermal conductivity ($W/(m°C)$) by k. This equation proves that the necessary material properties for a thermal analysis are density, specific heat capacity and thermal conductivity. It has been observed that density shows a weak dependency on temperature variations, while the rest of the material properties are highly affected by temperature gradients [4].

In numerical analyses, the heat input is usually treated as a body or surface heat flux, applied on the workpiece. The energy input, Q, generated by the heat source is calculated by:

$$Q = \eta U I \tag{4.2}$$

where η is the thermal efficiency of the welding method, U is the arc voltage [V], and I is the electric current [A] used by the welding process.

The thermal efficiency of the welding method is mainly related to the arc efficiency, depicting the fraction of the total arc energy that is transferred to the welded parts. The arc generated energy is not fully transmitted to the workpiece, since a part of it is lost into the surrounding environment. Similarly, a part of the net energy that is transferred to the parent material is used for melting of the fusion zone, while the rest is lost

to the adjacent parent material, through thermal conduction. This fraction of energy influences the creation of the heat affected zone (HAZ) and contributes to the heating of the base metal [14]. The arc efficiency is a characteristic of the applied welding process, that shows little variation for different values of the current, I. For consumable electrode processes, as Gas Metal Arc Welding that was used in this model, the arc efficiency ranges from 0.8 to 0.9 [14].

4.5.1. Heat source model

The size and shape of the heat source has been under investigation for many years. A popular analytical method was introduced in the late 1930s, when Rosenthal suggested the simulation of the heat source as a concentrated point or line, at which the temperature is infinite. Many researchers showed, however, that the temperature predictions near the fusion and heat affected zone were subjected to serious errors, while the accuracy was improved for regions far from the weld [16]. Today, Rosenthal's model is replaced by numerical methods which consider a finite heat source, distributed over an area. Pavelic et al. suggested the distribution of flux in a circular disc on the surface of the workpiece, following the Gaussian distribution [16],[6]. Up to date, the most commonly used heat source model is the one developed by Goldak et al., which adopts a non-axisymmetric, three dimensional moving heat source in the form of two ellipsoidal shapes [16].

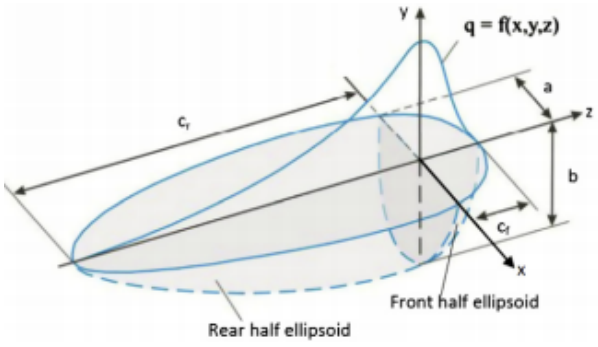

Figure 4.7: Double ellipsoid heat source configuration [18]

In the double ellipsoid heat source model, developed by Goldak et al. [16], the front and rear half of the source are the quadrants of two different ellipsoidal shapes (Figure 4.7). The power density distribution of the front quadrant is defined as:

$$q_f(x,y,z) = \frac{6\sqrt{3}f_f Q}{\alpha b c_f \pi\sqrt{\pi}} e^{-3x^2/\alpha^2} e^{-3y^2/b^2} e^{-3z^2/c_f^2} \tag{4.3}$$

Similarly, for the rear quadrant, the following applies:

$$q_r(x,y,z) = \frac{6\sqrt{3}f_r Q}{\alpha b c_r \pi\sqrt{\pi}} e^{-3x^2/\alpha^2} e^{-3y^2/b^2} e^{-3z^2/c_r^2} \tag{4.4}$$

In equations 4.3 and 4.4, Q is the power input in Watt and the parameters α, b, c_f, c_r are the radial dimensions of the molten zone to the side, underneath, at the front and behind the arc (Figure 4.7). Those parameters can be fixed by directly measuring the relevant dimensions on a cross section of the molten zone. Parameters α and b which correspond to the width and depth of the heat source, are related to the dimensions of the weld's cross section. Regarding the fractions f_f and f_r of the heat deposited in the front and rear part of the ellipsoids, they should satisfy the condition $f_r + f_f = 2$. Values of $f_f = 0.6$ and $f_r = 1.4$ are usually considered, since they have been proved to yield a sufficient correspondence between experimental results and simulation estimations of the thermal history [16]. The relation between parameters c_f and c_r can be estimated by considering that the heat fluxes q_f and q_r have to be equal at the origin of the coordinate system. This requirement demands that $c_r = 2.33c_f$, while, as suggested in the literature [16], c_f can be considered approximately as equal to one half of the weld width. In the present work, Goldak's model has been used to simulate the moving heat source. The parameters related to the size of the welding arc are calibrated based on experimental results.

In ABAQUS, heat input can be defined as a concentrated, surface or body heat flux. In order to implement the double ellipsoidal heat source model, heat input was introduced as a body heat flux, using DFLUX subroutine. Equations 4.3 and 4.4 are fully described in the subroutine code. At each time moment, the arc position is calculated based on the elapsed welding time and the heat flux is computed at each point, depending on its position with respect to the moving arc. Input parameters of the subroutine are the arc voltage, current, efficiency and travel speed, as well as the geometric parameters described in eqations 4.3 and 4.4. Arc voltage and current for each pass were derived from experimental data, as the average values of the measured quantities.

As mentioned earlier, the adoption of Goldak's moving heat source model, includes the determination of parameters a, b, c_f, c_r of the welding arc. In the present study, an investigation of the optimal value of the aforementioned parameters has been carried out. Thanks to the measurements on the weld cross section, as described in Chapter 3, a realistic estimation of the geometry parameters a, b, c_f, c_r has been achieved.

The aim of the suggested model is the application in any weld with known dimensions, even when a microscopic image of the cross section is not available. Following the information of Figure 4.7, the origin of the coordinate system of the heat source is applied at the middle of the fillet weld's hypotenuse, while x and y coordinates are parallel and vertical to it (Figure 4.8). This is achieved by rotating the local coordinate system, using the rotation matrix in the DFLUX subroutine. Parameters a, b were assumed to be proportional to the weld width and throat respectively. In every analysis, each parameter was changed individually, so as to evaluate its impact on the temperature field. By comparing the experimental and simulation results, adjustments have been made on the adopted values.

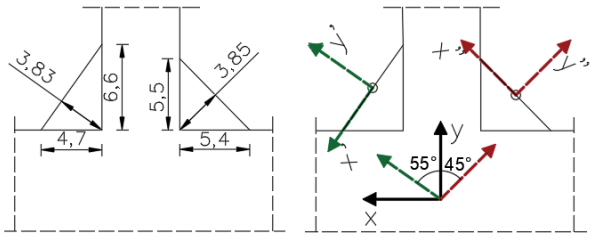

Figure 4.8: Weld geometry and rotation of coordinate system. The left weld represents the weld produced during the first run, and the right weld represents the one that was produced last

The final parameter values are shown in Table 4.1. It has been concluded that the width parameter can be accurately described by half the weld's width, the depth parameter is linked to the weld's throat, while length parameters are related to the weld width, as described previously. These have been used as the reference values for the performance of a parametric study, aiming at evaluating the influence of each variable on the thermal output. This study is presented below, only for the first welding run, since the response of the model was similar for both welding stages.

	First pass	Second pass
Current [A]	213.94	214.10
Voltage [V]	23.59	23.77
Efficiency	0.85	0.85
Width a [mm]	4.05	3.85
Depth b [mm]	3.83	3.85
Front c_f [mm]	4.05	3.85
Back c_r [mm]	9.44	8.97
Welding speed [mm/s]	7	7

Table 4.1: Heat source parameters

Influence of width parameter

In Figure 4.9, the temperature evolution with time, for four positions of the base plate is presented. The results are plotted for two analyses; one where the width parameter is doubled and one where it is considered half of the adopted value α. As indicated in Figure 4.9, an increase in the value of α leads to increased temperatures and vice versa.

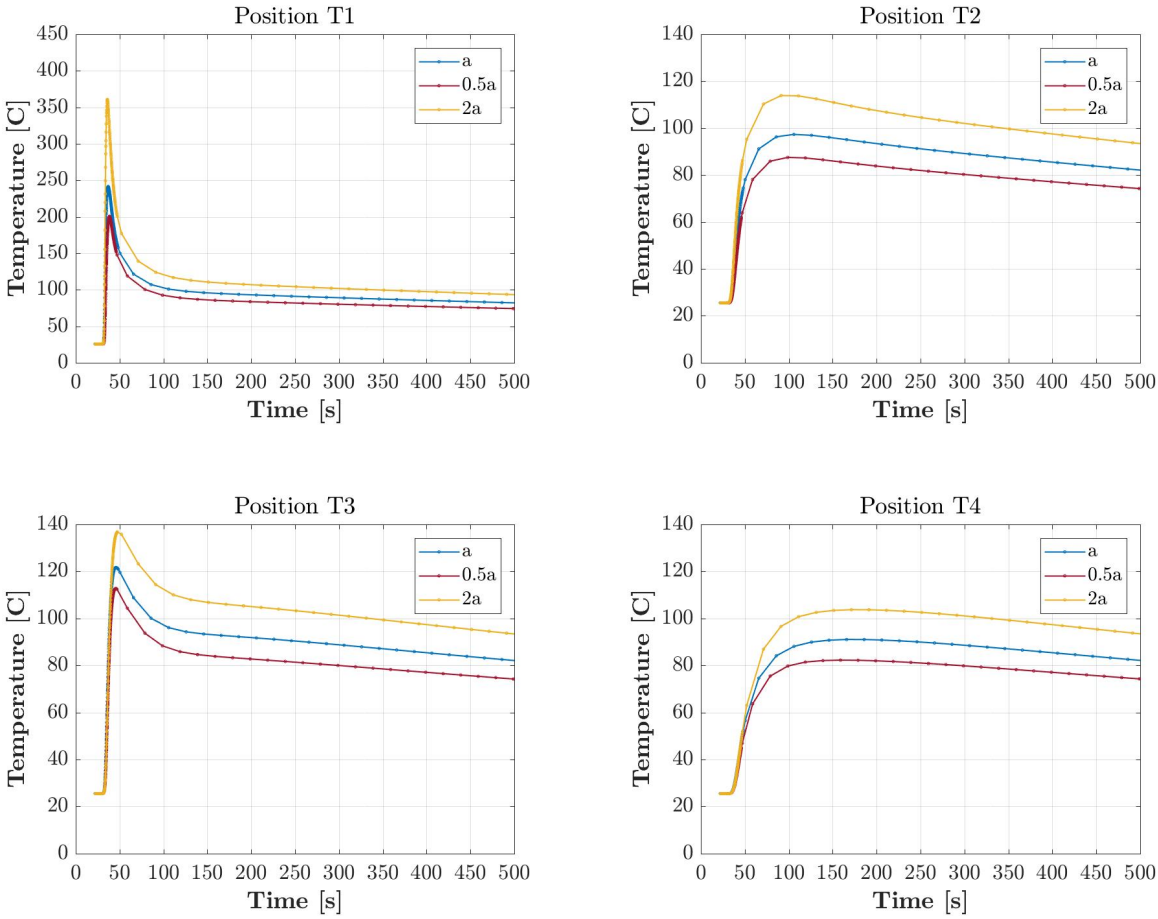

Figure 4.9: Influence of width parameter, α, on the temperature

Due to the high deviation on temperature results for different values of α, the distribution of temperature along the base plate's width is also evaluated, as shown in Figure 4.10, where results are plotted for two separate time moments during welding. Figure 4.10a corresponds to time moment t_1, when the heat source is close to the path under investigation, while Figure 4.10b represents time moment t_2, when the heat source has moved away. In the beginning of welding (Figure 4.10a), high temperatures are predicted near the weld area, while as the cooling down process initiates (Figure 4.10b), the temperature of these points drops. This is accompanied by an increase of the temperature of points further from the weld, as a result of the heat trasportation in the plate. In order to quantify the observed deviations, Figure 4.11 shows the percentage difference of the predicted temperature along the base plate's width when compared to the reference case. When the heat source is close to the investigated path (time t_1), the influence of the width parameter is more enhanced near the weld, than away from it. Doubling the value of the width parameter results in a temperature increase that can reach 75%, while dividing its value by two leads in a temperature drop up to 45%. Moreover, in the first case, the length over which the temperature is affected is larger, since by increasing the arc width, more points are under the direct influence of the heat source. Indeed, changes are observed up until a distance of $30mm$ from the weld, while in the second case, this distance is estimated at approximately $25mm$. At a later time moment (t_2), when the heat source has moved away from the points of interest, the influence of the width parameter on the temperature decreases and appears to be more uniform along the plate's width. When the value of α is double the reference value, temperature is 25% higher until a distance of

$20mm$ from the weld toe, and reaches a 20% difference at the end of the plate. When α is twice as small, the predicted temperature is approximately 15% lower until a distance of $20mm$ from the weld toe and 5% lower at the end of the plate.

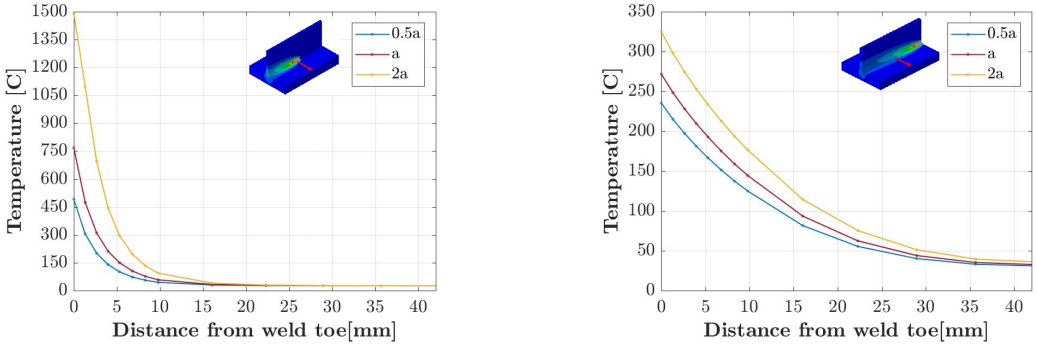

(a) Temperature distribution along the plate's width when the heat source is close (time t_1)

(b) Temperature distribution along the plate's width when the heat source is away (time t_2)

Figure 4.10: Temperature distribution along the width of the base plate for different values of width parameter

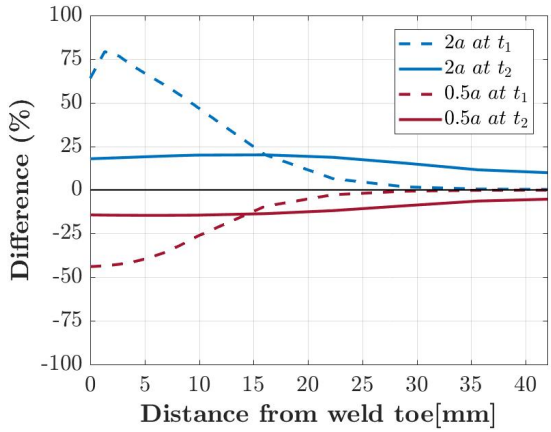

Figure 4.11: Percentage difference of predicted temperature when the width parameter is double or half of the reference value, α. Results are plotted for time moments t_1, t_2, with $t_1 < t_2$

Influence of depth parameter

In Figure 4.12, the temperature distribution with respect to time is plotted for two variations of the adopted parameter with respect to its reference value. From this it is observed that an increase in the adopted value leads to an overall increase of the maximum reached temperature for points further from the weld (T2-T4), while it does not severely affect it for points close to the weld (T1). During the cooling down phase, the temperature appears to be higher, in all investigated positions, when the depth parameter is increased.

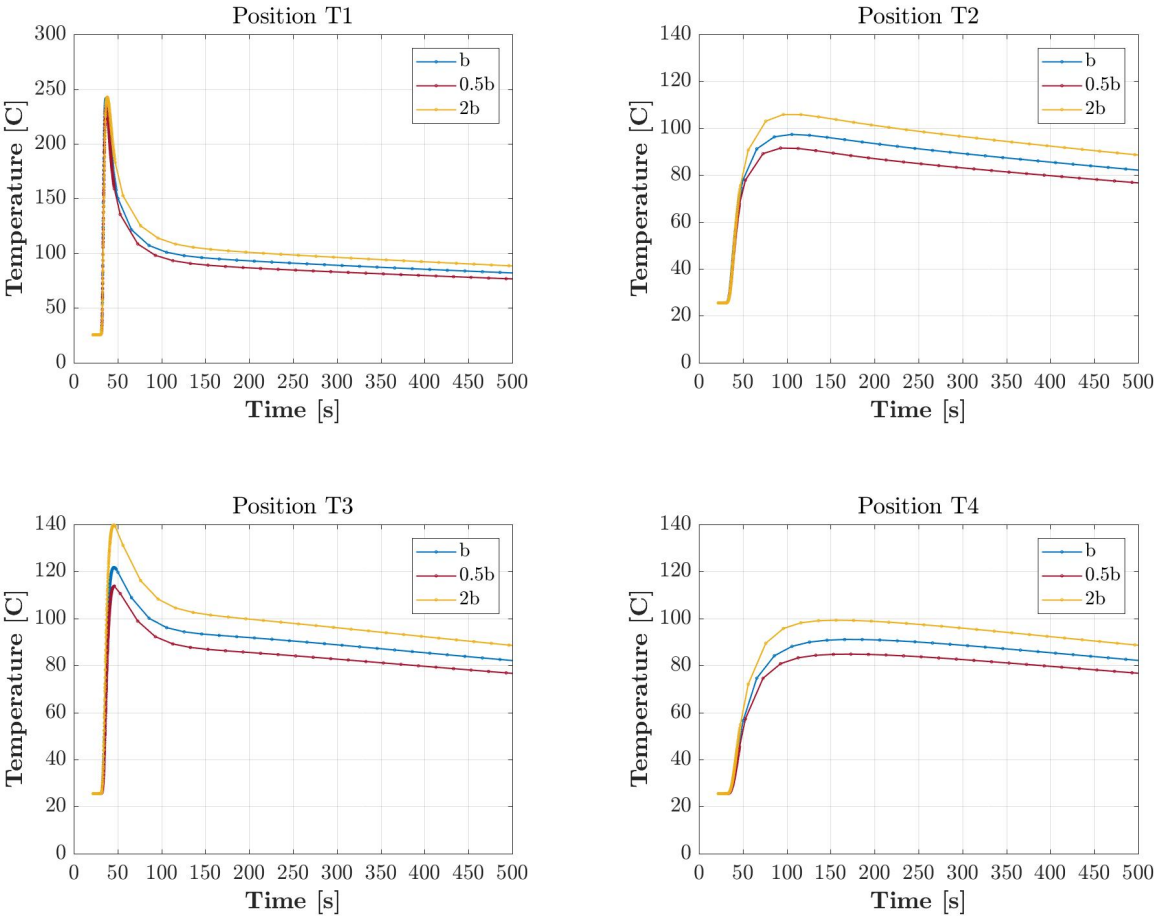

Figure 4.12: Influence of depth parameter, *b*, on the temperature

The temperature distribution along the plate's width is plotted in Figure 4.13, for two time moments, as in the previous case. In both considered time moments, the difference in the predicted temperature is small. In Figure 4.14, the percentage difference of the predicted temperature with respect to the reference analysis is given. For time moment t_1, when the heat source is close to the investigated path, temperature seems to be up to 10% higher when the parameter is half the reference value. On the other hand, the predicted temperature when the parameter is doubled seems to be 10% lower. This can be explained by the more enhanced heat distribution towards the plate's thickness than towards the surface, when the depth parameter is higher. The effect of the adopted value on the temperature seems to extend over a larger distance from the weld, when the parameter is higher. At a later time moment, during cooling (t_2) and as the heat transportation has already initiated, the influence on the material temperature is reversed. In this case, it seems that higher temperature is reached in case of a larger depth parameter. Near the weld area, up to 10% larger temperature values appear close to the weld, when the parameter is doubled and up to 10% smaller when the parameter is twice as small. In both cases, points located away from the weld are less significantly affected.

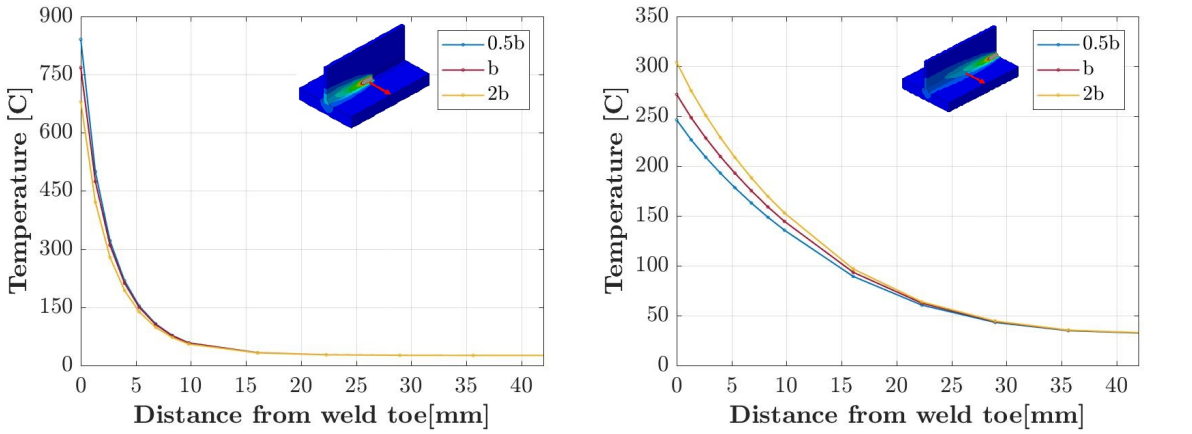

(a) Temperature distribution along the plate's width when the heat source is close (time t_1)

(b) Temperature distribution along the plate's width when the heat source is away (time t_2)

Figure 4.13: Temperature distribution along the width of the base plate for different values of depth parameter

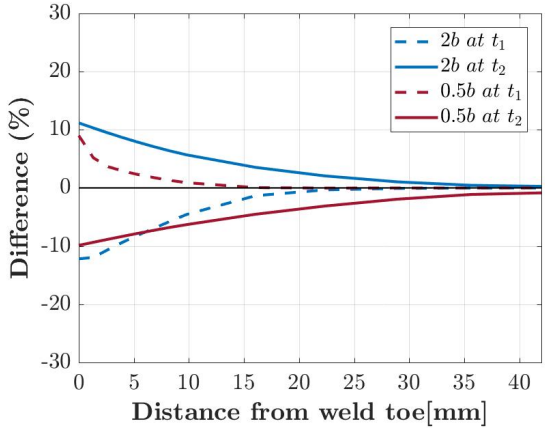

Figure 4.14: Percentage difference of predicted temperature when the depth parameter is double or half of the reference value, b. Results are plotted for time moments t_1, t_2, with $t_1 < t_2$

Influence of length parameter

In Figure 4.15, the temperature distribution with respect to the elapsed time is plotted for variations in the length parameter. Changes of the radial dimensions, c_f and c_r, in the front and back of the weld pool have a negligible influence on the final temperature distributions.

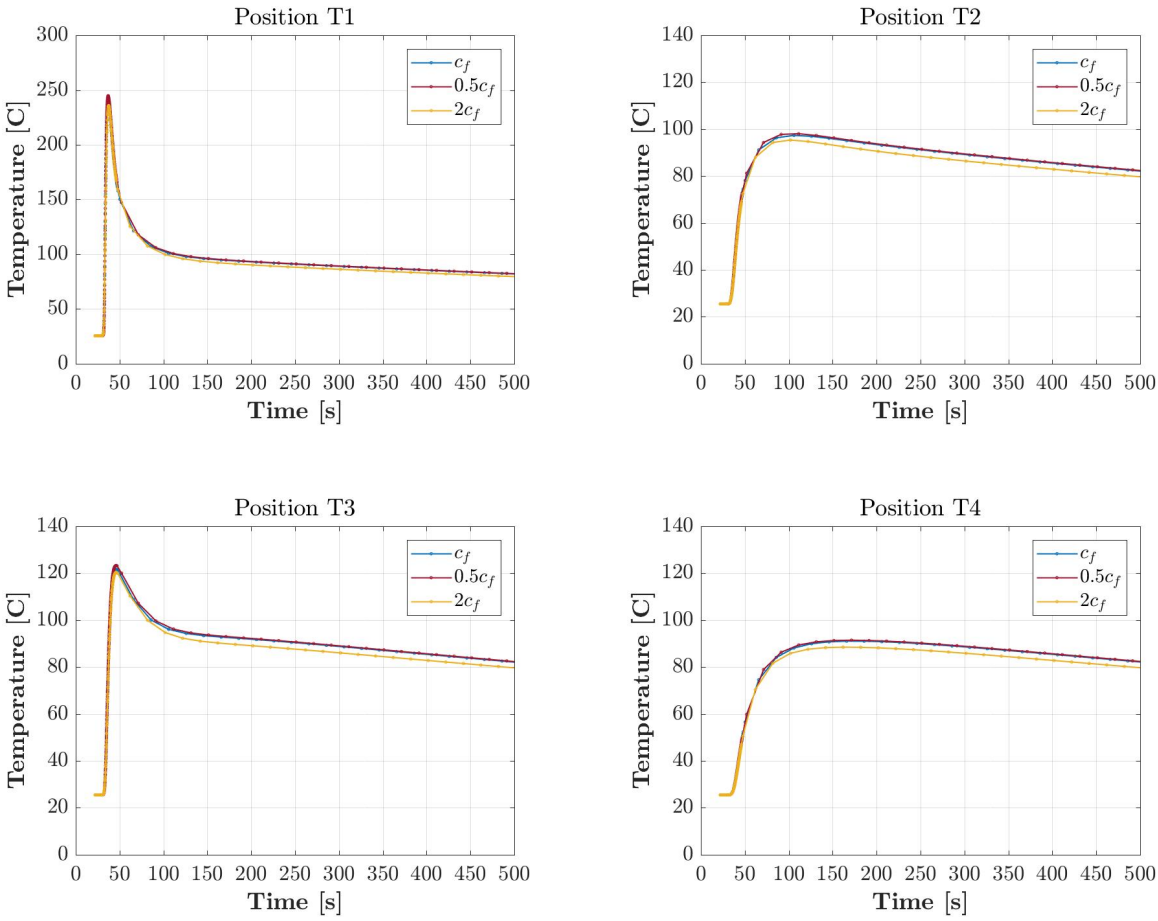

Figure 4.15: Influence of length parameter, c, on the temperature

4.5.2. Heat losses

Welding causes an increase of the body's temperature, which slowly decreases overtime until room temperature is reached again. This reduction is attributed to energy transfer within the body in the form of conduction, but also to heat losses due to convection and radiation to the surrounding air [33].

Thermal losses due to convection are described by Newton's law of cooling:

$$q_c = h_c(T - T_\infty) \tag{4.5}$$

where h is the heat transfer coefficient in case of convection, T is the surface temperature and T_∞ is the room temperature. Heat loss due to radiation is defined as:

$$q_r = \epsilon\sigma_B(T^4 - T_0^4) \tag{4.6}$$

where ϵ is the radiation emissivity, σ_B is the Stefan-Boltzmann constant, equal to $5.67{\cdot}10^{-8} W m^{-2} K^{-4}$, T is the surface temperature and T_0 is the room temperature. In ABAQUS, convection and radiation are considered by applying the surface film condition and surface radiation commands. The former is defined through the film coefficient, representing the heat transfer coefficient (Equation 4.5), and the sink temperature. The radiation losses are defined by the emissivity (Equation 4.6), and the sink temperature. The values of both coefficients are fixed by comparing experimental and simulation results. Thus, the film coefficient is assigned the value of $10 W/m^2 K$, the emissivity is set equal to 0.5, while the room temperature was set at $25.5^o C$, as measured by the thermocouples.

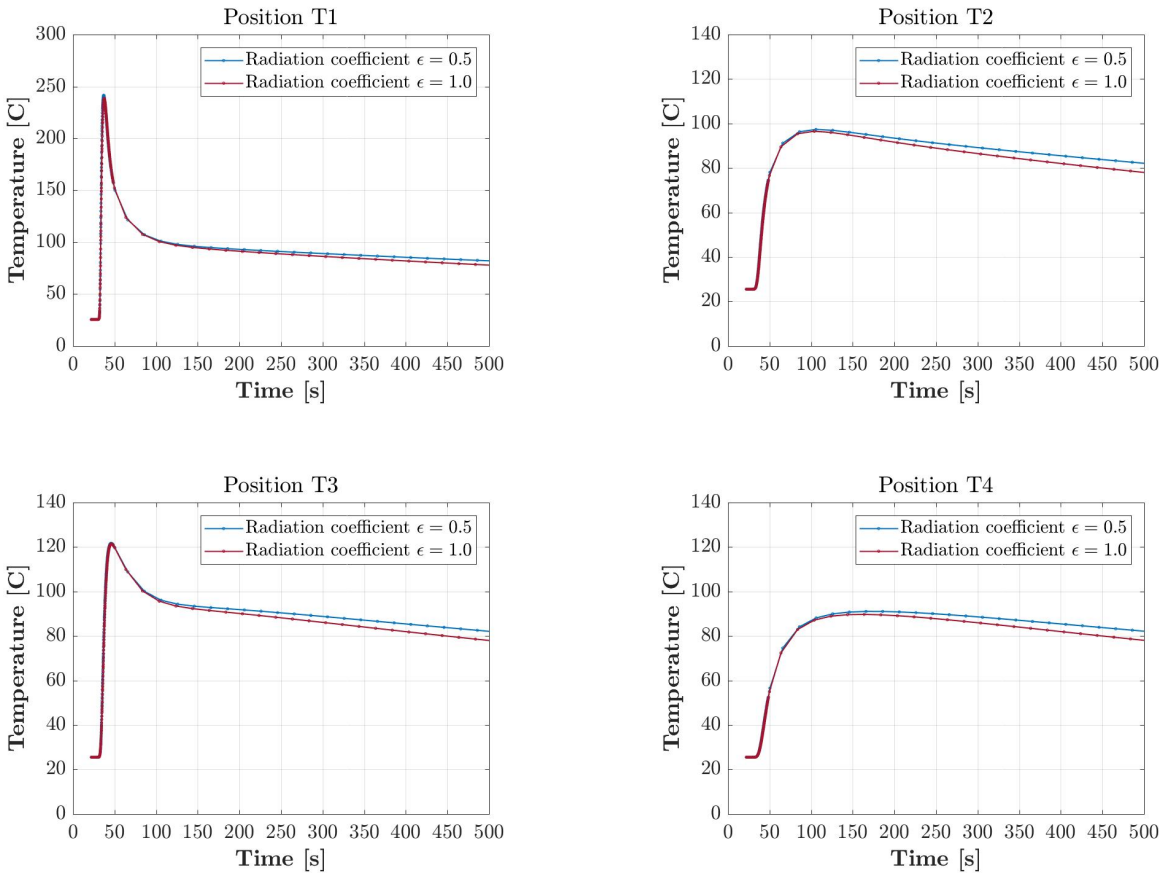

Figure 4.16: Influence of radiation coefficient, ϵ, on the temperature

As it can be seen in Figures 4.16, 4.17, thermal losses do not affect the maximum temperatures on the plate, but mainly the cooling rate, after the completion of the welding procedure. Between the two mechanisms,

it appears that convection losses have the most impact on the temperature field. However, even in the case where the heat transfer coefficient is $20W/m^2K$, the cooling down rate is low.

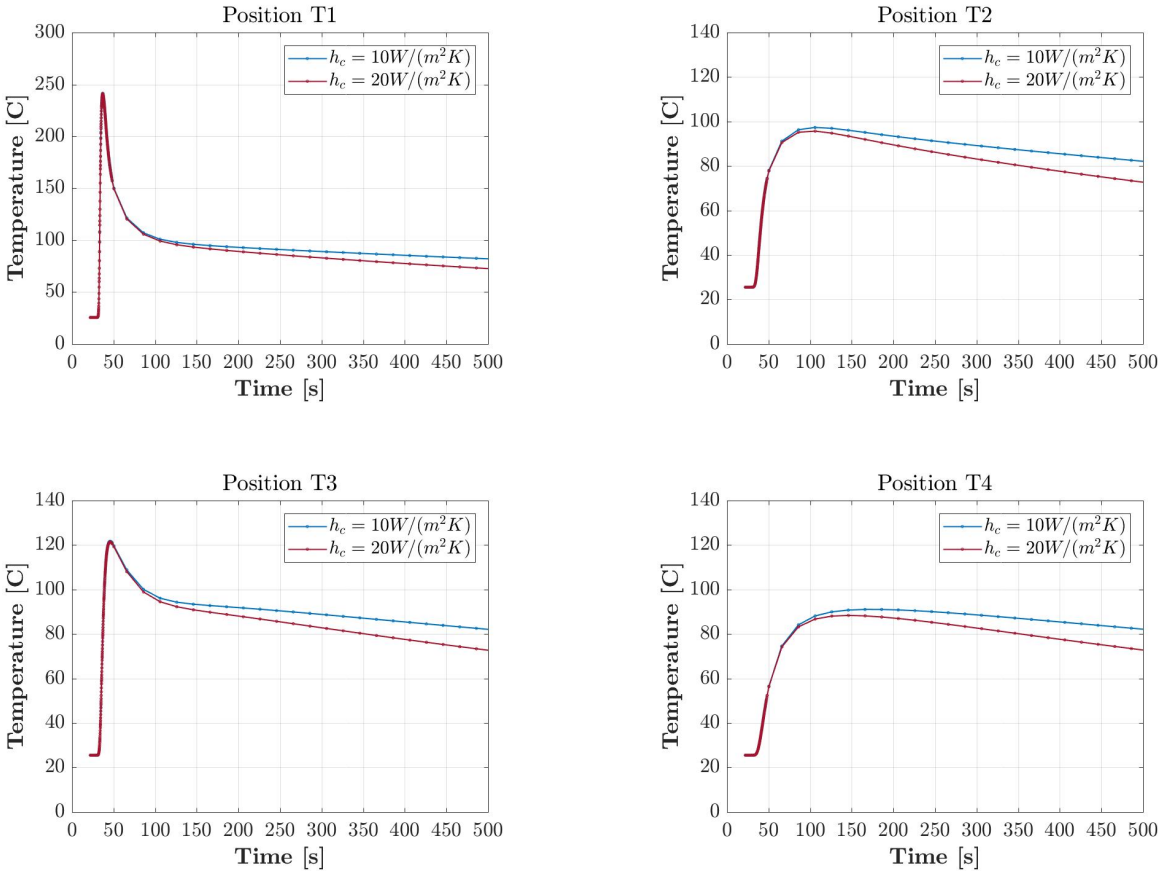

Figure 4.17: Influence of heat transfer coefficient, h_c, on the temperature

4.6. Mechanical Analysis

After solving the heat conduction problem independently from the mechanical problem, the temperature histories are used as input information for the mechanical analysis. In a numerical analysis, those histories are inserted into the subsequent mechanical analysis as predefined fields. The temperature time histories are read at the nodes and then are interpolated within each element. The connection between thermal and mechanical analysis lies also in the temperature dependent thermo-mechanical properties and the thermal expansion [13], [6], [4].

In a thermomechanical analysis, apart from the elastic, plastic and thermal strain, phase transformations generate two additional strains: transformation strains due to volumetric changes and transformation plasticity strains. In case of low carbon, mild steel, phase transformations have a negligible influence on the welding residual stresses and distortions [12], [13]. As a result, the total strain rate can be divided in three components: the elastic, plastic and thermal strain rate. For the modelling of the elastic strain, Hook's law with temperature dependent modulus of elasticity is applied. An elastoplastic model (according to EN 1993-1-2:2005[1]) with the von Mises yielding criterion is adopted for the modelling of plasticity.

4.6.1. Mechanical boundary conditions

In mechanical analyses, the constraint conditions influence significantly the distortions and stress fields. In order for the distortion results to be as realistic as possible, the mechanical boundary constraints represent the actual clamping conditions.

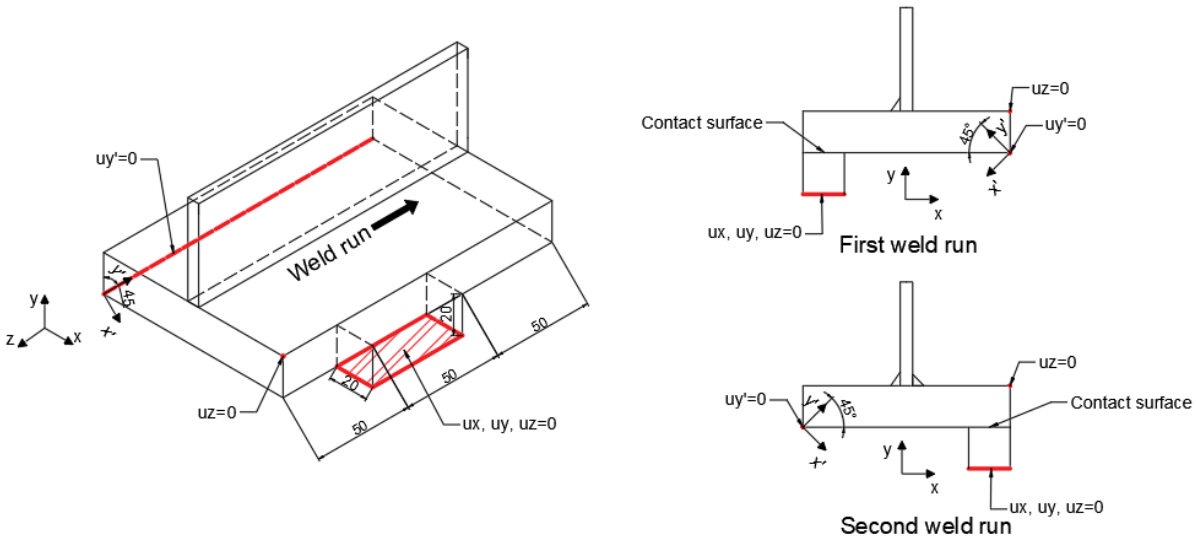

Figure 4.18: Mechanical boundary conditions of the numerical analysis

As it was described in Chapter 3, the specimen was positioned on the welding table at an angle of 45^o (Figure 3.2). During the experiment, the bottom plate is supported at two locations. Towards the welding side, the specimen was in contact with the inclined support, only at a certain area. This support was included in the mechanical analysis and it was fixed at its bottom, along all three directions. In the interface between the support and the plate, the normal and tangential behaviour of the surface-to-surface contact were defined. The normal behaviour was described by the "Hard Contact" interaction, so as to prevent the penetration of one surface into the other during the analysis. The tangential behaviour described the friction between the surfaces, by assuming a friction coefficient of 0.6. On the opposite to the weld run side, the specimen was in contact with the welding table, along the entire plate edge. In order to consider the inclination of the specimen in the numerical model, a local coordinate system was created for this edge and the movement of the plate along the local, y direction was constrained. In order to avoid rigid body motion, the movement of the specimen along the longitudinal, z direction was constrained at one point of the bottom plate (Figure 4.18). The mechanical constraints additionally included the restraint of the vertical plate due to spot welding. The spot welds were modelled so as to tie together the two plates at the points of application.

4.7. Results

4.7.1. Thermal analysis

The temperature distributions, as derived after applying the proposed values, are shown in Figures 4.19, 4.20.

A good agreement can be observed between experimental and numerical data. In the case of the first welding run, differences are observed in thermocouples T1 and T2. This is mainly attributed to erroneous measurements at the first stages of the welding procedure. Indeed, during the first seconds an abrupt increase of temperature is measured, which can be explained by sparks and spattering from the welding arc to the area near the thermocouples. In thermocouples T3 and T4, the maximum temperature difference are 10^oC and 5^oC, which are acceptable.

The comparison of data for the second welding run shows bigger agreement than the first one. No faulty measurements have been observed during the experiment and the deviations between numerical and experimental results are insignificant.

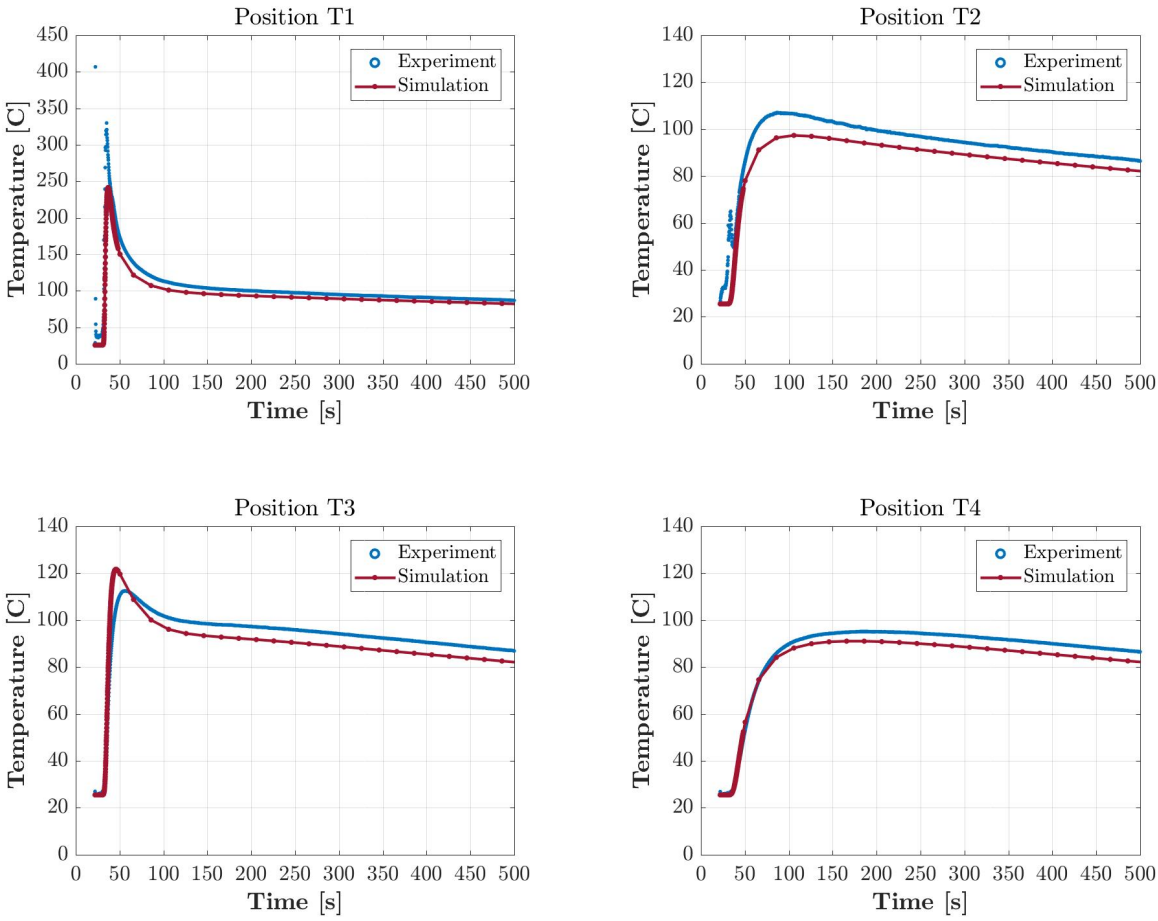

Figure 4.19: Comparison of experimental and simulation results for the first welding run

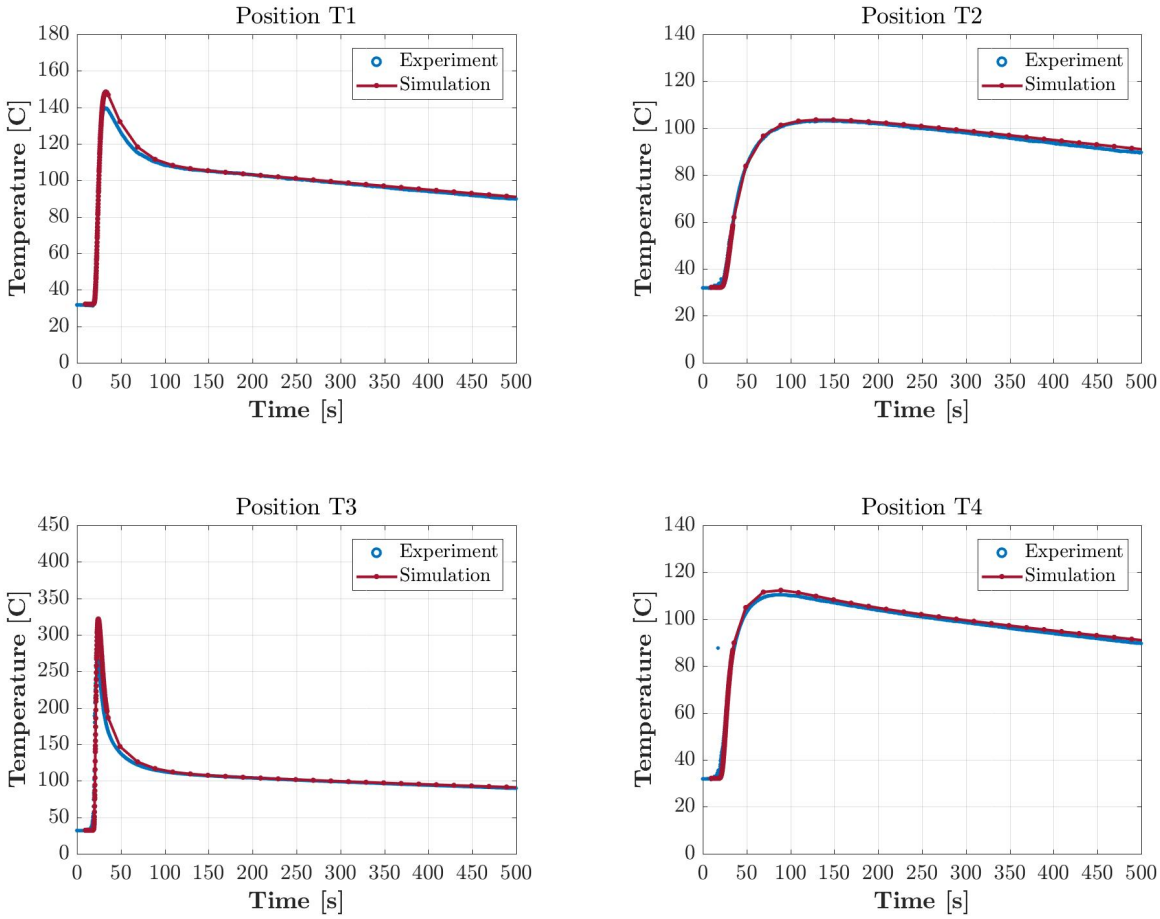

Figure 4.20: Comparison of experimental and simulation results for the second welding run

The validity of the thermal results is also verified by comparing the cross section of the weld, as seen through the microscope, with the isotherms as obtained by the numerical analysis. The fusion zone represents the boundary, inside which the steel temperature exceeds the melting temperature. This temperature depends on the steel alloy and for mild carbon steel it can be estimated around 1400^oC. Similarly, the temperature above which the microstructure of steel is altered due to the heat input is estimated around 700^oC. This temperature represents the heat affected zone boundary, which separates the affected and unaffected base material. As seen in Figure 4.21, the fusion zone is slightly underestimated in the numerical model. This can be explained by the definition of the heat source model's depth as the weld throat, instead of the penetration depth. In general, however, the isothermal contours show a good agreement with the specimen's microstructure.

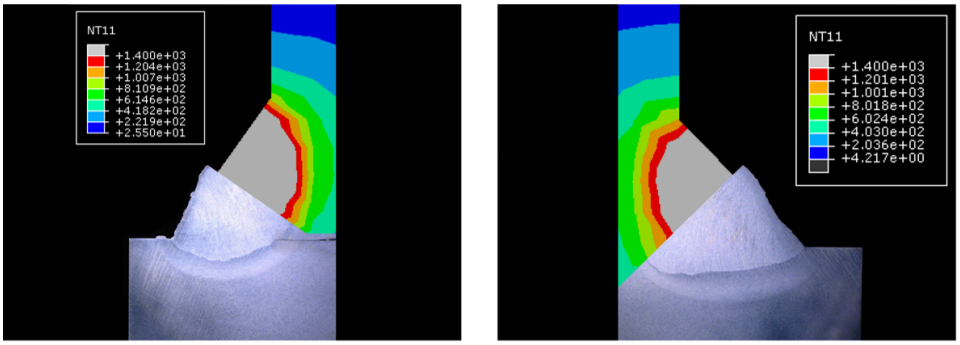

Figure 4.21: Comparison of fusion zone and heat affected zone between experiment and simulation

4.7.2. Mechanical analysis

The distortion results of the numerical analysis were derived by evaluating the horizontal displacement of the vertical plate, at the points of interest, at the same time moments as in the experiment. As was presented in Chapter 3, Figure 3.5b, the specimen was placed in such a way that the transverse edge of the bottom plate was in contact with the table. Considering that the distortion of the bottom plate could affect the actual distortion measurements of the thinner plate, the horizontal distortion of this supporting face was also taken into account. However, numerical analysis suggested that it was of the order of $10^{-3}mm$, which is insignificant compared to the distortion at the points of interest, on the thinner plate. The comparison between experimental and simulation data are shown in Figure 4.23.

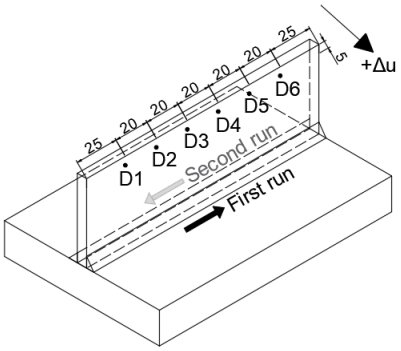

Figure 4.22: Sign convention for distortions

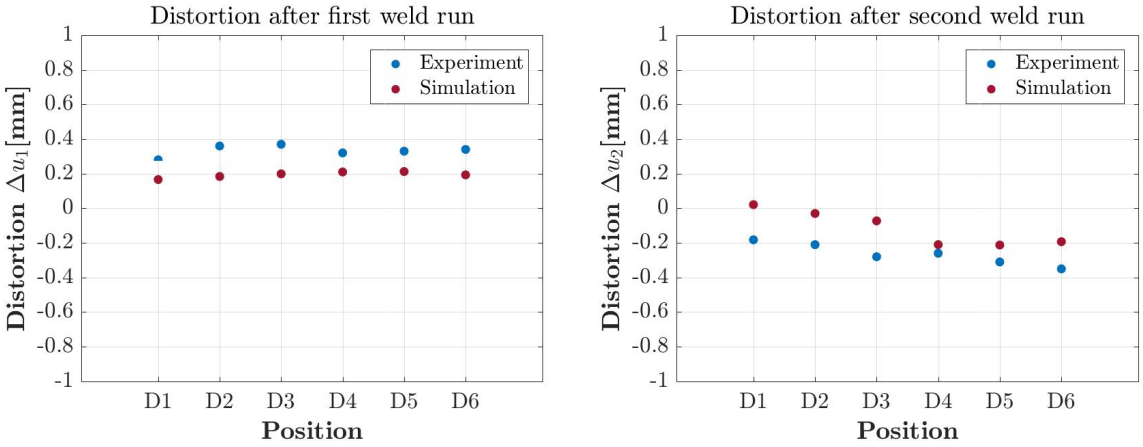

Figure 4.23: Comparison of experimental and numerical distortion results

Comparing the results of Figure 4.23, some useful conclusions can be drawn. Predicted distortions follow a similar pattern as the one observed during the experiment. Although a small deviation is observed between predicted and measured values, overall a good agreement between simulation and experiment is achieved. The reason behind the differentiations could lie in the fact that, as shown in Figures 4.21, the molten zone is slightly underestimated. To support this claim, a new thermomechanical analysis has been conducted, where the depth parameter of the heat source model is considered equal to the penetration depth of the weld, as shown in Figure 4.24. Indeed, in the new model, the predicted distortion approaches more the actual measured data during the experiment. However, in this research project, the depth parameter is considered equal to the weld's throat. This is partly due to the fact that the analyses have indicated that it yields satisfactory results and partly because the penetration depth is not known, unless a microscopic image of the weld is available. Overall, results of the thermal and mechanical numerical analyses are confirmed by measured data of the small-scale welding experiment. The suggested methodology can be applied in other welded connections with satisfactory accuracy.

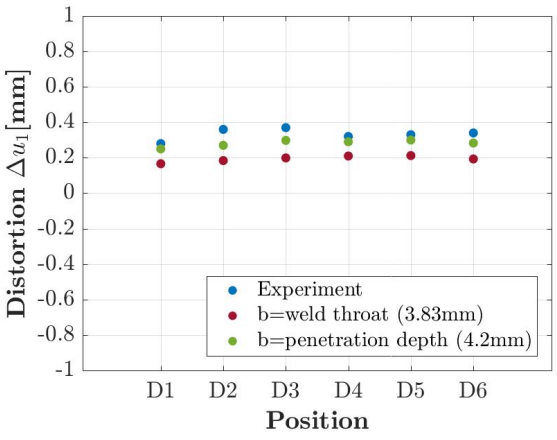

Figure 4.24: Comparison of distortion results for different depth parameters

5

Simulation of orthotropic steel deck joint

This chapter describes the procedure followed in the numerical modelling of an orthotropic steel deck's connection. The adopted thermomechanical model is based on the work described in Chapter 4. The influence of welding sequence, boundary conditions and material model on the residual stress distribution is also discussed.

5.1. Introduction

Fatigue tests on a full-scale orthotropic steel deck were carried out in the Stevin II laboratory of TU Delft, for the determination of the classification of orthotropic bridge deck details for new designed steel bridge decks (Figure 5.1). The dimensions of this orthotropic steel deck were adopted in the present study, in order to investigate the residual stress distribution in the welded through-to-deck joint.

Figure 5.1: Overview of the OSD in the laboratory [11]

The deck plate has a total length of 9.4m and width of 5.1m. The thickness of the deck plate is 20mm and longitudinal stiffeners of a closed, trapezointal cross section are welded at the bottom of the deck plate (Figure 5.2). The troughs have a thickness of 6mm and a height of 350mm, while the width is 300mm at the upper side and 105mm at the lower side (Figure 5.4). The material used to manufacture the specimen is structural steel S355J2, under the requirements of EN10025-2:2004 and EN10029:2010.

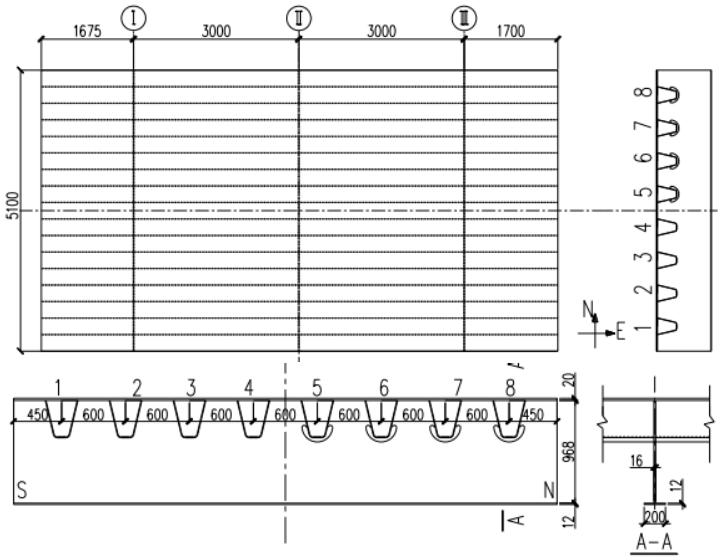

Figure 5.2: Deck dimensions [mm] [37]

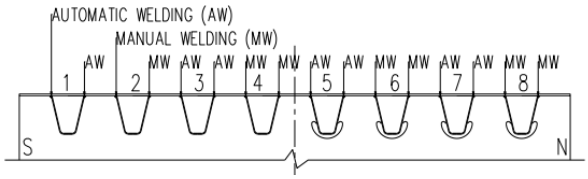

Figure 5.3: Weld sequence [37]

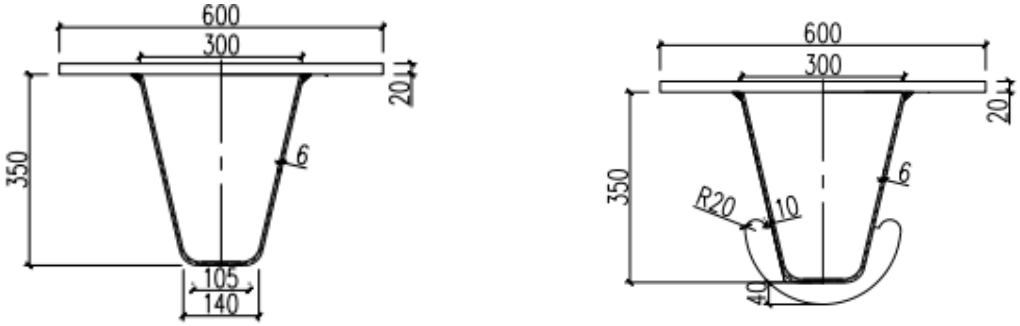

Figure 5.4: Geometry of longitudinal stiffeners [37]

5.2. Numerical modelling

In an orthotropic steel deck, the trough-to-deck plate connection is a region where crack initiation and propagation is likely to occur. Therefore, obtaining more information about the residual stress distribution near the weld is useful in order to understand the reasons behind this phenomenon.

As part of the large scale experiment in an orthotropic bridge deck, executed in Delft University of Technology, welding between the trough and the deck plate was executed both in an automatic and manual way (Figure 5.3). In the present study, the welded connection between longitudinal stiffeners and the deck plate of an orthotropic steel deck is modelled in the finite element software ABAQUS. The first step of the numerical approach is the thermal analysis and the investigation of temperature distribution during welding. The welding heat source is modelled using the double ellipsoid heat source model and appropriate thermal properties and boundary conditions are applied. In the next step of the process, the nodal temperatures, as obtained by the thermal analysis, are used as input information for the mechanical analysis. Similarly, mechanical material properties and boundary conditions have to be defined. Finally, both longitudinal and transverse residual stress distribution in the through-to-deck plate connection are evaluated.

Welding of the longitudinal stiffeners to the deck plate has been executed both in a manual and automatic way. This applies only to the outside of the stiffeners, since the welding source cannot have access to the inside of the trough. For the case of manual welding, special attention in brought upon the influence of the welding sequence on the residual stress distributions. Thus, two welding scenarios are investigated:

- Parallel welding
  In this case, welding is executed at the same time on both trough sides. After both sides of the trough are welded to the deck plate, a sufficiently large time step is considered, so as to simulate the process of material cooling. Thus, the model returns to room temperature and the stress distribution at the end of the analysis represents the residual stresses in the material.

- Sequential welding
  In contract to the previous case, welding is executed on one side, only after the completion of the previous one is complete. Again, a large time step is considered after the welding procedure, in order to obtain the residual stresses at the end of the material cooling.

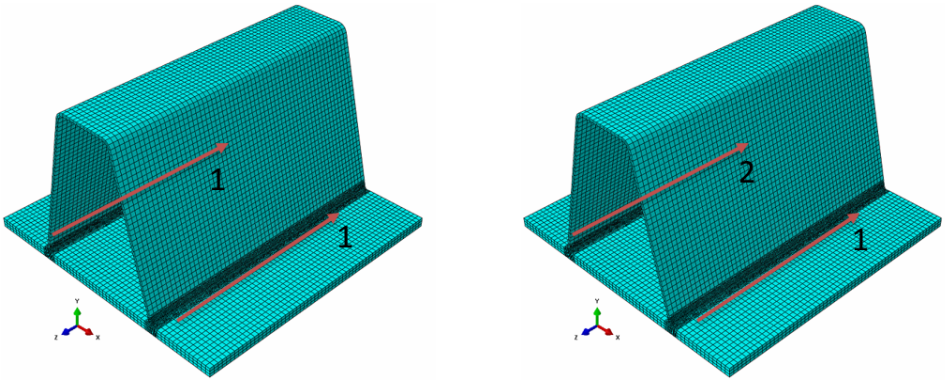

Figure 5.5: Welding direction of parallel and sequential welding

5.2.1. Geometry

As shown in Figure 5.3, the welded connection between the longitudinal stiffeners and the deck plate has been executed in two ways; manual and automatic. Between the two methods, differences are observed, not only in the followed welding procedures and the weld geometry, but also in the geometry of the connection. As a result, two separate models are constructed, as shown in Figures 5.6, 5.7. Each model consists of one trough, connected to the deck plate. For ease of calculations and limit of the computational time, the model length is considered equal to its width ($z = 600mm$).

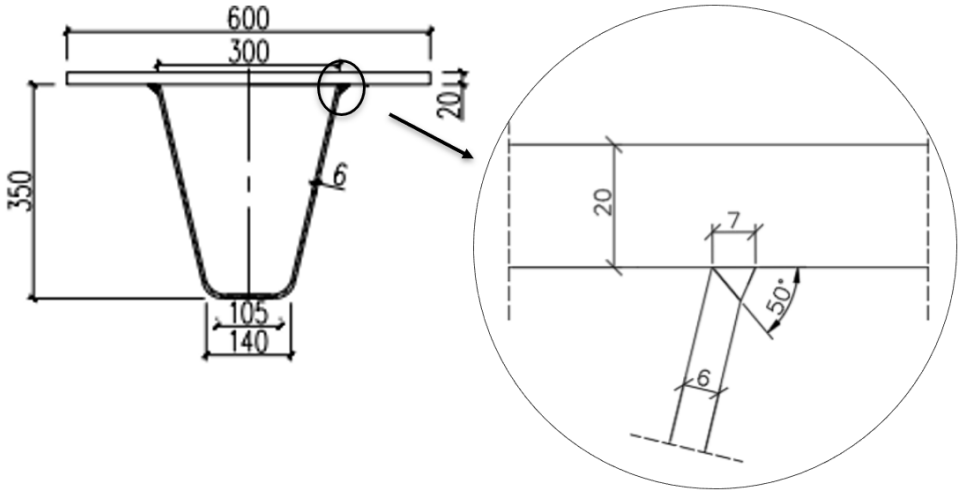

Figure 5.6: Trough to deck connection geometry and weld size for manually welded connection

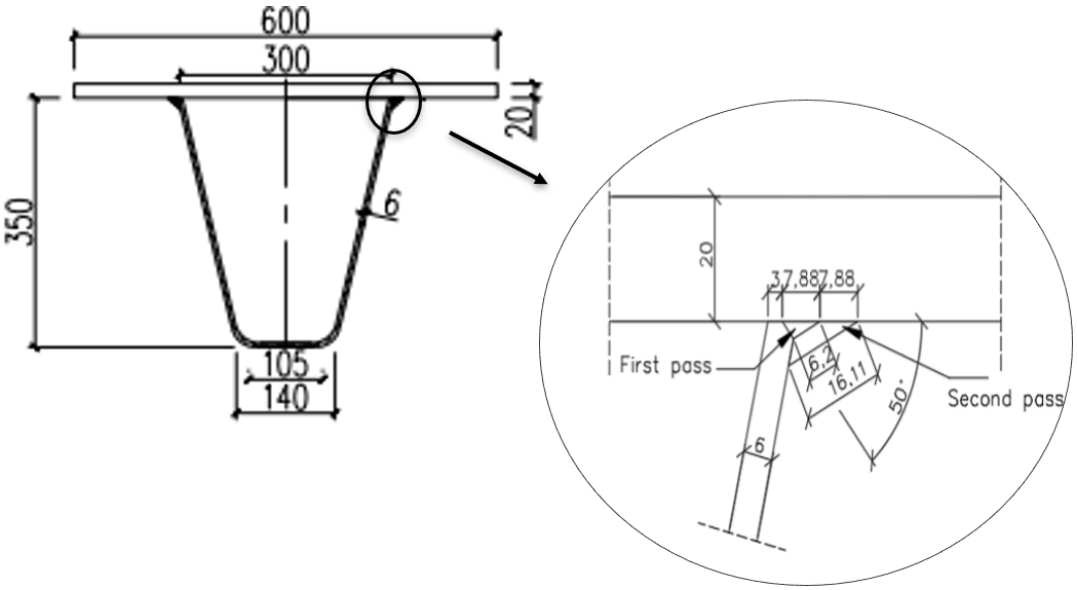

Figure 5.7: Trough to deck connection geometry and weld size for automatically welded connection

5.2.2. Mesh

The used mesh is shown in Figures 5.8, 5.9. Near the weld area, the element size is kept as small as possible, in order to accurately capture the thermal response due to the heat input. However, since welding simulations require a large amount of computational time, the element size is kept at 2.5mm at the longitudinal direction, near the weld. This size gradually increases to 10mm at a distance from the weld, in order to reduce the total amount of elements. In the transverse direction, two elements are adopted in the stiffener's depth and seven elements in the deck's depth. In the fillet welds, wedge elements are used, in order to account for their triangular shape, while in the rest of the model, the element shape is kept hexagonal. During the thermal analysis, 6-node linear heat transfer triangular prisms (DC3D6) are used at the welds, and 8-node linear heat transfer bricks (DC3D8) at the rest of the model. Accordingly, in the mechanical analysis, 6-node linear triangular 3D stress prisms (C3D6), and 8-node linear 3D stress bricks (C3D8R) are used for the welds and the rest of the model respectively.

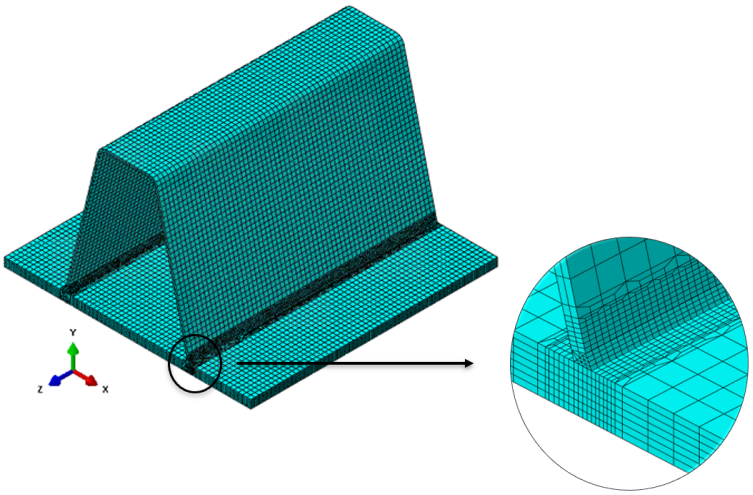

Figure 5.8: Numerical model and adopted mesh for manually welded connection

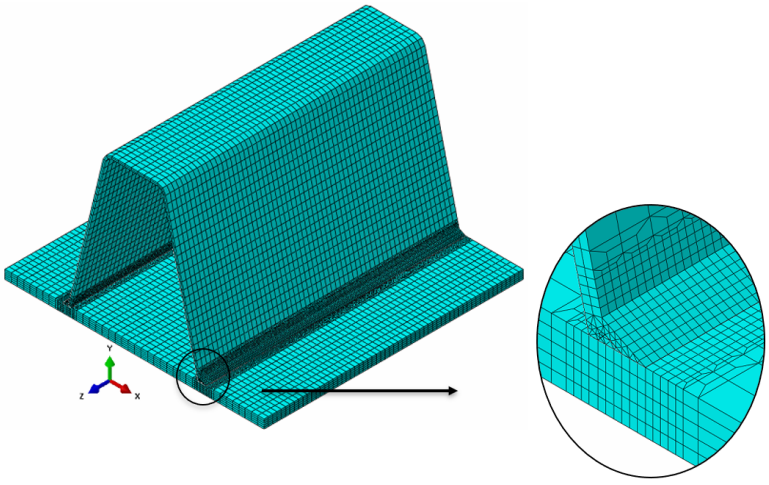

Figure 5.9: Numerical model and adopted mesh for automatically welded connection

5.2.3. Material

As described in Chapter 4, it is necessary to model the material behaviour using temperature dependent thermomechanical properties. In EN 1993-1-2:2005 [1], information is given about the evolution of those properties with increasing temperature. In this standard, it is assumed that steel experiences no strain hardening under elevated temperatures, thus it adopts an ideal plastic material model (Figure 5.10). This assumption has also been widely used in the literature, in order to capture the mechanical response of steel during welding. In Chapter 4, this material law was used in order to validate the accuracy of the adopted thermal model and it was found to yield satisfactory results. In this Chapter, a further examination is carried out, in order to study the effect of strain hardening on the residual stresses. For this reason, apart from the ideal elastoplastic material model, a stress-strain relationship including strain hardening (Figure 5.11), is also used as input information. This relationship was the result of steady-state heating tests on standard S355 specimens. During the experiment, first the specimens were heated up to certain temperature level, and then they were loaded with a train increase of $0.02\%/sec$, [5]. As it can be seen from Figure 5.11, strain hardening is observed up until the temperature of 400^oC, while for higher temperatures, no strain hardening is noticeable.

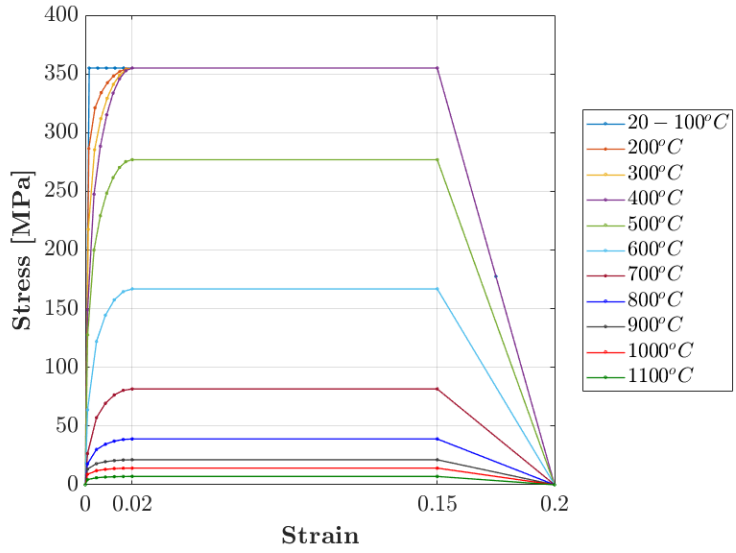

Figure 5.10: Stress-strain relationship of S355 under elevated temperautes, without considering strain hardening [1]

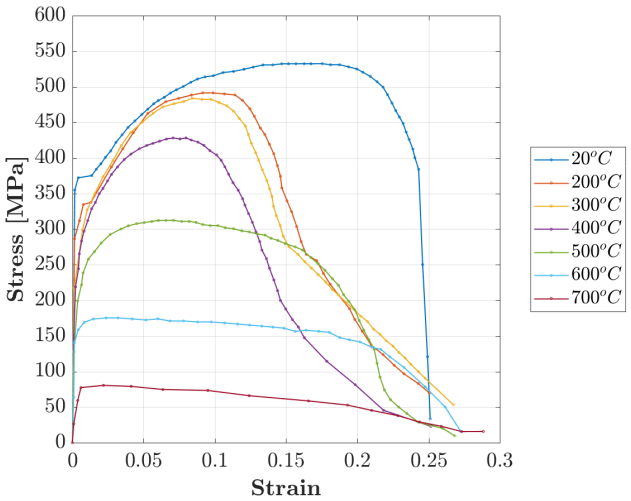

Figure 5.11: Stress strain relationship of S355 under elevated temperatures considering strain hardening, adopted from [5]

5.2.4. Thermal analysis

The first step of the numerical analysis is the thermal analysis for the calculation of the temperature distribution during and after welding. The followed procedure is in accordance with the information presented in Chapter 4.

The continuous deposition of the filler material during welding is implemented through the birth and death tecnique. The weld bead is divided into segments and in the beginning of the analysis, all segments are removed from the model. In every analysis step, a segment is added, following the movement of the heat source along the plates. The duration of every step is defined by the welding speed and the length of the applied segment. After the completion of the welding procedure, one analysis step with a sufficiently large duration ($\Delta T = 7500s$) is applied, in order for the material's temperature to return to its initial value (25^oC).

As it has been mentioned, welding has been executed both in a manual and automatic way. In the first case, the followed method has been Shielded Metal Arc Welding (SMAW), and welding has been completed with one pass on each side of the trough. In the second case, two passes have been executed on each side of the trough. The first one was completed though a Flux Cored Arc Welding (FCAW) technique, while the second one was executed with a Submerged Arc Welding (SAW) technique. The characteristics of each method are summed up in Table 5.1.

The heat source is modelled according to the double ellipsoid heat source model [16]. The heat input is defined as a body heat flux, which is applied on the entire model but is running along the welding direction. This is achieved by implementing in the model the DFLUX subroutine, in which the heat source model is fully described. The geometrical parameters a, b, c_f and c_r, which are necessary for the description of the ellipsoidal shape of the heat source, are related to the weld's geometry as indicated in Chapter 4. More specifically, a is considered equal to half the weld's width, while b is taken equal to the theoretical weld throat. The length parameters c_f is equal to parameter a and $c_r = 2.33 \times c_f$. The origin of the local coordinate system of the heat source is applied in the middle of the fillet weld's hypotenuse, while appropriate rotation transformations are applied, so as to allow for the x and y axes to be parallel and vertical to it.

Heat losses through convection and radiation are also considered, by assigning appropriate heat transfer and emissivity coefficients. In this case, the assigned values to the coefficients are similar to the ones assumed in Chapter 4, since no additional data were available. The necessary parameters for the thermal analysis are shown in Table 5.1.

	Manual Welding	Automatic Welding	
Steel grade	S355	S355	S355
Layers	1	1	2
Method	SMAW	FCAW	SAW
Current [A]	165	235	525
Voltage [V]	23.5	26	26
Welding speed [mm/s]	1.5	7.5	7.9
Efficiency	0.80	0.80	0.95
Width a [mm]	2.98	3.1	8.06
Depth b [mm]	6.40	3.53	3.4
Front c_f [mm]	2.98	3.1	8.06
Back c_r [mm]	6.94	7.2	18.8
Heat transfer coefficient h_c $[W/(m^2K)]$	10	10	10
Emissivity coefficient ϵ	0.5	0.5	0.5

Table 5.1: Welding characteristics and heat source parameters for manual and automatic welding, used in the thermal analysis

5.2.5. Mechanical analysis

The next step towards the estimation of welding residual stresses is the mechanical analysis. The temperature distributions calculated during the previous step, are inserted into the mechanical analysis as a predefined temperature field.

In order to achieve compatibility between the thermal and mechanical analysis, the same number of time steps, with the same duration, is used. The welding procedure is implemented again through the birth and death technique, thus simulating the constantly changing constraint conditions due to the solidification of the filler material.

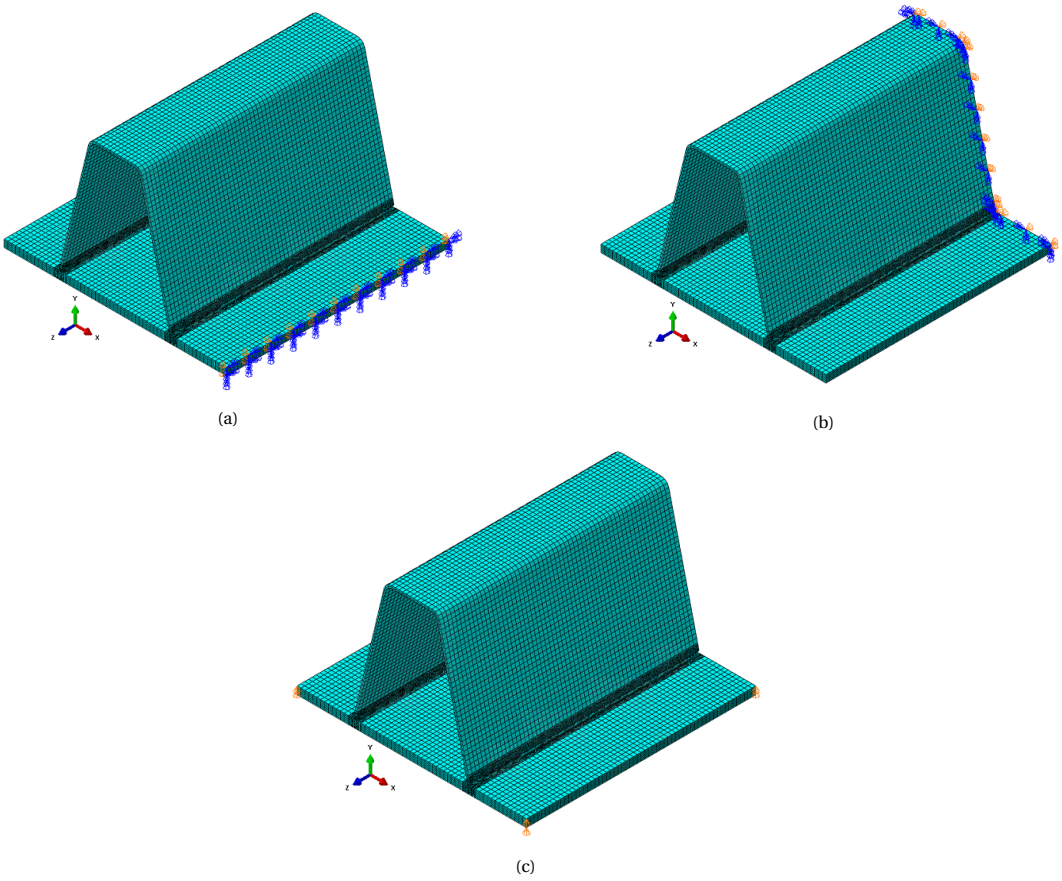

Figure 5.12: Boundary conditions implemented in the numerical model

When investigating welding residual stresses, boundary conditions highly affect the residual stress field. Indeed, overconstraining the mechanical model can introduce additional stresses, thus overestimating the actual condition. It is therefore important to implement appropriate boundary conditions, which can yield realistic results. In this study, it has been considered that the part under investigation is not independent, but it is affected by the surrounding structure. Thus, along two faces vertical to the x and z horizontal directions, symmetry boundary conditions have been applied. As shown in Figure 5.12a, the noted face was constrained against translations along the x direction and rotations around the y and z axes, thus taking into account the restricted movement of this part due to adjacent trough. Similarly, as shown in Figure 5.12b, translations along the z axes and rotations around the x and y axes were restrained on the highlighted face, so as to consider the symmetry of the model in the longitudinal direction. Finally, in order to avoid rigid body motion, the model has also been constrained against vertical displacement (along the y axis), on the four external vertical edges of the deck plate (Figure 5.12c). Symmetry boundary conditions have not been considered on all surrounding faces, so as to avoid overconstraining the model.

5.3. Simulation results for manual welding

5.3.1. Influence of welding sequence

Longitudinal stresses at the deck

The longitudinal stresses (σ_z) are calculated along an edge near the free face ($z = 20mm$), along the middle edge $z = 300mm$, and along an edge near the face that is constrained against moving in the longitudinal direction ($z = 580mm$), as shown in Figure 5.13. That way, the influence of the boundary conditions can also be estimated. Out of the three considered cases, the one that may more realistically represent the actual boundary conditions in an orthotropic steel deck is the position $z = 580mm$. When considering a large-scale model of an OSD and evaluating the residual stress field in the midspan between two cross-beams, the boundary conditions near this face can be considered representative of the constraints imposed by the surrounding material in the longitudinal direction. Thus, in the next sections, residual stresses are plotted for this specific position.

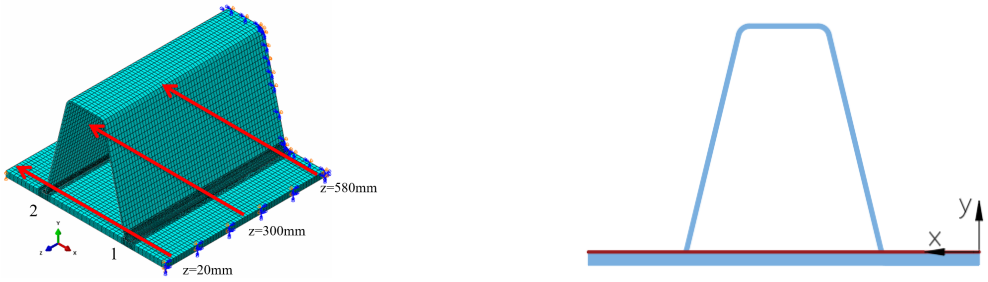

Figure 5.13: Indication of position for which longitudinal stresses on the deck are plotted

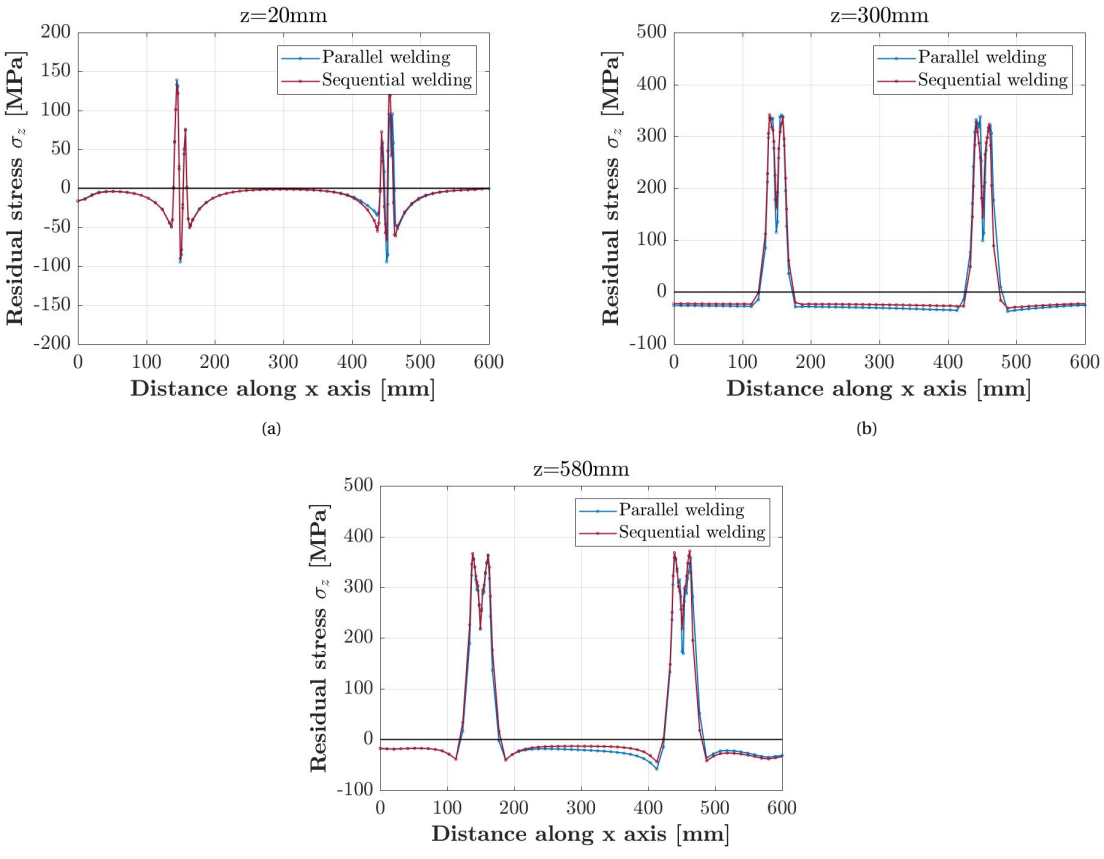

Figure 5.14: Longitudinal residual stresses σ_z along three edges of the deck plate

Longitudinal stresses at the stiffeners

The longitudinal stresses (σ_z) are calculated along the plane $z = 580mm$, as shown in Figure 5.15. Stresses are investigated along four positions, namely the inside and outside edges of both stiffeners.

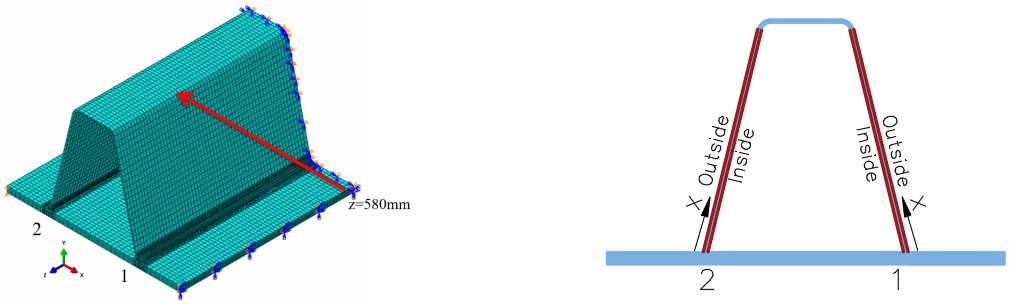

Figure 5.15: Indication of position for which longitudinal stresses on the stiffeners are plotted

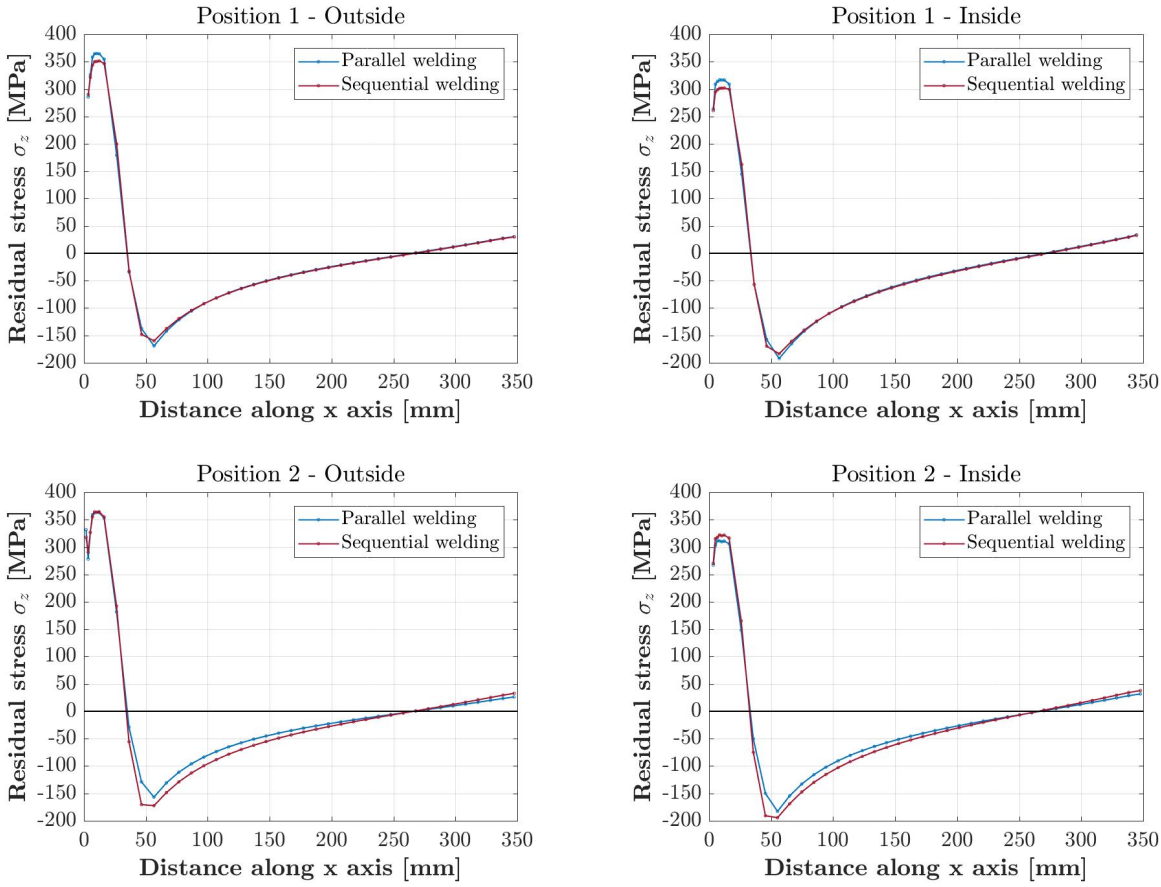

Figure 5.16: Influence of welding sequence on longitudinal residual stresses along the stiffener

Transverse stresses at the deck

The transverse stresses (σ_x) are calculated along the thickness of the deck, in the end of the plate ($z = 580mm$), as shown in Figure 5.17. The starting points of the edges along which stresses are plotted are located at the weld's root and toe, in both stiffeners. In case of sequential welding, position 1 refers to the side of the trough that is welded first.

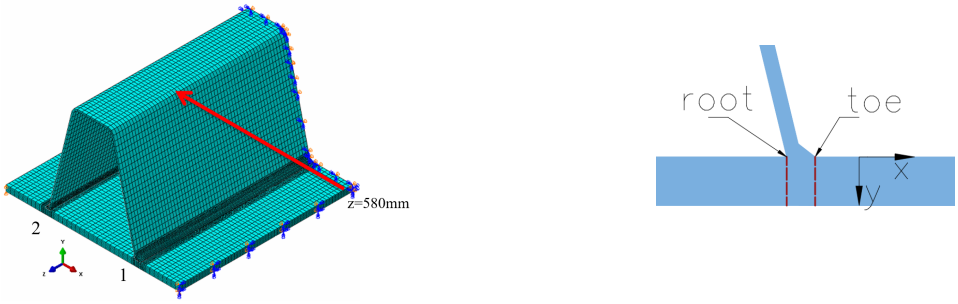

Figure 5.17: Indication of position for which transverse stresses on the deck are plotted

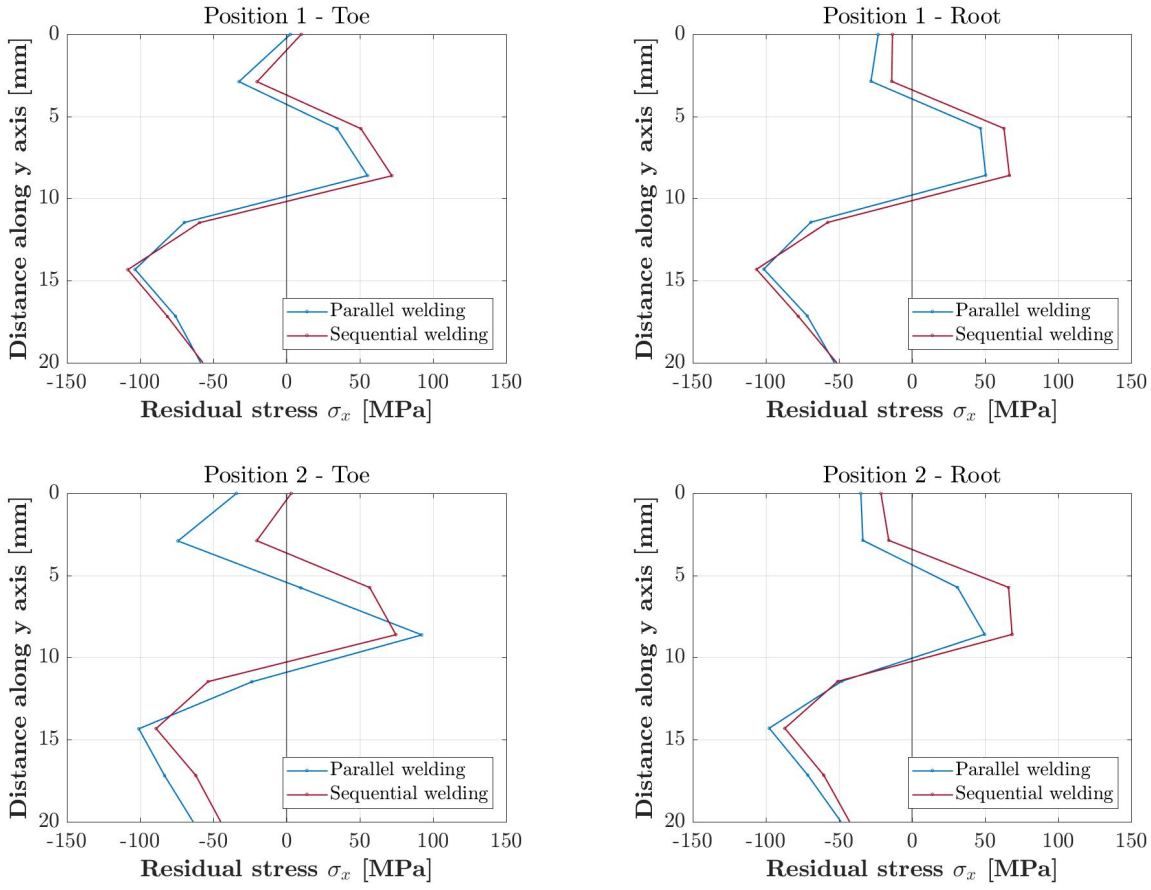

Figure 5.18: Influence of welding sequence on transverse residual stresses along the deck's thickness

5.3.2. Influence of material

The influence of the adopted material model on the residual stresses is investigated for the case of parallel welding. The only difference between the two analyses is the stress-strain relationship, so as to evaluate the effect of strain hardening on the material's response.

Longitudinal stresses at the deck

Longitudinal stresses, (σ_z), at the deck are calculated along three edges on the deck's surface, as shown in Figure 5.19.

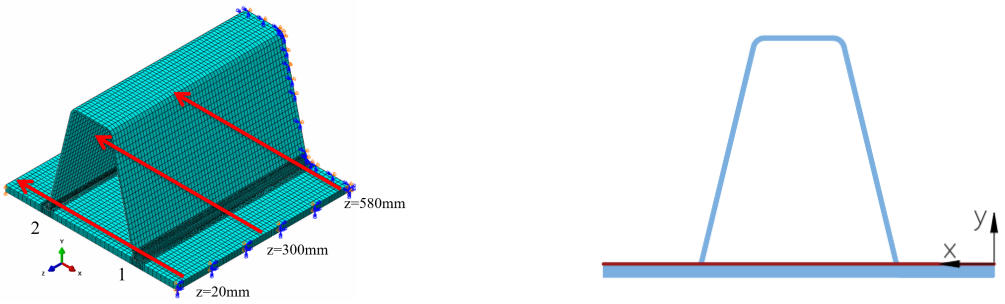

Figure 5.19: Indication of position for which longitudinal stresses on the deck are plotted

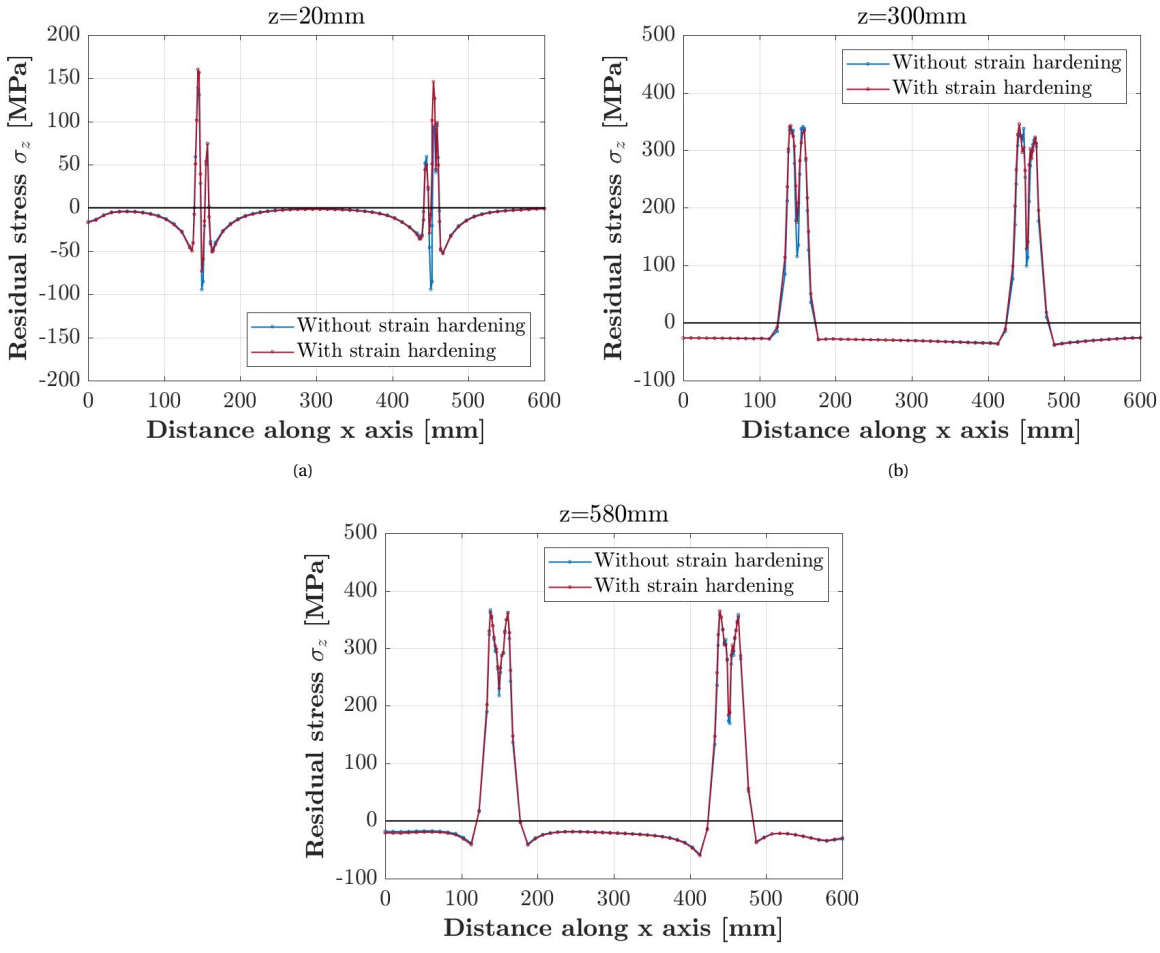

Figure 5.20: Longitudinal residual stresses σ_z along three edges of the deck plate

Longitudinal stresses at the stiffener

Longitudinal residual stresses (σ_z) are calculated along the height of the stiffeners, in the end of the model (z=580mm). Four locations are considered, as shown in Figure 5.21.

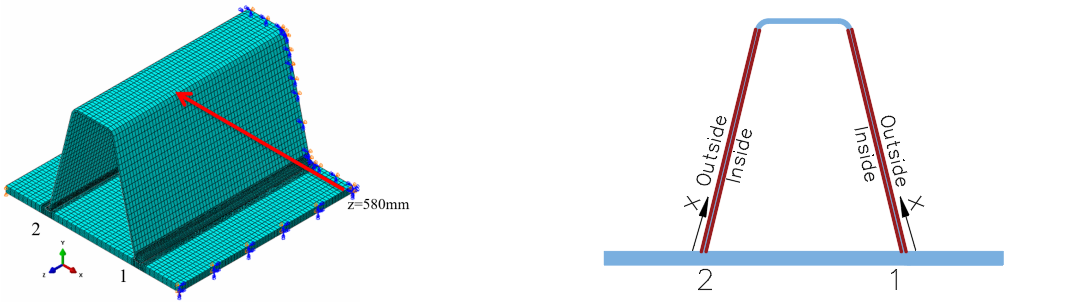

Figure 5.21: Indication of position for which longitudinal stresses on the stiffeners are plotted

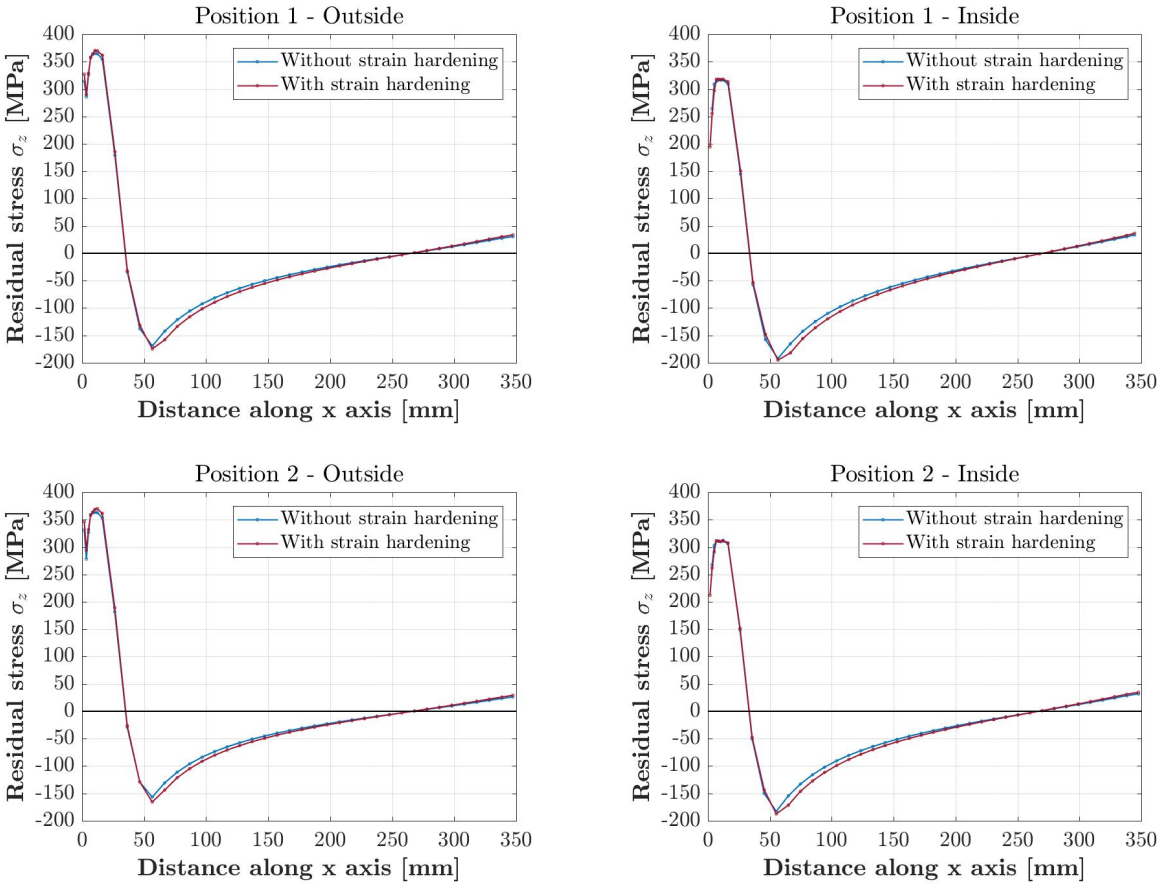

Figure 5.22: Influence of material model on longitudinal residual stresses along the stiffener

Transverse stresses at the deck

Transverse stresses (σ_x) are calculated along the deck's thickness, in four positions, namely the weld's toe and root at both stiffeners. The lines along which transverse stresses are estimated lie in the plane z=580mm.

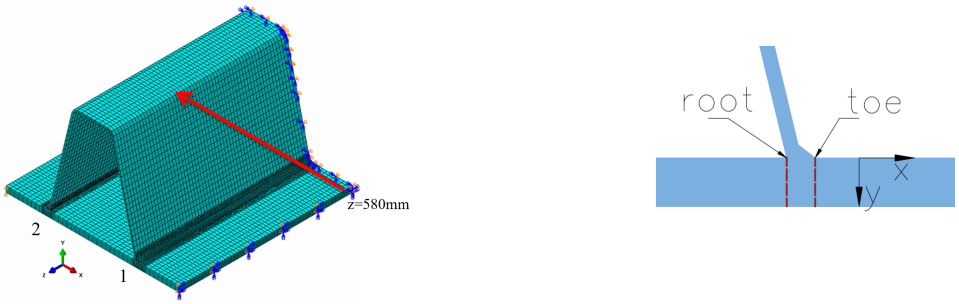

Figure 5.23: Indication of position for which transverse stresses on the deck are plotted

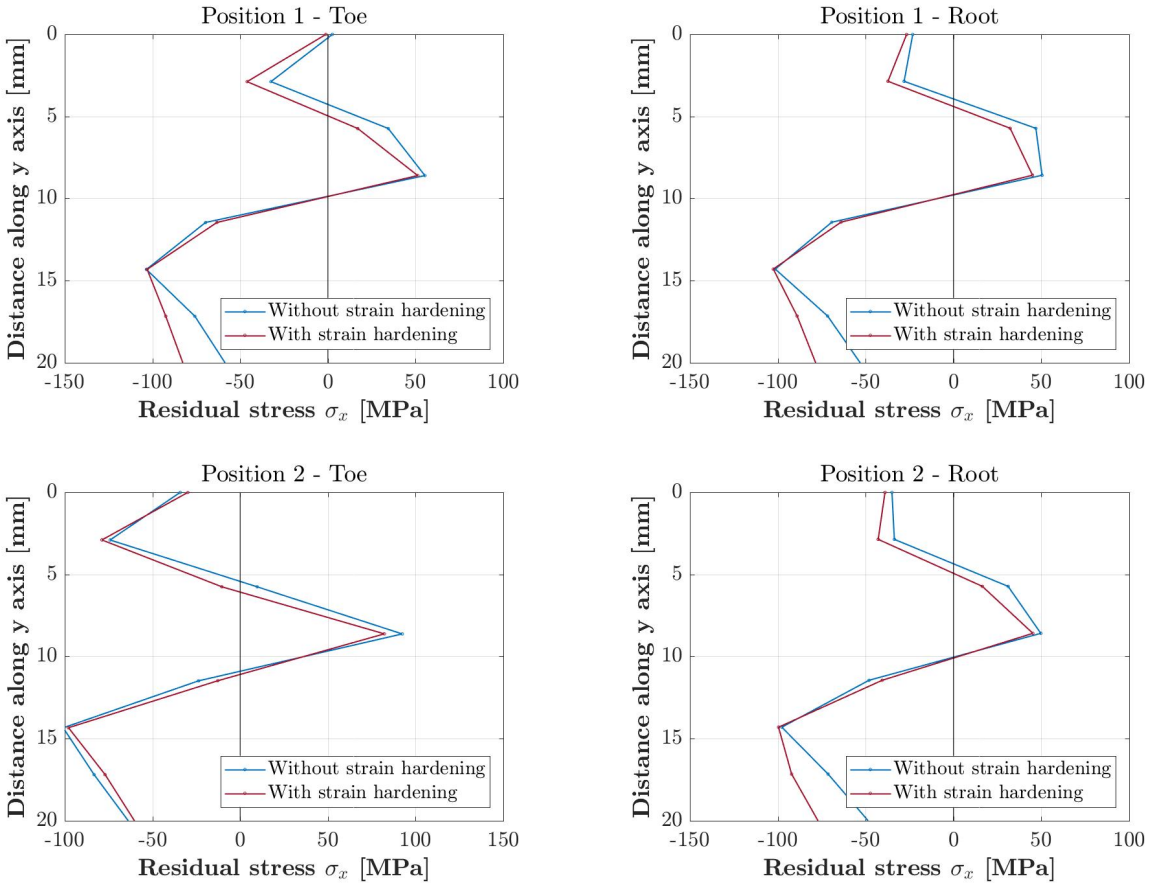

Figure 5.24: Influence of material model on transverse residual stresses along the deck's thickness

Stress contour plots

In the following Figures, the contour plots of principal stresses are plotted for three different scenarios.

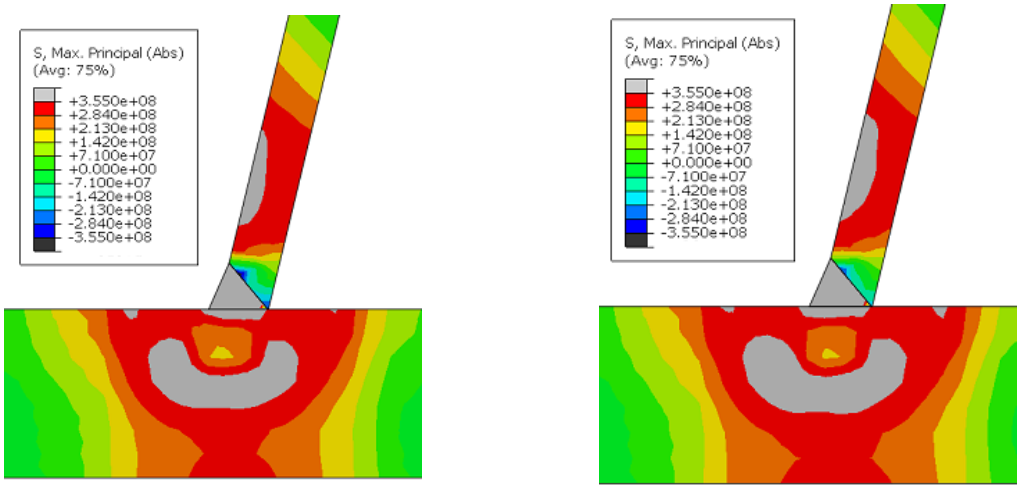

Figure 5.25: Maximum principal stresses in the welded joint, in case of parallel welding, when strain hardening is not included in the material model (a), and when it is included (b)

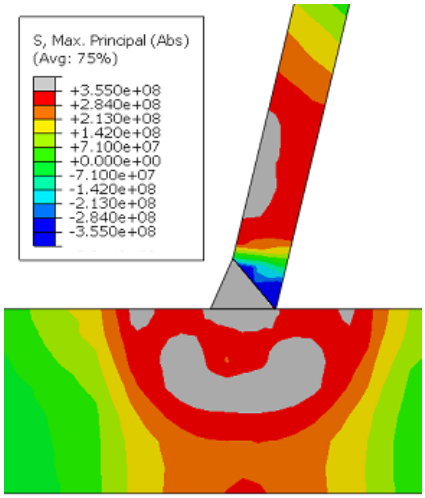

Figure 5.26: Maximum principal stresses in the welded joint in case of sequential welding. The material model does not include strain hardening

When evaluating the possible positions for fatigue crack initiation, it is important to take into account the combination of residual stresses and stresses due to external loading. Even when the externally applied stresses are mainly compressive, or their magnitude in tension is not significant to induce crack propagation, the structure is susceptible to fatigue failure due to the residual stress field. Since residual and external stresses are superimposed, the actual range of fluctuating stresses would be in tension in cases of very high principal tensile residual stresses. This is also the case for the contour plots of Figures 5.25, 5.26. Indeed, high principal stresses are present around the weld. Locally, these stresses exceed the material yield stress (355MPa). As a result, the areas near the weld's toe and root are potential crack initiation positions.

5.3.3. Welding imperfections

For the strength calculation of stiffened plates, residual stresses are regarded as initial imperfections. Indeed, in case of plated structures, EN 1993-1-5 [2] translates geometric and structural imperfections into equivalent initial imperfections, that are taken into account in numerical non-linear analyses. In reality, their actual magnitude is not known a priori and the extent to which the suggested values of EN 1993-1-5 can accurately describe the residual stresses and deformations caused during welding, remains vague [31].

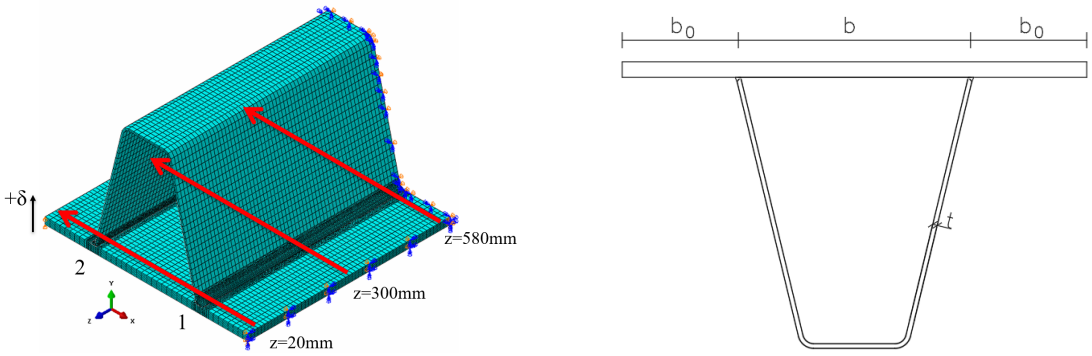

Figure 5.27: Edges along which deflection is plotted and sign convention

The estimation of imperfections induced by welding has been performed through the evaluation of the vertical displacement of the deck plate, after the material has cooled down. For this purpose, the boundary conditions of the model have been slightly modified, so as to consider the deflection of the deck plate inside the trough. Thus, the vertical displacement has been constrained along the longitudinal, z-direction of the plate, in the position of the stiffeners (Positions 1, 2 in Figure 5.27a). The vertical displacement is compared to the value $b/200$, suggested by [2] for local imperfections of panels with a short span b.

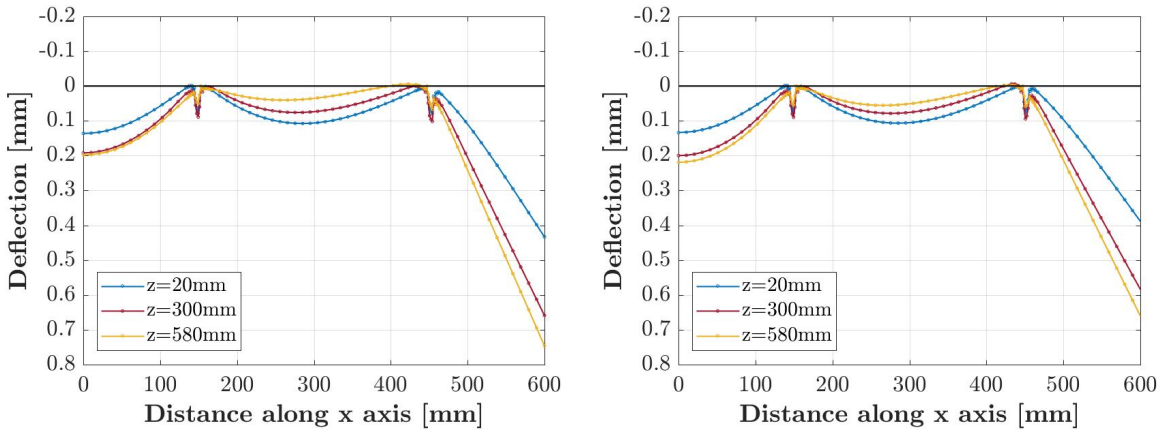

Figure 5.28: Deflection of the deck plate in case of (a) parallel welding and (b) sequential welding

In Figure 5.28, the deflection of the deck plate, after the cooling down period, is plotted for both cases of parallel and sequential welding. Results are shown for three edges along the deck, as indicated in Figure 5.27. At the position z=20mm near the free face, the deflection of the deck between the stiffener positions is estimated at $b/3000$ and $b_0/1100$ outside the trough, at point x=0. Near the restrained face (z=580mm) a vertical deflection of $b/6000$ is found inside the trough and $b_0/750$ out of it. Even in the most unfavourable case of $b/3000$, the deflection is significantly lower than the limit value $b/200$ suggested in EN 1993-1-5 [2]. This, however, includes the combined action of both fabrication and manufacturing imperfections.

5.4. Simulation results for automatic welding

5.4.1. Residual stresses

The following analysis results refer to the case of parallel welding. The adopted material model is the one described in EN 1993-1-2:2005 [1], which does not consider strain hardening under elevated temperatures.

Longitudinal stresses at the deck

Longitudinal stresses, (σ_z), at the deck are calculated along three edges on the deck's surface, as shown in Figure 5.29.

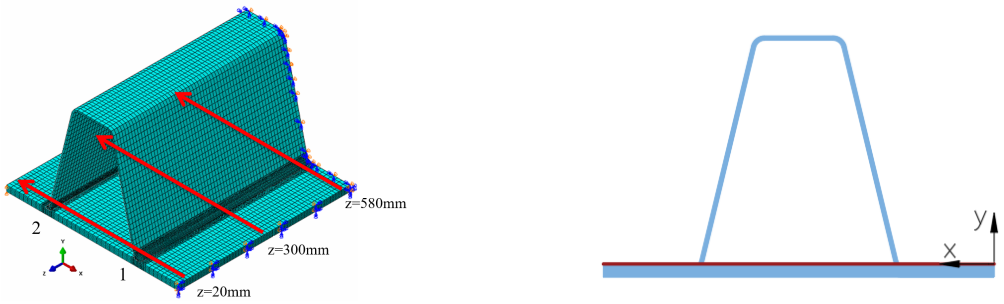

Figure 5.29: Indication of position for which longitudinal stresses on the deck are plotted

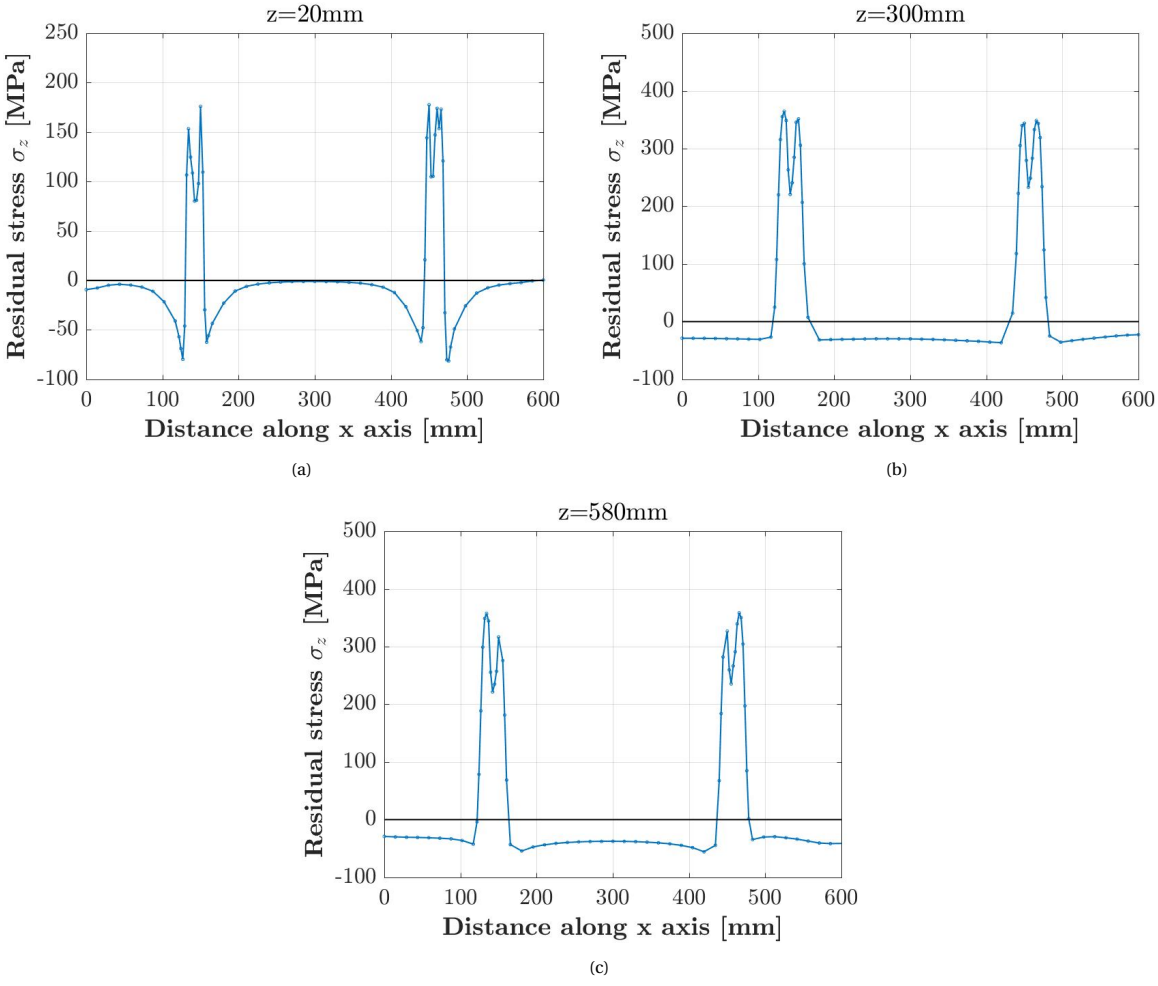

Figure 5.30: Longitudinal residual stresses σ_z along three edges of the deck plate

Longitudinal stresses at the stiffener

Longitudinal residual stresses (σ_z) are calculated along the height of the stiffeners, in the end of the model (z=580mm). Four locations are considered, as shown in Figure 5.31.

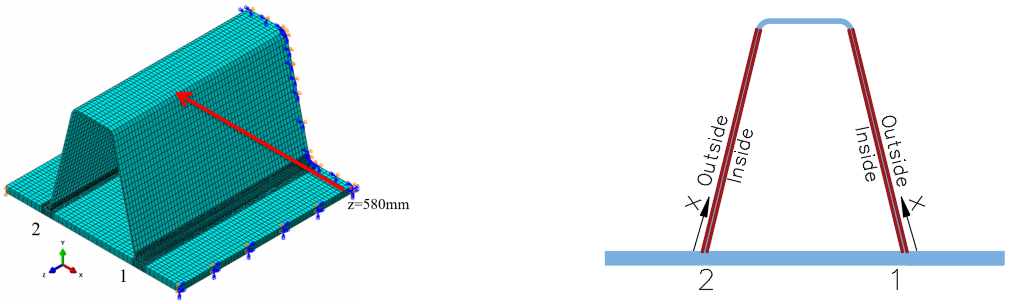

Figure 5.31: Indication of position for which longitudinal stresses on the stiffeners are plotted

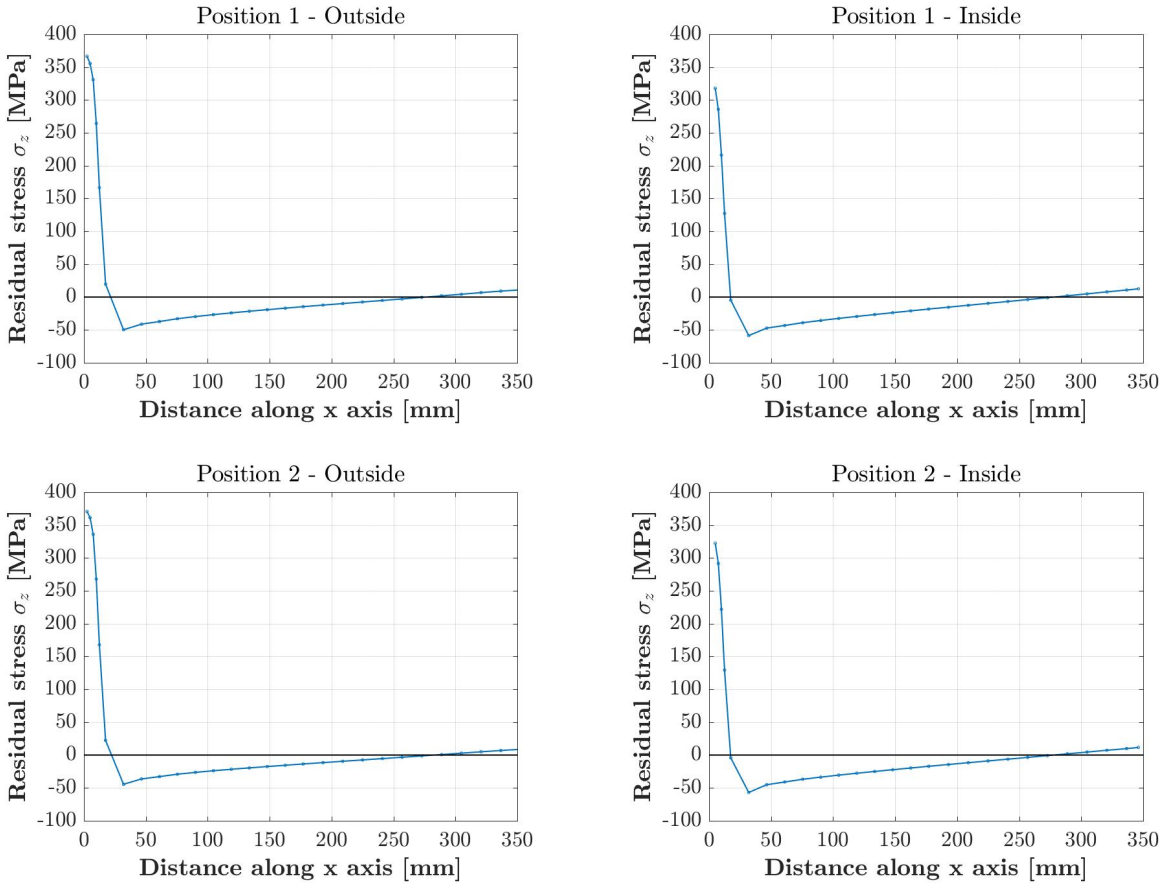

Figure 5.32: Influence of material model on longitudinal residual stresses along the stiffener

Transverse stresses at the deck

Transverse stresses (σ_x) are calculated along the deck's thickness, in four positions, namely the weld's toe and root at both stiffeners. The lines along which transverse stresses are estimated lie in the plane z = 580mm.

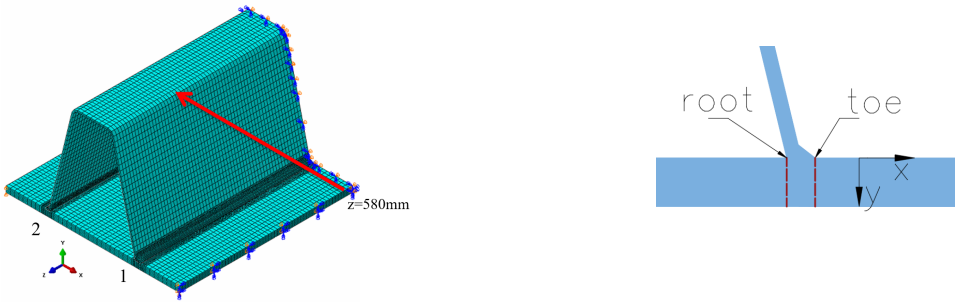

Figure 5.33: Indication of position for which transverse stresses on the deck are plotted

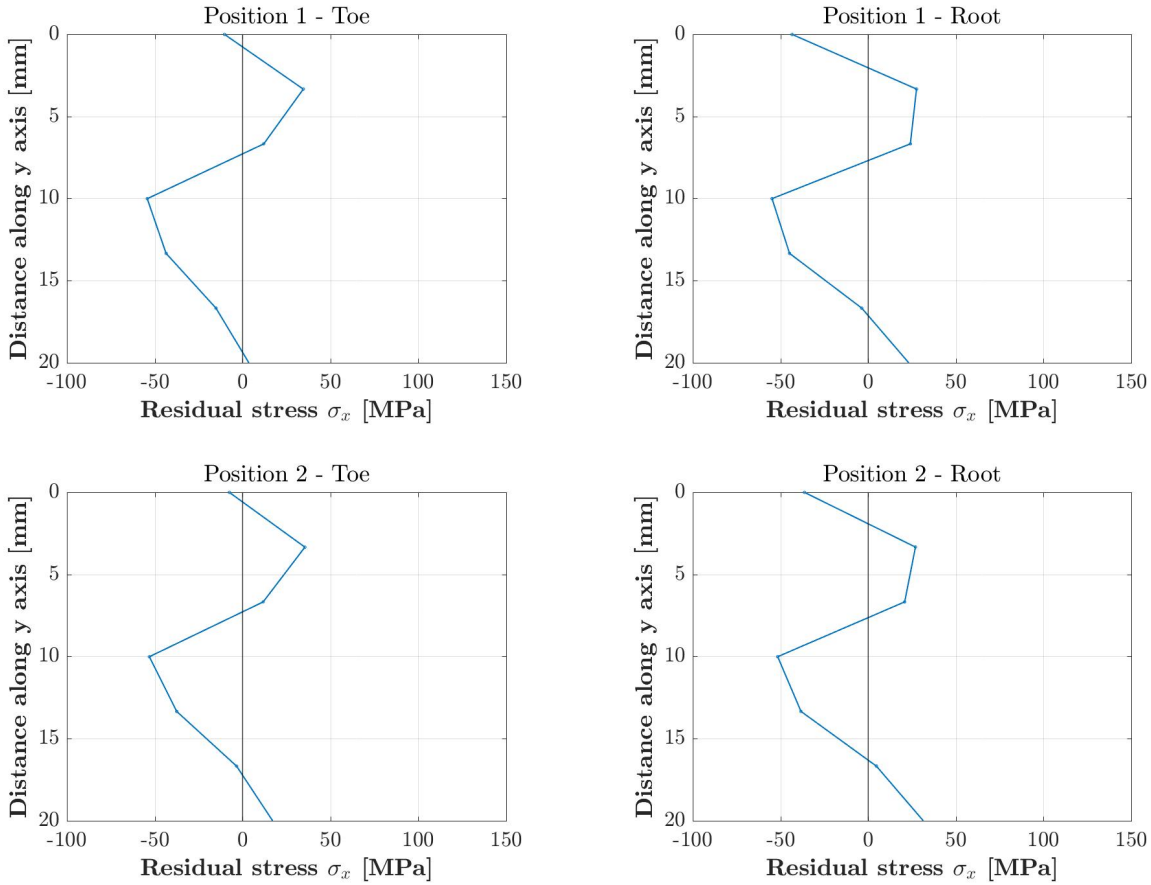

Figure 5.34: Influence of material model on transverse residual stresses along the deck's thickness

Stress contour plots

As in the case of the previous model, significantly high principal tensile stresses appear around the weld. These stresses exceed the material yield stress close to the weld's root and toes. Due to the superposition of external and residual stresses, this highly tensile residual stress field indicates the susceptibility of this connection to fatigue cracking, even if the component is nominally in compression.

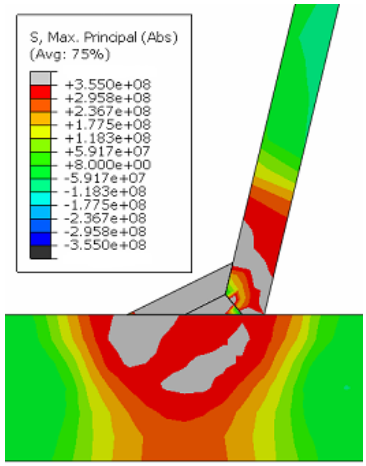

Figure 5.35: Maximum principal stresses in the welded joint, in case of parallel welding

5.4.2. Welding imperfections

Imperfections induced by welding are evaluated through the vertical deflection of the deck plate at three locations, as shown in Figure 5.36a. Again, the vertical displacement has been restrained along the longitudinal z-direction, at the stiffener positions 1, 2.

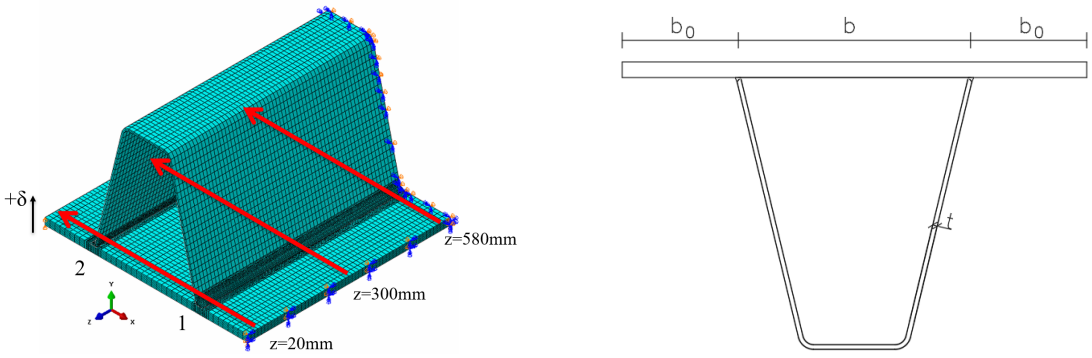

Figure 5.36: Edges along which deflection is plotted and sign convention

The deflection of the deck plate is presented in Figure 5.37. The most unfavourable vertical displacement is found at the position z=20mm, located near the free face. In this case, the deflection reaches a value of $b/500$ at the deck plate inside the trough and a value of approximately $b_0/300$ outside of it, at point x=0. The deflection shape that approaches more a realistic condition is the one found along the edge z=580mm, since the boundary conditions nearby are a good representation of actual boundaries in a large-scale deck. In this position, the deck's vertical deflection inside the trough is $b/1000$ and approximately $b_0/750$ outside. If these values are compared to the suggested value $b/200$ in EN 1993-1-5 [2], it is seen that they are quite lower than this limit. In Eurocode, the equivalent imperfection, however, is used to represent both manufacturing and fabrication imperfections. It is recommended as the geometric imperfection for a design by finite element analysis.

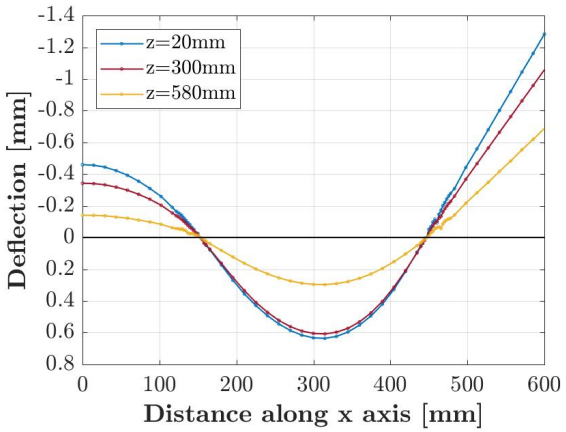

Figure 5.37: Deflection of the deck plate in case of parallel welding

5.5. Discussion

In the previous section, residual stresses have been plotted along various positions of a welded trough-to-deck plate connection. A simplified distribution of longitudinal residual stresses is presented for both models, for the position z=580mm (Figures 5.38, 5.39).

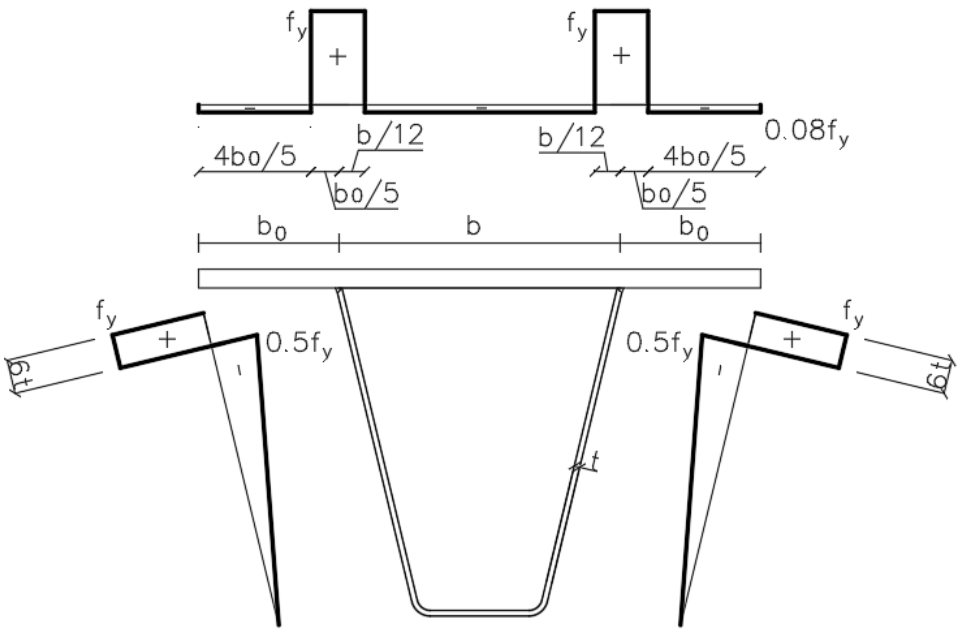

Figure 5.38: Simplification of residual stress distribution in case of manual welding

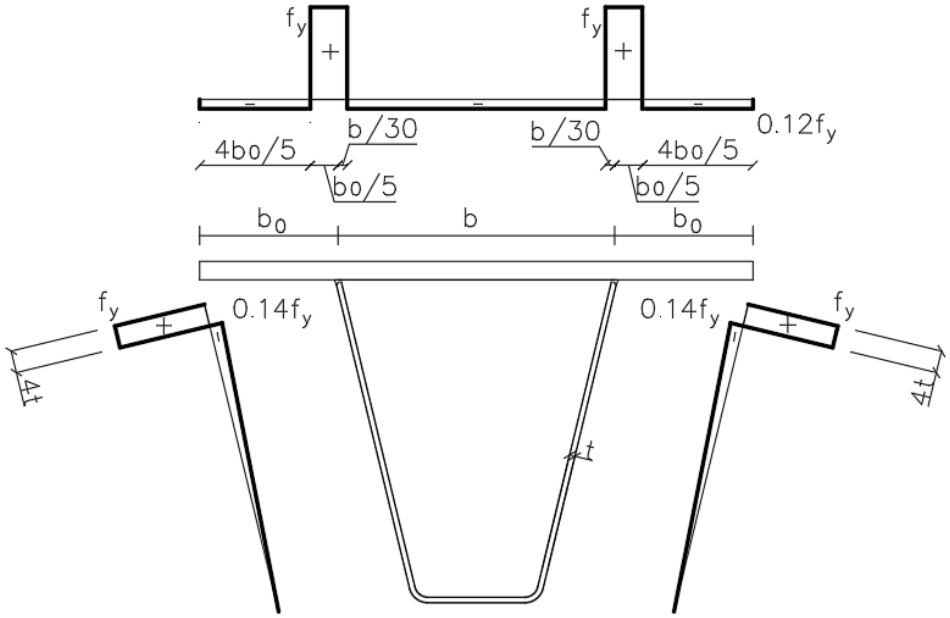

Figure 5.39: Simplification of residual stress distribution in case of automatic welding

In the first model of manual welding, tensile residual stresses with a magnitude equal to the yield stress are found around the weld, over a length of $b_0/5+b/12$ at the deck and $6t$ at the stiffeners. In the remaining parts of the deck, mostly constant compressive residual stresses appear, with an approximate magnitude of 8% of the material yield stress. In case of the stiffeners, a triangular shape of compressive stresses is observed, with a maximum value of $50\% f_y$. In the model of automatic welding, a similar stress shape is observed. Around the weld, tensile stresses at the level of the yield stress appear over a length of $b_0/5+b/30$ at the deck and $4t$ at the stiffeners. Compressive residual stresses at 12% of the material yield stress are observed at the rest of the deck. As in the previous case, compressive residual stresses with a triangular shape are found at the stiffeners, having a maximum magnitude of 14% of the yield stress. The differences in the stress magnitudes and their widths of application can be attributed to the different welding procedures.

The influence of the material model on the final results has also been examined. The adopted material model for strain hardening does not have a serious impact on the predicted stress field. As a result, the simplified stress-strain relationship suggested by [1], can be used with satisfactory accuracy.

Regarding the calculated vertical displacement of the deck plate, significantly different deflection shapes and magnitudes have been predicted for the manual and automatic welding model. The predicted distortions are considerably smaller in case of manual welding. Since the geometry, the material and the boundary conditions are the same in both cases, it is implied that the followed welding procedure can have an impact on the result.

6

Conclusions and Recommendations

This research project has been developed around two main questions:

How can the welding procedure be modelled in a finite element analysis software, so as the residual stress field can be predicted?

- In a numerical analysis, the welding procedure is described through a sequentially coupled thermomechanical analysis. Modelling of the welding heat source can be sufficiently achieved by using the double ellipsoid heat source model, whose parameters are proportional to the dimensions of the weld. Parameter α can be described by half of the weld's width, parameter b can be expressed as the weld's throat, parameter c_f can be considered equal to half the weld's width, while c_r is twice the value of parameter c_f. The validity of this conclusion has been verified through comparisons between experimental and numerical results.

- Parameters α and b of the heat source model, affect the predicted nodal temperatures. The influence depends on both the distance from the heat source and the elapsed time from welding. In the first stages of welding, their impact on the temperature is more intense for points near the weld. When the width parameter is doubled, more points on the plate surface are under the direct influence of the arc, and temperature increases locally by 75%. On the other hand, when the depth parameter is doubled, more heat is generated towards the thickness of the plate, thus surface temperature of points close to the weld drops by 10%. In the beginning of cooling, the influence of width parameter is uniform along the plate's width, since temperature increases by 20% approximately in all positions when its value is doubled. At the same stage, doubling the depth parameter results in a non-uniform temperature increase across the plate's width, ranging from 10% to zero, as the distance from the weld increases. On the other hand, the temperature distribution with time of four investigated positions has indicated that changes in the values of parameters c_f and c_r, do not affect significantly the temperature field.

- Heat losses are modelled through radiation and convection described by the radiation emissivity and heat transfer coefficient. Variations in the considered values do not affect the maximum temperatures reached in the body, but the cooling rate, after the completion of welding. Higher values of heat loss coefficients have lead to higher rates of cooling, but these still remain relatively low.

What is the distribution of residual stresses in a welded through-to-deck plate connection of an orthotropic steel deck?

- In the model of manual welding, tensile longitudinal stresses at the deck extend over a length $b_0/5 + b/12$ around the welded connection, having a magnitude equal to the yield stress. In the remaining areas, compressive stresses are present with an approximate magnitude of $0.08 f_y$. Along the stiffener's height, tensile stresses up to the yield point are found at a distance of $6t$ from the weld. The compressive stresses follow a triangular shape, ranging from $0.5 f_y$ to zero at the end.

- In the model of automatic welding, tensile stresses equal to the yield stress appear at a length $b_0/5 + b/30$, around the weld at the deck plate. Compressive stresses at 12% of the yield stress are found in

the rest of the deck. In the stiffeners, at $4t$ from the weld, tensile stresses equal to the yield stress are present. In the remaining part, compressive stresses develop from $0.14 f_y$ to zero, following a triangular shape.

- Transverse residual stresses at the deck are compressive near its surface, at the weld root and toes. In most cases, the stresses turn into tension and then compression along the thickness of the deck plate, having a maximum magnitude of 25 – 30% of the material yield strength.
- The contour plots of maximum principal stresses show that high tensile residual stresses are present around the weld, whose magnitude exceeds in certain positions the material yield stress. Considering that residual stresses are superimposed to the external ones, the effective stress under cyclic loading at these areas would be in tension, even if the applied loads cause compressive stresses. This implies that these areas are potential locations of fatigue crack initiation.

Additionally, the following conclusions can be reached:

- Longitudinal residual stresses at the deck are affected by boundary conditions. Near the unrestrained face, the maximum tensile residual stress is approximately $50\% f_y$. Compressive residual stresses reach $15 - 20\% f_y$, but appear to be zero in the middle of the deck. This fact is explained by the less restricted expansion and shrinkage of the material.
- The welding sequence does not affect significantly the predicted stresses. Between the two welding scenarios, no differences are observed in case of longitudinal stresses, both in the stiffeners and the deck plate. In case of transverse stresses at the deck, the distributions follow similar trends with respect to the stress sign and small variations have been observed in terms of the magnitude.
- The maximum vertical deflection of the deck plate was calculated as $b/3000$ and $b/500$ in case of the manual and automatic welding model, respectively. These are below the value of $b/200$, suggested by EN 1993-1-5 [2], which however includes the combined influence of manufacturing and fabrication imperfections.

Following the reached conclusions, some recommendations are made for future research:

- In this study, the research interest has focused on investigating residual stresses in a small part of an orthotropic steel deck. It is necessary to extend the analysis to a larger scale and evaluate these stress distributions in case of span lengths that are adopted in practice.
- Additional studies on the factors that affect residual stresses should be performed. Welding scenarios with various welding speeds or heat input can be implemented, so as to investigate to what extent they can modify the remaining stress field.
- Concepts of fracture mechanics can be used in order to estimate the crack propagation rate and the remaining fatigue life, under the combined action of the predicted residual stresses and local wheel load.
- For strength calculations with non-linear analyses, it is important to have information about initial imperfections. Although suggestions about their magnitude are given in EN 1993-1-5, the actual initial imperfections of a component are not known. In case of deformations induced by welding, these can be predicted through a thermo-mechanical numerical simulation. Since their value could be influenced by factors such as the deck's thickness or the welding procedure, it would be of great interest to analyse if and to what extent this effect is significant. Knowing the magnitude of initial imperfections due to welds and directly introducing them in numerical strength calculations, would make the analyses more accurate.

A

Repetition of welding experiment

During this thesis, two welding experiments have been conducted, in order to investigate the distortion of the vertical plate during welding. A suspected error in the measurements of the first experiment has lead to the repetition of the process and the evaluation of the distortion results. In this chapter, more information is given about the distortion measurements which have been taken during the welding experiments.

A.1. First welding experiment

The distortion results during the first experiment are shown in Figure A.2. According to the sign convention presented in Figure A.1, positive values of distortion are expected after the first welding pass, and negative values after the second welding pass. In this context, the negative values of distortion at positions D1 and D2 of Figure A.2a, indicate a possible measurement error. Regarding the distortions after the second weld run, as indicated in Figure A.2b, the sign of the values is negative, as expected. However, it is observed that their absolute value is significantly greater than the corresponding values of Figure A.2a. Considering that the constrainment of the vertical plate during the second pass is greater than during the first pass, due to the presence of the first weld, it seems unnatural to observe such a trend.

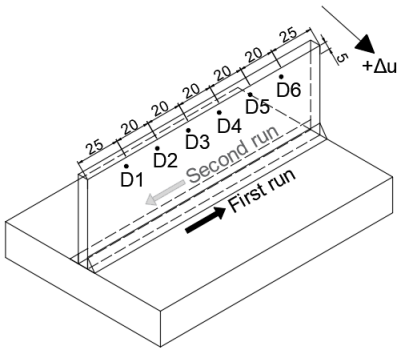

Figure A.1: Sign convention for distortions

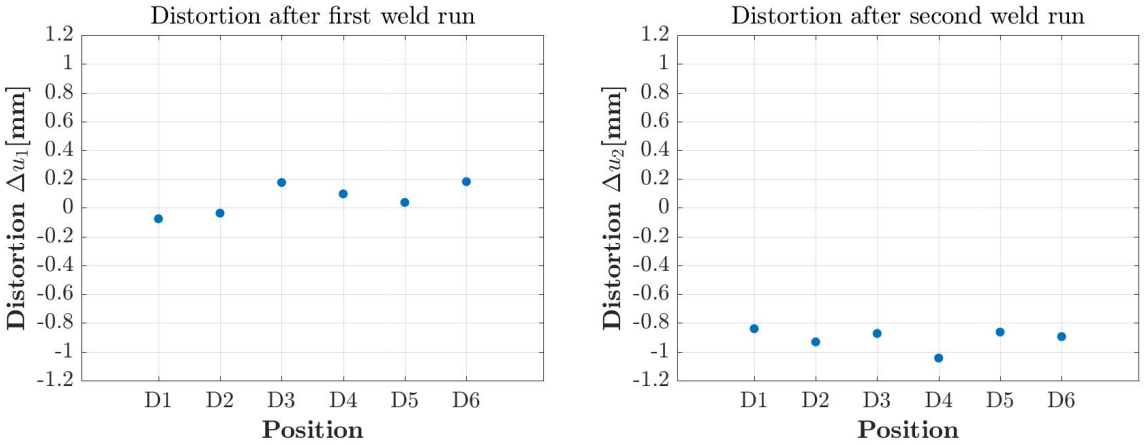

Figure A.2: Distortion measurements during first experiment

The comparison between experimental and numerical findings is shown in Figure A.3.

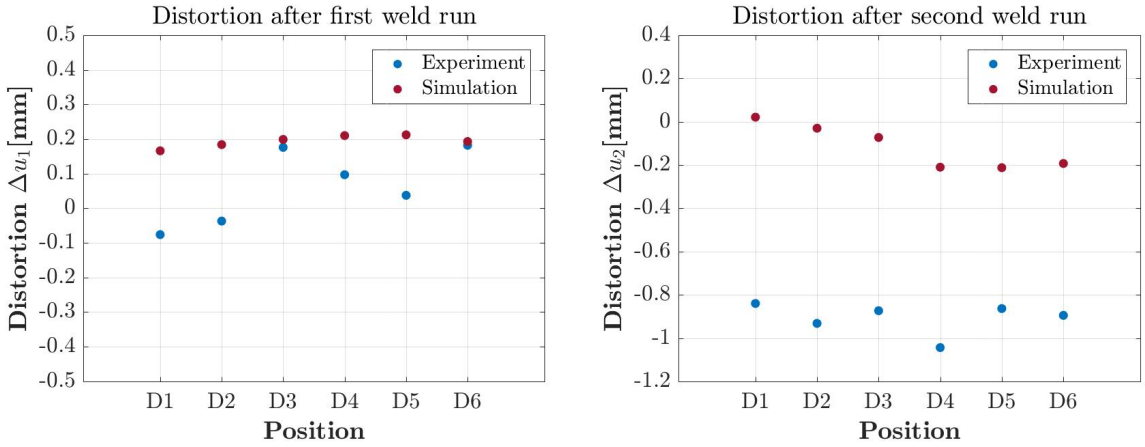

Figure A.3: Comparison of experimental and numerical distortion results during first experiment

Regarding Figure A.3a, it is observed that the numerical analysis predicts a more uniform pattern of distortions for neighbouring points, compared to experimental data. In Figure A.3b, important differences are observed. Simulation data confirm the fact that the second distortion should be less or equal than the distortion after the first pass. Following the reasoning explained before, the validity of the experimental results is further questioned after comparing them to the simulation output. By observing these differences, it is distinguished that the former ones seem displaced by an almost fixed amount from the values predicted by simulation. This could be explained by a possible systematic error included in the measurements. Even the slightest displacement of the sensor from its initial position can introduce a systematic error that is observed in every measurement.

A.2. Second welding experiment

In order to verify the validity of these doubts and limit the possibility of faulty distortion data, the welding experiment has been repeated and new distortion measurements have been derived.

During the second experiment, all parameters have been kept the same as in the initial case. Thus, two S355 plates with dimensions $100 \times 150 \times 20 mm^3$ and $55 \times 150 \times 6 mm^3$, have been welded using Gas Metal Arc Welding. The welding torch has been positioned at an angle of $90^o C$ to the direction parallel to welding and at an angle of $45^o C$, to the transverse direction. The welding speed was $7 mm/sec$.

Special attention has been given on the distortion measurement set up, so as to ensure that no errors will appear in the obtained data. As it can be seen from Figure A.4, an additional rigid constraint is used to secure the position of the clamp, on which the laser sensor is positioned.

Similarly to the procedure followed during the first experiment, the two plates were tack welded at their ends, so as to facilitate the process of welding. Welding has been executed on both sides of the vertical plate. Distortion measurements on the vertical plate have been taken at three different time moments, and six points, similarly to the procedure described in the first experiment.

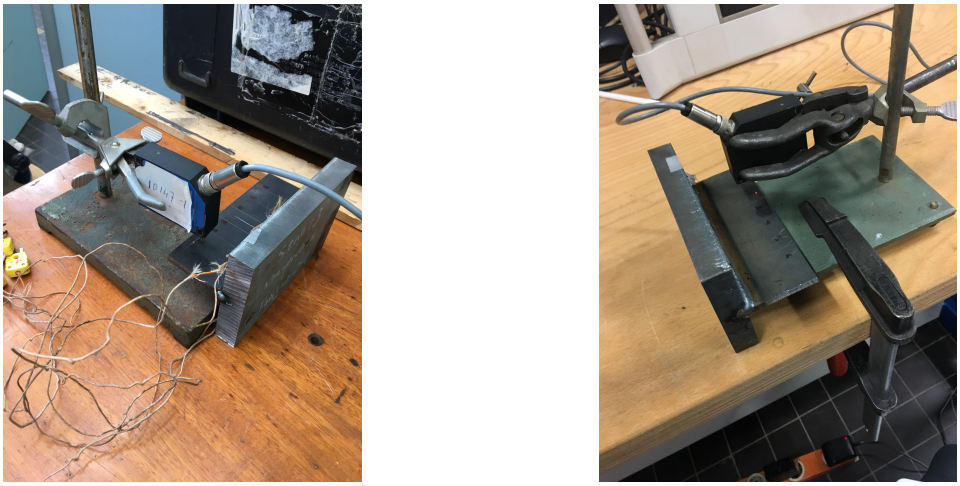

(a) First welding experiment

(b) Second welding experiment

Figure A.4: Difference in the distortion measurement set up. The clamp to which the laser sensor is attached, is held into place with a rigid constraint in (b).

Apart from distortion measurement, temperature measurements have also been obtained. This was essential, in order to ensure that temperature would variate in a similar way between the two experiments. The comparison between the temperature distributions between the first and the second experiment, is shown in Figure A.5, for positions T2, T3, during the first welding run. A good agreement is observed between the two experiments.

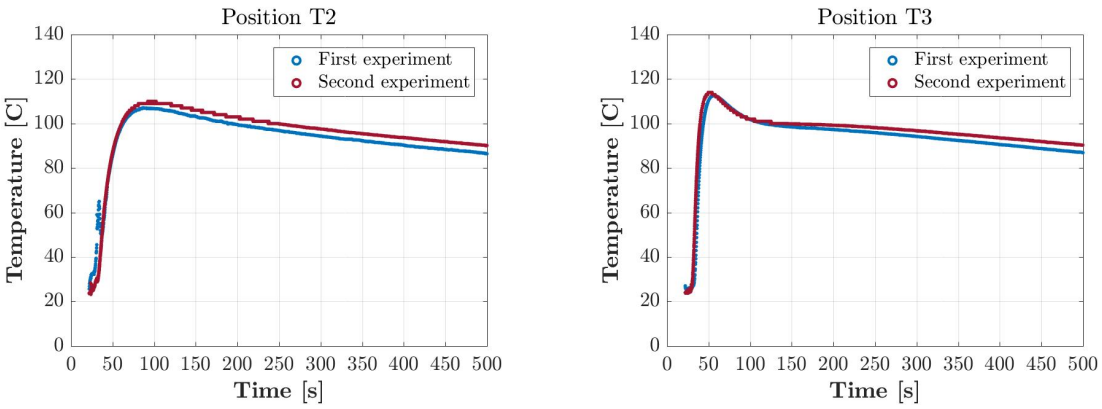

Figure A.5: Comparison of temperature distribution during first and second welding experiment in case of the first weld pass

In Figure A.6, the new measured distortion data are presented. The new experimental data confirm the fact that erroneous measurements have been taken during the first experiment. As a result, distortions derived during the second welding experiment have been used in this study for the verification of the numerical model.

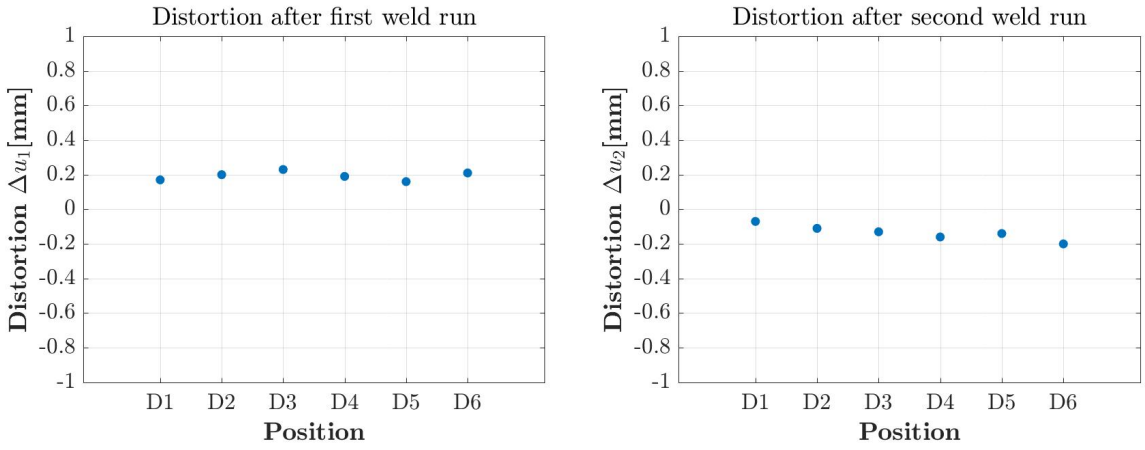

Figure A.6: Comparison of experimental and numerical distortion results, after the repetition of distortion measurements

Bibliography

[1] Eurocode 3: Design of steel structures - part 1-2: General rules - structural fire design.

[2] Eurocode 3: Design of steel structures - part 1-5: Plated structural elements.

[3] Z. Barsoum and I. Barsoum. Residual stress effects on fatigue life of welded structures using lefm. *Engineering Failure Analysis*, 2008.

[4] A. A. Bhatti, Z. Barsoum, H. Murakawa, and I. Barsoum. Influence of thermo-mechanical material properties of different steel grades on welding residual stresses and angular distortion. *Materials and Design*, 65:878–889, 2015.

[5] I. Boko, N. Toric, and B. Peros. Fire resistance analysis of steel structures. *Gradevinar*, 64(8):631–640, 2012.

[6] W. Cheng. *In-plane shrinkage strains and their effects on welding distortion in thin-wall structures*. PhD thesis, School of The Ohio State University, 2005.

[7] R. Connor, J. Fisher, W. Gatti, V. Gopalaratnam, B. Kozy, D. L. McQuaid B. Leshko, R. Medlock, D. Mertz, T. Murphy, O. Sorensen D. Paterson, and J. Yadlosky. *Manual for Design, Construction, and Maintenance of Orthotropic Steel Deck Bridges*. US DEPARTMENT OF TRANSPORTATION FEDERAL HIGHWAY ADMINISTRATION, February 2012.

[8] C. Cui, Y. Bao, and Q. Zhang. Strain energy-based fatigue life evaluation of deck-to-rib welded joints in osd considering combined effects of stochastic traffic load and residual stress. *Journal of Bridge Engineering*, 23(2), 2017.

[9] C. Cui, Q. Zhang, Y. Luo, H. Hao, and J. Li. Fatigue reliability evaluation of deck-to-rib welded joints in osd considering stochastic traffic load and welding residual stress. *International Journal of Fatigue*, 111: 151–160, 2018.

[10] F. B. P. de Jong. *Renovation techniques for fatigue cracked orthotropic steel bridge decks*. PhD thesis, Technische Universiteit Delft, 2006.

[11] TU Delft. Osd bridge specimen tested in stevin ii laboratory. URL `https://www.tudelft.nl/en/ceg/about-faculty/departments/engineering-structures/sections-labs/steel-and-composite-structures/research/phd-students/32607/weijian-wu/`. Digital image; accessed April 27, 2013.

[12] D. Deng, Y. Luo, H. Serizawa, M. Shibahara, and H. Murakawa. Numerical simulation of residual stress and deformation considering phase transformation effect. *Trans. JWRI*, 32(2):325–333, 2003.

[13] D. Deng, W. Liang, and H. Murakawa. Determination of welding deformation in fillet-welded joint by means of numerical simulation and comparison with experimental measurements. *Journal of Materials Processing Technology*, 183:219–225, 2007.

[14] J. N. DuPont and A. R. Marder. Thermal efficiency of arc welding processes. *Welding Journal*, 74:406s–416s, 1995.

[15] H. Gao. *Residual Stress Development due to High-Frequency Post Weld Impact Treatments for High-Strength Steels*. PhD thesis, Technische Universiteit Delft, 2014.

[16] J. Goldak, A. Chakravarti, and M. Bibby. A new finite element model for welding heat sources. *Metallurgical Transactions B*, 15(2):299–305, 1984. ISSN 1543-1916. doi: 10.1007/BF02667333. URL `https://doi.org/10.1007/BF02667333`.

[17] M. Hirt and J. P. Lebet. *Steel Bridges, Conceptual and Structural Design of Steel and Steel-Concrete Composite Bridges*. EPFL Press, 2013.

[18] S. Joshi, J. Hildebrand, A. S. Aloraier, and T. Rabczuk. Characterization of material properties and heat source parameters in welding simulation of two overlapping beads on a substrate plate. *Computational Materials Science*, 69:559–565, 2013. doi: https://doi.org/10.1016/j.commatsci.2012.11.029.

[19] S. Kainuma, Y.S. Jeong, M. Yang, and S. Inokuchi. Welding residual stress in roots between deck plate and u-rib in orthotropic steel decks. *Measurements*, (92):475–482, 2016. doi: http://dx.doi.org/10.1016/j.measurement.2016.06.040.

[20] A. Karlsson and C. Wesley. Fatigue analysis for orthotropic steel deck bridges. Master's thesis, Chalmers University of Technology, 2014.

[21] D. Kollar, B. Kovesdi, and J. Nezo. Numerical simulation of welding process. application in buckling analysis. *Periodica Polytechnica Civil Engineering*, 61(1):98–109, 2017. doi: 10.3311/PPci.9257.

[22] M. H. Kolstein. *Fatigue Classification of Welded Joints in Orthotropic Steel Bridge Decks*. PhD thesis, Technische Universiteit Delft, 2007.

[23] Micro-Epsilon. *Compact CMOS CCD Sensor optoNCDT 1401*. Micro-Epsilon. URL `https://tudelft.auralibrary.nl/koppelingen/documenten/feteris_opto-ncdt1401.pdf`.

[24] W. Nagy, E. Van Puymbroeck, K. Schotte, P. Van Bogaert, and H. De Backer. Measuring residual stresses in orthotropic steel decks using the incremental hole-drilling technique. *Experimental Techniques*, 41 (3):215–226, 2017. doi: 10.1007/s40799-017-0169-2.

[25] T. Nitschke-Pagel and H. Wohlfahrt. Residual stresses in welded joints - sources and consequences. *Material Science Forum*, 404-407:215–226, 2002. ISSN 1662-9752. doi: 10.4028/www.scientific.net/MSF.404-407.215.

[26] C. Ohms. *Residual Stresses in Thick Bi-metallic Fusion Welds: a Neutron Diffraction Study*. PhD thesis, Delft University of Technology, 2013.

[27] H. Pasternak, B. Launert, and T. Krausche. Welding of girders with thick plates - fabrication, measurement and simulation. *Journal of Constructional Steel Research*, 115:407–416, 2015. doi: http://dx.doi.org/10.1016/j.jcsr.2015.08.037.

[28] W. Pastorius. Laser displacement sensors - from analog to digital. Online, 2014. URL `https://lmi3d.com/company/digital-hub/blog/laser-displacement-sensors-analog-digital`.

[29] A. Pilipenko. *Computer simulation of residual stress and distortion of thick plates in multi-electrode submerged arc welding. Their mitigation techniques*. PhD thesis, Norwegian University of Science and Technology, 2001.

[30] Z.H. Qian and D. Abruzzese. Fatigue failure of welded connections at orthotropic bridges. *Frattura ed Integrita Strutturale*, 9:105–112, 2005.

[31] C. Stapelfeld, B. Launert, H. Pasternak, N. Doynov, and V. Michailov. The influence of geometrical and welding imperfections on the strength of stiffened structures. In *First Workshop Proceedings of High Performance Steel Structures Research Council (HPSSRC)*, 2018.

[32] Dassault Systemes. *Simulia Abaqus 6.13 Documentation*. URL `http://dsk.ippt.pan.pl/docs/abaqus/v6.13/index.html`.

[33] E. van der Aa. Finite element modelling of temperature profiles, distortions and residual stresses due to tig welding. Master's thesis, Delft University of Technology, 2002.

[34] G.A. Webster and A. N. Ezeilo. Residual stress distributions and their influence on fatigue lifetimes. *International Journal of Fatigue*, (23):S375–S383, 2001.

[35] P. J. Withers. Residual stress and its role in failure. *Reports on Progress in Physics*, 70:2211–2264, 2007.

[36] P. J. Withers and H. K. D. H. Bhadeshia. Residual stress - part 1 - measurement techniques. *Materials Science and Technology*, 17:355–365, 2001.

[37] W. Wu, H. Kolstein, M. Veljkovic, R. Pijpers, and J. Vorstenbosch-Krabbe. Fatigue behaviour of the closed rib to deck and crossbeam joint in a newly designed orthotropic bridge deck. In *EUROSTEEL 2017*, 2017.

[38] Z. G. Xiao, K. Yamada, J. Inoue, and K. Yamaguchi. Fatigue cracks in longitudinal ribs of steel orthotropic deck. *International Journal of Fatigue*, (28):409–416, 2005.

[39] Z. G. Xiao, K. Yamada, S. Ya, and X. L. Zhao. Stress analyses and fatigue evaluation of rib-to-deck joints in steel orthotropic decks. *International Journal of Fatigue*, 30:1387–1397, 2008.